

## Colloidal Quantum Dot Solar Cells

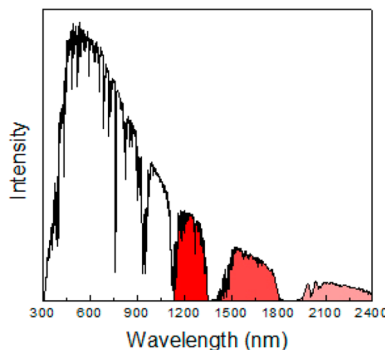
Graham H. Carey,<sup>†</sup> Ahmed L. Abdelhady,<sup>‡</sup> Zhijun Ning,<sup>§</sup> Susanna M. Thon,<sup>||</sup> Osman M. Bakr,<sup>‡</sup> and Edward H. Sargent<sup>\*†</sup>

<sup>†</sup>Department of Electrical and Computer Engineering, University of Toronto, 10 King's College Road, Toronto, Ontario M5S 3G4, Canada

<sup>‡</sup>Division of Physical Sciences and Engineering, Solar & Photovoltaics Engineering Center, King Abdullah University of Science and Technology (KAUST), Thuwal 23955-6900, Saudi Arabia

<sup>§</sup>School of Physical Science and Technology, ShanghaiTech University, 100 Haik Road, Shanghai 201210, China

<sup>||</sup>Department of Electrical and Computer Engineering, Johns Hopkins University, 3400 North Charles Street, Baltimore, Maryland 21218, United States



### CONTENTS

- 1. Introduction
- 2. Quantum Dot Synthesis
  - 2.1. Nucleation, Growth, and Stabilization
  - 2.2. Synthetic Methods
  - 2.3. Control of Quantum Dot Physical Properties
    - 2.3.1. Quantum Dot Size
    - 2.3.2. Quantum Dot Shape
  - 2.4. Control of Quantum Dot Chemical Properties
    - 2.4.1. Solution-Phase Ligand Exchange
    - 2.4.2. Alloying and Doping
    - 2.4.3. Core/Shell Quantum Dots
- 3. Materials Processing
  - 3.1. Physical Processing
  - 3.2. Chemical Processing
    - 3.2.1. Ligand Exchange
    - 3.2.2. Processing Conditions
    - 3.2.3. Impurity Management
- 4. Optoelectronic Properties of Colloidal Quantum Dots
  - 4.1. Carrier Mobility
  - 4.2. Trap Density
  - 4.3. Carrier Lifetime and Diffusion Length
  - 4.4. Doping Density
- 5. Device Physics and Performance
  - 5.1. Schottky CQD Solar Cells
  - 5.2. Heterojunction CQD Solar Cells
  - 5.3. Bulk Heterojunction CQD Solar Cells
  - 5.4. Quantum Junction and Nanoheterojunction CQD Solar Cells

5.5. Quantum Funnels	R
5.6. Graded Doping Architectures	S
5.7. Electrical Contact Development	T
5.7.1. Strategies To Improve Hole Collection	T
5.7.2. Strategies To Improve Electron Collection	T
5.8. Optical Engineering of CQD Solar Cells	U
5.8.1. Geometric and Nanophotonic Light Trapping	U
5.8.2. Plasmonic Enhancement of CQD Solar Cells	U
5.9. CQD Solar Cell Concepts beyond the Single-Junction Limit	W
5.9.1. Multiple-Junction CQD Solar Cells	W
5.9.2. Hot Carrier Effects in CQD Solar Cells	W
6. Conclusion	X
Author Information	Y
Corresponding Author	Y
Notes	Y
Biographies	Y
References	Z

D

### 1. INTRODUCTION

Colloidal quantum dots (CQDs), nanometer-scale semiconductor crystals capped with surfactant molecules and dispersed in solution, have provided a powerful platform for the development of numerous classes of solution-processed optoelectronic devices over the past decade, including photovoltaic cells, photodetectors,<sup>1–3</sup> and light-emission devices.<sup>4–6</sup> In addition to enabling solution processing, a key advantage of colloidal quantum dots is the quantum confinement effect; optical and electrical properties are readily tuned by adjusting the size and shape of the nanoparticles.<sup>7</sup> In photovoltaic devices, doped semiconductor CQD films are combined with a metal (Schottky junction cells) or with another semiconductor (CQD–CQD or CQD–titanium dioxide p–n junctions, CQD–CQD–zinc oxide p–i–n junctions), along with asymmetric electrodes, to form a complete functional device.

H

**Special Issue:** Solar Energy Conversion

P

**Received:** February 2, 2015

P

This review will focus on the application of colloidal quantum dots in photovoltaic devices. We survey the fabrication process, start to finish, addressing advances in synthesis methods, physical and chemical materials processing procedures, quantification and improvement of optoelectronic properties, and device architecture and performance. This survey addresses the key challenges facing the field: synthesizing high-quality quantum dot solutions with ideal properties (band gap, absorption, monodispersity), converting these solutions into high-quality CQD films (with ideal quantum dot packing, surface passivation, and absorptive/conductive properties), and constructing an ideal material stack around the CQD film to maximize overall device efficiency.

## 2. QUANTUM DOT SYNTHESIS

### 2.1. Nucleation, Growth, and Stabilization

For most CQD-based applications, a critical factor is the synthesis of quantum dots with a highly monodisperse, narrow size distribution. Studies of the mechanisms underlying the formation of CQDs have improved current synthetic methods and led to innovative routes for the synthesis of nanocrystals of controlled size and shape. The formation of monodisperse CQDs typically involves two steps: a rapid nucleation followed by a slow growth.<sup>8–10</sup>

Key factors controlling the rate of nanocrystal nucleation are temperature, interfacial tension, and degree of supersaturation in solution.<sup>11</sup> Nucleation can be terminated either by a reduction in concentration below a critical level or by a rapid drop in reaction temperature induced by fast injection of the precursor(s) into a hot coordinating solvent (hot-injection method).<sup>12</sup> Following nucleation, nanocrystal growth begins with molecular addition of the monomeric precursor(s) remaining in solution. Two competing effects can be observed during the growth process: focusing and defocusing. On the basis of diffusion-controlled growth, a focusing model was proposed which illustrates the growth rate and size distribution reduction.<sup>13</sup> According to the model, larger particles grow more slowly than smaller particles because the particle growth rate is inversely proportional to its radius; narrower size distributions can be obtained provided secondary nucleation is avoided and all particles are growing. By contrast, the defocusing effect is based on the solubility of the particles as a function of their size; smaller particles dissolve and larger particles continue to grow due to the higher chemical potential of the smaller particles. This phenomenon is widely known as Ostwald ripening.<sup>14</sup> It has been demonstrated that, in both diffusion-controlled and reaction-controlled growth, a critical radius for the formation of a stable particle exists, and is highly dependent on the degree of supersaturation.<sup>15</sup> In a typical synthesis, the focusing effect is observed first, with a constant number of particles and near-symmetrical size distribution. When the average particle radius exceeds the critical radius, the defocusing effect prevails; the number of particles decreases, and the result is a broader and more asymmetric size distribution.

To compensate for the high surface-to-volume ratio of CQDs, surface-passivating reagents known as surfactants or ligands are used during synthesis. The majority of established CQD synthetic routes use surfactant molecules comprised of a long hydrocarbon tail and a polar head; such surfactants include oleic acid, oleylamine, trioctylphosphine oxide, or dodecanethiol.<sup>16</sup> These surfactants can tune the reactivity of the precursors, improving control over the nucleation and growth

rates.<sup>17,18</sup> In addition, the phase,<sup>19</sup> morphology,<sup>20</sup> and optical properties<sup>21</sup> of CQDs can be tuned on the basis of the choice of surfactant.

The choice of surfactant is determined by the coordination chemistry with CQD surface atoms. On the basis of the Lewis concept of acids and bases, a hard Lewis acid will favor bonding to a hard Lewis base such as oxygen. By contrast, metal cations with a lower charge to size ratio (soft acids) prefer bonding to thiol surfactants (soft bases).<sup>7</sup> A review by Talapin et al.<sup>22</sup> summarizes the characteristics of CQDs synthesized and passivated with a wide variety of ligands.

### 2.2. Synthetic Methods

Size- and shape-controlled synthesis can be achieved using the thermal decomposition method, a low-cost, high-quality method.<sup>8,9,12,22,23</sup> The separation of nucleation and growth steps by thermal decomposition can be accomplished using either the hot-injection or the heat-up method. The hot-injection method involves the rapid injection of precursor(s) into a hot, high boiling point surfactant (Figure 1a). The injection temperature is critical, as it regulates the decomposition of the precursor(s). Upon injection, nucleation is initiated due to induced supersaturation. Injecting a room temperature solution will decrease the overall reaction temperature, terminating the nucleation stage and commencing

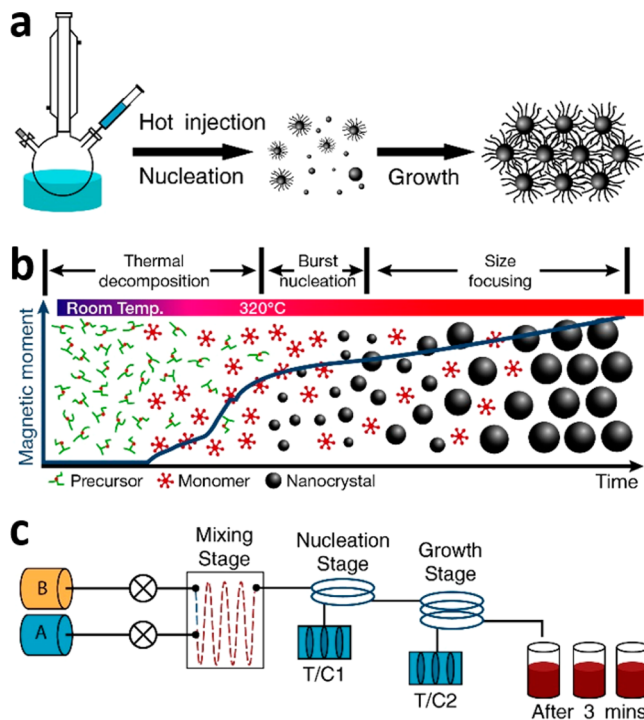


**Figure 1.** Synthetic methods. Schematic diagrams detailing a number of CQD synthesis methodologies. (a) Hot-injection synthesis, with nucleation occurring upon the injection of a room temperature precursor into a high-temperature surfactant, followed by reaction cooling leading to the growth phase. Adapted with permission from ref 9. Copyright 2007 Wiley-VCH Verlag GmbH & Co. KGaA. (b) Noninjection heat-up method. All precursors are present from the beginning of the reaction, and are steadily heated to initiate nucleation and growth stages. Adapted from ref 23. Copyright 2007 American Chemical Society. (c) Flow reactor synthesis, separating the phases of synthesis with a multistage, low-volume, continual flow synthesis reactor. Adapted from ref 24. Copyright 2013 American Chemical Society.

the growth stage. In the noninjection heat-up method (Figure 1b), the two-step mechanism is achieved through the steady heating of a mixture of precursor(s) and ligand.<sup>23</sup>

Continuous flow synthesis has numerous advantages versus batch methods, including superior control of reaction parameters, efficient reagent/solvent mixing, simplicity, scalability, and in-line analysis; additionally, this process allows for full synthetic automation. A recent study showed the impact of using a dual temperature stage flow reactor (Figure 1c).<sup>24</sup> Such a reactor allows the separation of the nucleation and growth steps, leading to improved process control and a narrower CQD size distribution.

Purification of the as-synthesized CQD is a critical step in the overall fabrication process. The presence of unreacted precursors or excess surfactants can limit charge transfer and militate against high efficiency in solar cells.<sup>25–27</sup> Typically, CQD purification takes place through sequential precipitation and dispersion in a nonsolvent and solvent, respectively. This purification technique may result in reduced CQD photoluminescence quantum yield (PLQY).<sup>28</sup> Reduction of the photoluminescence quantum yield was also observed in a recently reported purification technique: gel permeation chromatography (GPC).<sup>29,30</sup> The decrease in CQD photoluminescence quantum yield was attributed to the loss of ligands, as the quantum yield can be restored by the reintroduction of the removed ligand.

Recent reports have examined the effectiveness of in situ CQD synthesis methods such as successive ionic layer adsorption and reaction (SILAR).<sup>31–35</sup> SILAR synthesis shows good control over CQD stoichiometry and size and can improve surface ligand coverage. However, devices fabricated using SILAR-synthesized material suffer from CQD corrosion, and lead to lower efficiencies than ex situ synthesized CQD devices.<sup>36</sup>

### 2.3. Control of Quantum Dot Physical Properties

**2.3.1. Quantum Dot Size.** The band gap of CQDs can be tuned over a large spectral range by changing their size.<sup>37–39</sup> Larger band gaps are obtained by reducing the CQD size, indicated by a blue shift in optical absorption or emission spectra. In practice, the average CQD diameter is typically estimated on the basis of the observed band gap.<sup>38,40,41</sup>

Lead sulfide (PbS) CQDs are an ideal test case for examining the impact of synthesis parameters on CQD size; this material has been studied extensively due to its high air stability and ideal range of available band gaps. The hot-injection method is most widely used for PbS CQD synthesis; indeed, the current record CQD photovoltaic devices are prepared using this method.<sup>42</sup> Typically, a lead oleate precursor is formed by mixing PbO and oleic acid in octadecene, followed by the injection of bis(trimethylsilyl) sulfide (TMS) in octadecene.<sup>43</sup> This method results in PbS CQDs with diameters between 2.6 and 7.2 nm, covering a wide spectral range in absorption onset (from 825 to 1750 nm). Recently, even smaller PbS CQDs (1.5 nm) were synthesized using the same method by controlling the lead to oleic acid ratio and injection and growth temperatures.<sup>44</sup> A second synthesis variant has been established in which lead oleate and TMS are replaced with lead chloride and elemental sulfur, respectively, in oleylamine.<sup>45</sup> A narrower CQD size range is obtained via this procedure (from 4.2 to 6.4 nm), and can be extended to sizes between 3 and 10 nm by the addition of trioctylphosphine to the reaction medium (Figure 2).<sup>39</sup> Manipulating the reactivity of the precursors through the

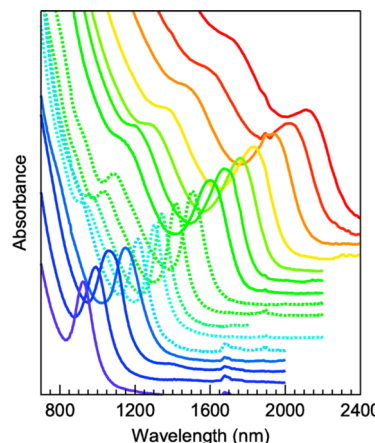


**Figure 2.** Size tunability. Absorbance spectra of PbS CQDs synthesized via hot injection of lead chloride and elemental sulfur, with additional trioctylphosphine. The CQD diameter can be tuned from 3 to 10 nm, leading to excitonic maxima ranging from 900 to 2100 nm. Reprinted from ref 39. Copyright 2011 American Chemical Society.

use of different surfactants is a well-documented method of CQD size control.<sup>46</sup> A recent study demonstrated the impact of size-selective CQD precipitation, a postsynthesis method of reducing the polydispersity of quantum dot sizes in a given population.<sup>47</sup>

Despite relatively high air stability, PbS CQDs are vulnerable to oxidation; it has been shown that oxidation states depend strongly on the quantum dot size.<sup>48</sup> Lead sulfite forms preferentially on small CQDs, while larger CQDs are prone to lead sulfate formation; the difference is due to the exposed crystal facets that depend on the quantum dot size. These oxidation products form trap states and detrimentally impact CQD film characteristics.

**2.3.2. Quantum Dot Shape.** The quantum confinement effect varies strongly depending on the material geometry; for instance, zero-dimensional CQDs show stronger quantum confinement than 1D nanowires, as one dimension of confinement has been eliminated in 1D structures.<sup>41,49</sup> Different models exist to explain the CQD shape evolution during synthesis (shown in Figure 3).<sup>12,50</sup> The classical thermodynamic model is based on minimization of the overall free energy.<sup>51</sup> In this model, particle growth is dependent on the surface energy of each crystallographic face.

The effective monomer model is a kinetics-controlled model in which the concentration, stability, and chemical potential of the precursor monomer are the governing parameters for a particular growth shape. Different quantum-confined shapes have been synthesized from a single recipe simply by varying the monomer concentration.<sup>52</sup> The selective adsorption model originates from the ability of different surfactants to bind to different facets of CQDs at different strengths.<sup>16</sup> In some cases, a mixture of surfactants is used to obtain the desired CQD shape.<sup>20</sup> The oriented attachment model evolves one shape (dots) into another (rods,<sup>53</sup> wires,<sup>54</sup> or rings<sup>54</sup>), using the fact that CQDs aggregate to eliminate high-energy surface facets and minimize the overall surface energy. Polytypism or the seeded growth model, which mainly focuses on the evolution of core/shell structures, is based on producing different shapes depending on the nucleation phase of the core CQDs.<sup>19</sup> Photovoltaic performance can be impacted by the shape of the CQDs;<sup>55</sup> large tetrapod-shaped CdTe nanoparticles showed

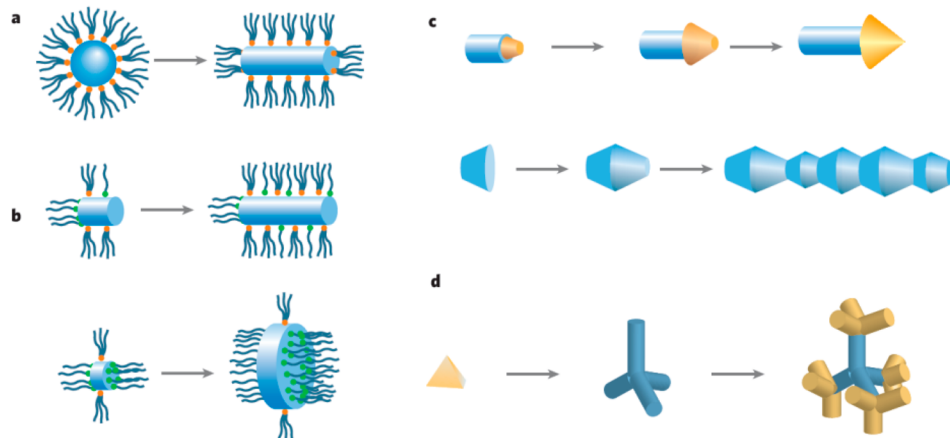


**Figure 3.** Illustration of different growth models: (a) effective monomer model, (b) selective adsorption model, (c) oriented attachment model, and (d) seeded growth model. Reprinted with permission from ref 16. Copyright 2005 Macmillan Publishers Ltd.

higher device performance than either small tetrapods or spherical CdTe CQDs.

#### 2.4. Control of Quantum Dot Chemical Properties

**2.4.1. Solution-Phase Ligand Exchange.** Long-chain surfactants enable a stable colloidal quantum dot solution; however, they act as an insulating medium around the CQDs.<sup>22,56</sup> Partially or fully exchanging the initial ligands in solution prior to device fabrication can lead to dramatic improvements in film properties and device performance. Early studies of ligand exchange reactions involved the replacement of the initial long-chain organic ligands in solution with short organic molecules such as butylamine<sup>1,57,58</sup> or pyridine.<sup>59–61</sup> Such studies revealed the difficulty in fully exchanging initial ligands in solution, and frequently required multiple solution treatments to approach full surface exchange, leading to a drop in solar cell efficiency.<sup>62</sup>

Metal chalcogenide complex (MCC) ligand exchanges have been widely studied (Figure 4A).<sup>56</sup> A wide variety of MCCs have been successfully implemented in solution-phase ligand exchanges (Figure 4B), including  $\text{In}_2\text{Se}_4^{2-}$ ,<sup>63,64  $\text{Cu}_7\text{S}_4^{-}$ ,<sup>63,65</sup>  $\text{AsS}_3^{3-}$ ,<sup>66</sup>  $\text{Sn}_2\text{S}_6^{4-}$ ,<sup>67</sup> and  $\text{Sn}_2\text{Se}_6^{4-}$ .<sup>67</sup> MCC exchanges lead to complete removal of the organic ligand, high colloidal stability, and high-conductivity CQD solids.<sup>22,56</sup> Despite the quality of</sup>

both the colloidal solution and film, high-efficiency photovoltaic devices have yet to be constructed using MCC-capped quantum dots; however, these studies provide a compelling pathway toward ligands that lead to both high conductivity and high photovoltaic efficiency.

Taken to the extreme, single atoms can be used to passivate some or all surface states.<sup>68–70</sup> Halides (chloride, bromide, or iodide) have a high affinity toward surface cations, enabling room temperature, ambient atmosphere, solution-phase ligand exchange. The PLQY of iodide-passivated PbS CQDs increased by 20% compared with that of long-organic-ligand-passivated CQDs.<sup>71</sup> Syntheses of halide-passivated PbS CQDs have been demonstrated using standard precursor injection techniques or, more recently, noninjection methodologies.<sup>72</sup> Halide-passivated PbS CQD synthesis leads to a size distribution comparable to that of the standard hot-injection method. Lead halide perovskites have recently been explored as solution-exchangeable ligands.<sup>73,74</sup> Perovskite-passivated CQDs maintain high PLQY and may present an interesting material system for photovoltaic devices.

**2.4.2. Alloying and Doping.** The band gap in cation- or anion-alloyed CQDs can be tuned by changing their constituent stoichiometries.<sup>41,75</sup> The relationship between the band gap and the mole fraction of each component is nonlinear and is governed by a bowing parameter dependent on the two binary materials.<sup>76</sup> Tuning the band gap of alloyed CQDs via stoichiometry enables absorption and emission of wavelengths that could not be achieved by the original binary materials.<sup>77</sup> The distribution of the alloy constituents determines whether the alloy is homogeneous or graded.<sup>77</sup> The exact structure of the alloy is highly dependent on the reactivity of the precursors;<sup>75,78</sup> by balancing precursor reactivities, a homogeneous alloy is produced.<sup>79</sup> The synthesis of  $\text{CdSe}_{x}\text{S}_{1-x}$  alloyed CQDs via the SILAR method was reported for photovoltaic applications.<sup>80</sup> A noninjection route has been shown effective for synthesizing  $\text{CdSe}_{0.45}\text{Te}_{0.55}$  CQDs, leading to reasonable photovoltaic performance (Figure 5).<sup>81</sup>

Doping p-type PbS CQDs with trivalent bismuth cations shifts the Fermi level, leading to n-type quantum dots; this allows the fabrication of a p–n structure with a single type of CQD.<sup>82</sup> The doping step had no effect on the shape of the CQDs, but the optical properties of the material were dramatically changed. Silver-doped PbS CQDs have led to increased solar cell device efficiency.<sup>83</sup> Silver incorporation into

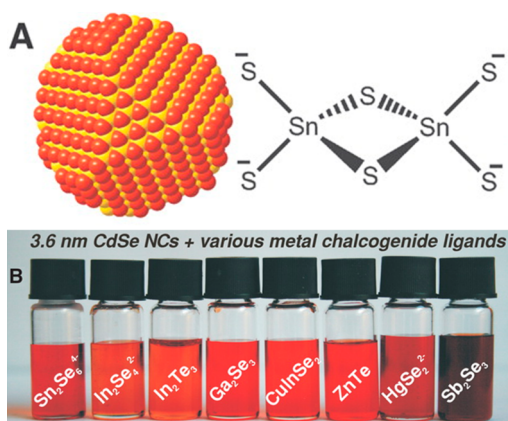


**Figure 4.** (A) CQDs capped with  $\text{Sn}_2\text{S}_6^{4-}$ . (B) CdSe CQDs capped with different MCC ligands in hydrazine. Reprinted with permission from ref 56. Copyright 2009 American Association for the Advancement of Science.

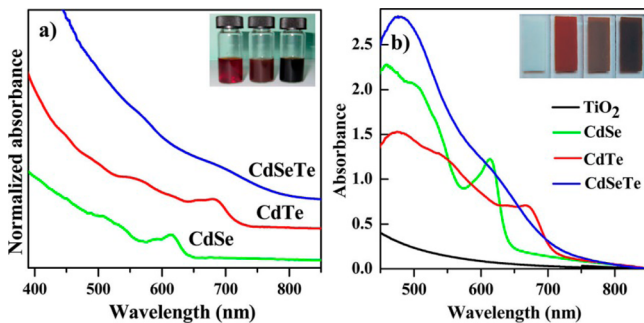


**Figure 5.** Absorbance spectra of binary CdSe and CdTe and ternary CdSeTe CQDs in both (a) solution and (b) film. Reprinted from ref 81. Copyright 2013 American Chemical Society.

the PbS lattice introduces an extra charge carrier per cation substitution. In addition to synthesis-based doping, energy landscape modifications can be made during subsequent treatment steps; this will be addressed in a later section of this review.

**2.4.3. Core/Shell Quantum Dots.** Organic surface ligands can easily desorb from the surface of the CQDs. A more efficient surface passivation can be achieved through the formation of a secondary material shell: a core/shell structure. The inorganic semiconductor shell enables complete and long-lasting isolation of the core atoms from the surrounding environment. The choice of the core and shell materials depends on two parameters: band offset alignment and the lattice mismatch between the core and shell. On the basis of the band offset alignment, core/shell structures can be divided into different types.<sup>7,84,85</sup>

Type I core/shell structures are formed through coating the core CQDs with a larger band gap material, which enables charge carrier confinement within the core. The optical properties of such a structure are core-dependent. PbS/CdS CQDs were confirmed as a type I core/shell structure on the basis of their optical properties.<sup>86</sup> The effect of size and shell thickness in solar cells sensitized with PbS/CdS CQDs revealed that small CQDs with a thin shell show high charge transfer rates.<sup>87</sup> A thin CdS shell of  $\sim 0.1$  nm has further been confirmed to provide near-complete surface passivation (Figure 6).<sup>88</sup> This core/shell structure is typically synthesized via a cation exchange procedure in which purified PbS CQDs are mixed with a cadmium precursor.<sup>89</sup>

Recently, the highest efficiency for CQD-sensitized solar cells was observed upon coating CuInS<sub>2</sub> (CIS) CQDs with a ZnS layer.<sup>90</sup> Core/shell structures can have a more profound effect on the optical properties of ternary CQDs due to the higher density of trap states in the band gap of such materials.<sup>91</sup> CdS has also been used successfully as a shell material for CIS quantum dots.<sup>4,92,93</sup> Furthermore, Mn-doped CdS shells enabled further enhancement in solar cell efficiency compared to pure CdS shells.<sup>94</sup> Mixing alloying with core/shell techniques, CISeS CQDs have been fabricated and subsequently cation-exchanged with Zn<sup>2+</sup> or Cd<sup>2+</sup>.<sup>95,96</sup> This strategy benefits from both higher infrared absorption due to alloying and reduced recombination losses due to improved surface passivation.

The band alignment in type II core/shell quantum dots (staggered alignment) is chosen so the core band gap accommodates either the valence band edge or the conduction band edge of the shell.<sup>97,98</sup> Spatial separation of the charge

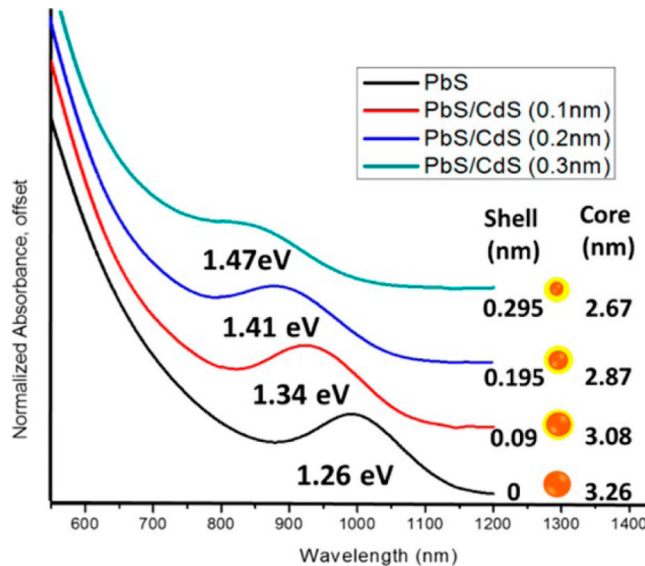


**Figure 6.** Absorbance spectra of PbS/CdS CQDs with different shell thicknesses synthesized from the same PbS batch via a cation exchange process. Reprinted from ref 88. Copyright 2014 American Chemical Society.

carriers occurs; one charge carrier is localized in the core and the other carrier in the shell, leading to reduced e–h overlap and longer exciton radiative lifetimes. With this structure, emission can be red-shifted to longer wavelengths, in particular toward the near-infrared region. Numerous type II core/shell CQDs have been explored for photovoltaic applications, including ZnSe/CdS,<sup>98,99</sup> CdS/CdSe,<sup>35,100–102</sup> CdTe/CdS,<sup>103</sup> and CdTe/CdSe.<sup>104,105</sup>

### 3. MATERIALS PROCESSING

The process of transforming synthesized colloidal quantum dots in solution into a final solid thin film for use in photovoltaic or other applications has evolved significantly over time. A broad swath of materials processing techniques have been developed to create stable, robust, high-quality colloidal quantum dot solids. These techniques can be subdivided into two broad categories: physical processing, primarily film formation, the physical means used to convert the colloid into a solid; and chemical processing, including passivation, the choice of ideal final capping ligand(s) and exchange mechanisms, densification, techniques developed to ensure minimal dot-to-dot distance to optimize optical and electrical film properties, and solvent environment and impurity removal studies.

#### 3.1. Physical Processing

While the physical process of converting a solution of quantum dots into a solid film consistently involves solution deposition and solvent evaporation, the method of deposition has significant impact on the physical morphology and macroscopic properties of the resultant film. All methods rely on depositing a small volume of solution onto a substrate and evaporating the solvent, leaving behind a collection of immobile quantum dots. Typically, a low boiling point solvent is chosen to facilitate a rapid drying step, which quickly and reproducibly produces quantum dot solids for further processing. This process varies minimally between methods; the key point of variation is the means of depositing the initial solution on a given surface.<sup>106</sup>

The majority of studies to date have focused on small-scale, batch-driven deposition methods. These methods tend to favor minimizing material use over scaling up the final film dimensions; for process development studies, batch processing is sufficient to discover and study characteristics and trends. The three batch deposition methods most commonly employed are drop-casting, spin-coating, and dip-coating. Drop-casting is the simplest of the three; a drop of solution is deposited on a substrate and simply left to dry without further physical impetus.<sup>107</sup> Drop-casting is typically employed when the quantum dots are dispersed in a high boiling point solvent such as dimethyl sulfoxide or formamide; such solvents are generally only used to disperse quantum dots capped with short, polar ligands, rather than the native long-chain organic ligands.<sup>107,108</sup> Depending on the boiling point of the chosen solvent, drop-casting can be performed on a hot plate at elevated temperature, to speed the evaporation process; however, adjusting the deposition temperature could alter the morphology and characteristics of the final film, as well as introduce chemical reactions such as oxidation into an otherwise purely physical process. The long time scales typically involved in drop-cast film formation can lead to low quantum dot packing density in the final film and negatively impact the film characteristics.<sup>109</sup>

In spin-coating, the substrate is mounted on a rotating vacuum stage, and after deposition of the initial solution, the stage is spun at typical speeds of 1000–5000 rpm, leading to spreading and shearing of the deposited solution. A constant spin-coating speed leads to reproducible, uniform thin films; to build up a film of desired thickness, the deposition and spinning process is typically repeated several times (layer-by-layer deposition).<sup>110–112</sup> This method consistently generates the highest quality film morphology, and was used in the fabrication of the latest record-performing solar cells.<sup>42</sup> Spin-coating is input-intensive, and wastes a significant fraction of the total quantum dot solution used;<sup>113</sup> additionally, the process can be highly sensitive to spin speed and ambient conditions such as temperature and humidity. Solvent choice is important; relatively low boiling point solvents such as toluene or octane must be chosen to balance colloidal stability with quick evaporation to ensure high-quality-morphology thin films. While the process is useful for small-scale device development, it is likely not conducive to scaled-up device fabrication.

Dip-coating applies a different mechanism for film deposition; rather than depositing solution on a substrate, the substrate is dipped into a stock solution of quantum dots, and withdrawn at a constant rate (typically using an automated system to ensure precision and repeatability). On the basis of the viscosity and surface tension of the solution, a thin layer is deposited on the substrate after evaporation.<sup>114</sup> This process wastes less of the initial inputs, and is slightly more scalable than spin-coating; however, it typically generates slightly less uniform films, and requires the use of lower boiling point solvents such as hexane to ensure proper deposition at the liquid/substrate interface. Dip-coating is also susceptible to changes in ambient processing conditions.

Small-scale batch processing is acceptable for initial research purposes, but as the field matures, researchers are increasingly examining the feasibility of scaled-up deposition methods. Such techniques must be able to deposit material over much larger areas, and are typically compatible with roll-to-roll processing schemes. Two such methods which have gained increasing

attention in recent years are inkjet printing<sup>115,116</sup> and spray-coating.<sup>117,118</sup> Each technique uses automated setups to reproducibly deposit very small volumes of colloidal quantum dot solution over a large area, and can be integrated into a setup with a continuous, rolling substrate for increased throughput and manufacturability. A representative spray-coating setup is shown in Figure 7.

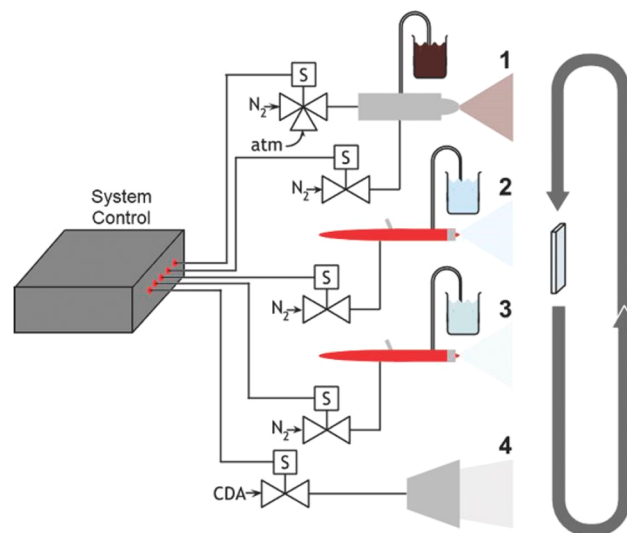


**Figure 7.** Schematic representation of the system for spray-coating colloidal quantum dot films. Reprinted with permission from ref 117. Copyright 2015 Wiley-VCH Verlag GmbH & Co. KGaA.

### 3.2. Chemical Processing

The primary goal of postsynthesis chemical processing studies is to generate a pristine final film, with quantum dots packed as tightly as possible to maximize electronic transport, while minimizing carrier trap states by passivating all available surfaces and eliminating any extraneous impurities from the film.

**3.2.1. Ligand Exchange.** As-deposited films of quantum dots are typically capped with very long, insulating ligands (oleic acid or oleylamine); these ligands are necessary to maintain colloidal stability in low boiling point organic solvents, but are detrimental to efficient electronic transport in quantum dot solids as they increase spacing between dots and lead to low film density.<sup>119</sup> The ligands can be exchanged from long ligands to short, conductive ligands in films to facilitate densification and transport between quantum dots. Numerous studies have shown the impact of varying the length of the final capping ligand on dot packing. Similar results are observed for bifunctional dithiols<sup>120,121</sup> and mercaptocarboxylic acids;<sup>122</sup> as the ligand length is reduced, the observed interparticle spacing is reduced, as shown in Figure 8a. Somewhat surprisingly, Figure 8b shows that studies of purely inorganic, atomic ligands such as halide atoms do not necessarily lead to the closest packing,<sup>123</sup> suggesting an active densifying effect during ligand exchange depending on the ligand type. Additionally, studies comparing quantum dots capped with a variety of dicarboxylic acids of similar length but variable structure show the importance of interparticle spacing and ligand structure for strong electronic coupling.<sup>124,125</sup>

Controlled full ligand removal and partial fusing between quantum dots is the next logical step in film densification.

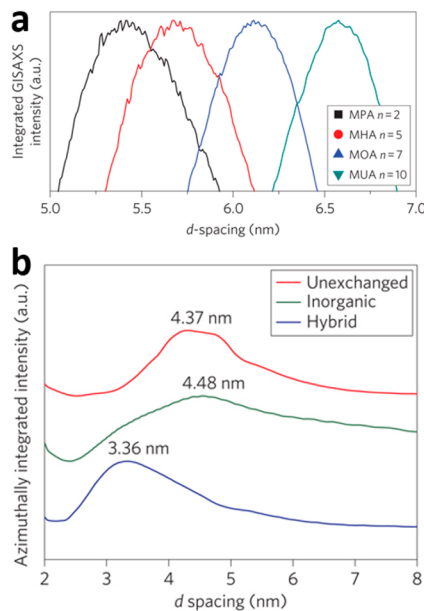


**Figure 8.** Grazing-incidence small-angle X-ray scattering data showing (a) decreases in  $d$  spacing (and increases in film density) for shorter ligands and (b) closer packing in hybrid organic–inorganic passivated films compared to inorganic-only passivated films. Panels a and b reprinted with permission from refs 122 and 123, respectively. Copyright 2012 Macmillan Publishers Ltd.

Recent studies have shown that treatment with various amines can lead to near-complete removal of all capping ligands and ordered arrays of necked quantum dots.<sup>126,127</sup> These arrays display highly efficient electronic transport, with high observed mobility and conductivity. As fabricated, such arrays failed to generate high-efficiency photovoltaic devices.

One potential reason for low photovoltaic performance in such systems may be related to the second function of capping ligands—reducing the trap state density by passivating the surface states. It is well-known that dangling bonds at surfaces in bulk semiconductors represent significant trap states; the large surface-to-volume ratios in quantum dot films magnify this effect. Various ligand strategies have been examined to minimize traps. To date, the most successful strategies include purely atomic ligands such as iodine<sup>42,71,128</sup> or bromine,<sup>68</sup> or a hybrid of atomic ligands and short organic ligands such as mercaptopropionic acid (MPA)<sup>123</sup> or ethanedithiol (EDT).<sup>129</sup> Full ligand coverage has been attempted via ligand exchange or via a mixture of passivation in solution and solid-state ligand exchange. To date, the most efficient reported CQD solar cell has employed a combination of partial fusing (through initial capping by amines) with strong passivation of the remaining surface using MPA and chloride ligands.<sup>130</sup>

A recent alternative to solid-state ligand exchange is fully solution-exchanged quantum dots. Such strategies exchange fully from long aliphatic capping ligands to the desired final short species while adjusting the stabilizing solvent from nonpolar to polar to maintain colloidal stability. Examples include the previously mentioned MCC ligands and short organic ligands similar to those used in solid-state exchanges.<sup>107,108</sup> Devices using fully solution-exchanged nanoparticles have, to date, demonstrated limited photovoltaic efficiency, due in large part to deficiencies in film formation.

Ligand exchange in metal chalcogenides (the dominant CQD materials for photovoltaic systems) has tended to focus on

passivation of exposed metal centers, with minimal research on the impact of sulfur/selenium passivation. Two binding modes have recently been proposed for thiol ligands in metal/sulfur quantum dots,<sup>131</sup> with the sulfur bound either within the nanocrystal or to a surface metal, as shown in Figure 9a. Such a

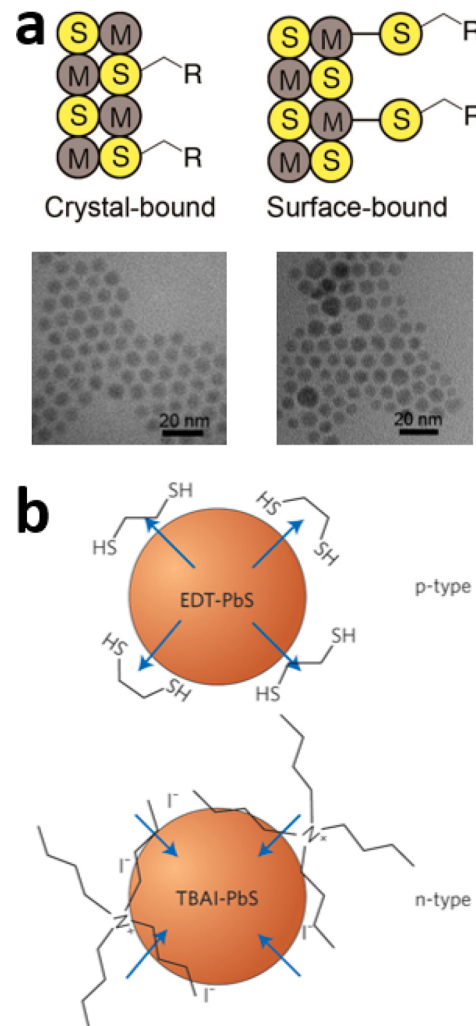


**Figure 9.** Ligand effects on quantum dots. (a) Thiol ligands shown incorporated into the crystal structure of a nanoparticle or surface-bound to metal atoms. Adapted from ref 131. Copyright 2014 American Chemical Society. (b) Variable surface dipoles on PbS quantum dots induced by different ligands, leading to p- or n-type behavior. Reprinted with permission from ref 134. Copyright 2014 Macmillan Publishers Ltd.

strategy could lead to improved overall passivation and enhanced photovoltaic performance. Additionally, a model has been proposed wherein excess metal carboxylate complexes in solution (Z-type ligands) bind reversibly to surface chalcogens, leading to dynamic surface passivation.<sup>132</sup>

Adjusting surface ligands can significantly impact the electronic properties of the film as a whole. The choice of ligand determines whether a single quantum dot species performs as an n- or p-type semiconductor.<sup>108,128,133</sup> As recently described by Milliron (Figure 9b), the choice of ligand induces surface dipoles which shift the energy levels of the quantum dot as a whole, leading to n- or p-type behavior.<sup>134</sup> Varying the surface species has a dramatic effect on the band structure of the quantum dot film.<sup>135,136</sup> The highest certified

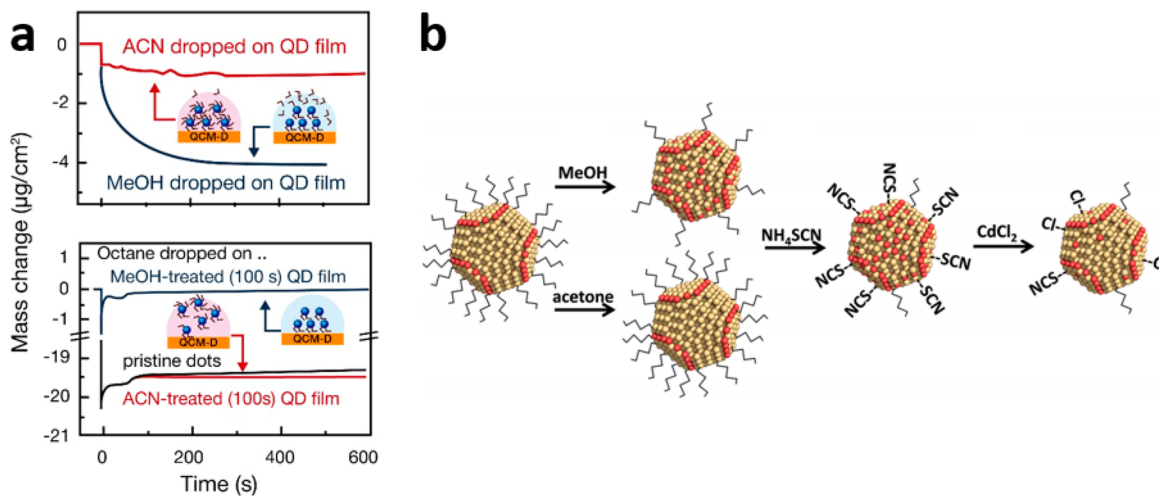


**Figure 10.** Impact of variant solvent systems, such as (a) acetonitrile or (b) acetone, on ligand exchange at nanoparticle surfaces. Panel a adapted with permission from ref 113. Copyright 2014 Wiley-VCH Verlag GmbH & Co. KGaA. Panel b reprinted from ref 140. Copyright 2014 American Chemical Society.

efficiency in a CQD solar cell to date has employed a p-i-n structure, with EDT-capped p-type PbS quantum dots, and iodine-capped intrinsic PbS quantum dots layered on an n-type zinc oxide layer.<sup>42</sup>

**3.2.2. Processing Conditions.** Relatively few studies have been performed to date on the full impact of processing conditions during postsynthesis processes on the characteristics of the final film. There is compelling evidence provided by such studies that factors such as the processing temperature, humidity, presence of oxygen, and solvent environment can impact film quality and photovoltaic performance. Some studies have examined the impact of annealing on quantum dot films, generally concluding that minimal effects are observed in the room temperature to 120 °C range, while ligand loss, domain growth, and loss of quantum confinement is observed above 120 °C.<sup>137,138</sup> Additionally, thermal annealing in air (rather than in an inert atmosphere) can lead to the formation of oxidation products.<sup>139</sup> Research has shown that an identical ligand exchange process can lead to either p- or n-type films, depending on whether the exchange is carried out under ambient conditions in air or in an oxygen/moisture-free nitrogen glovebox.<sup>128</sup>

The most efficient quantum dot solar cells are ligand-exchanged using a solution of the desired ligand mixed with methanol. Recent studies have examined the impact of methanol overexposure on film characteristics, and have explored potential alternative solvent systems (as shown in Figure 10).<sup>113,140</sup> The kinetics of ligand exchange, and the impact of the processing conditions, are beginning to receive attention; better understanding of the underlying processes could lead to more carefully designed chemical processing and higher quality films overall.<sup>141</sup>

**3.2.3. Impurity Management.** Due to the overwhelming impact of the surfaces on the overall properties of a quantum dot solid, only limited attention has been paid to the impact of chemical impurities on film characteristics, in contrast with related bulk semiconductor fields. The majority of intentional impurity (and related quantum dot stoichiometry) studies have focused on adjusting the synthesis parameters and conditions; recent evidence indicates that impurities may also be introduced in postsynthesis processes, such as the carbon-rich

stripes observed between quantum dot layers in Figure 11. Some inclusions may be inert within the film, while others

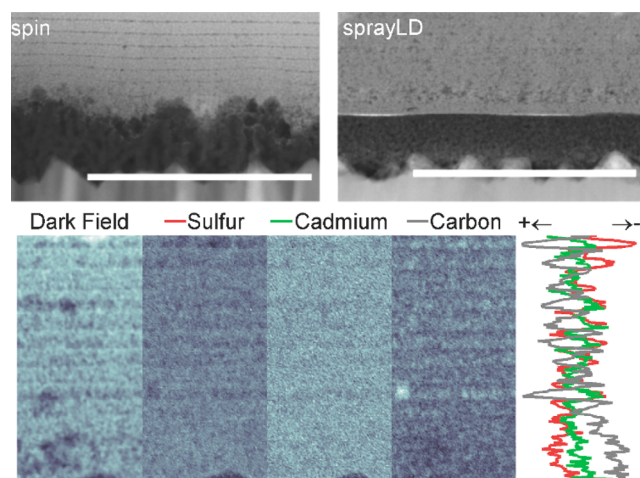


**Figure 11.** Impurities in CQD films. Cross-sectional TEM images of layer-by-layer fabricated CQD films (top) indicate the presence of impurities, which vary depending on the deposition technique. Electron energy loss spectroscopy (EELS) further elucidates that such impurities are sulfur-poor and carbon-rich (bottom). Reprinted with permission from ref 117. Copyright 2015 Wiley-VCH Verlag GmbH & Co. KGaA.

appear to be electronically active, increasing the trap state density in the film.<sup>117,142</sup> Additionally, the effect of quantum dot size polydispersity is significant; because optoelectronic properties are governed by dot size, overall film properties can be pinned by a relatively low population of differently sized quantum dots.<sup>143</sup> Novel approaches have been developed to purify films, eliminating all species other than quantum dots of a single size<sup>47</sup> and ligands directly passivating surface sites.

#### 4. OPTOELECTRONIC PROPERTIES OF COLLOIDAL QUANTUM DOTS

The critical parameters which influence CQD photovoltaic device performance are carrier mobility, doping density, trap density, and diffusion length in films (Table 1). In this section,

we will discuss recent progress in measuring and improving these parameters.

**Table 1. Common Quantum Dot Film Optoelectronic Parameters<sup>a</sup>**

property	related solar cell params	testing method
carrier mobility	$J_{sc}$ , FF	CELIV, TOF, $J_{sc}$ transient decay
trap density	$V_{oc}$ , $J_{sc}$ , FF	$V_{oc}$ transient decay
doping density	$V_{oc}$ , FF	capacitance–voltage, FET
carrier lifetime	$J_{sc}$ , FF	$V_{oc}$ transient decay
diffusion length	$J_{sc}$ , FF	photoluminescence quenching

<sup>a</sup>  $J_{sc}$  = short-circuit current,  $V_{oc}$  = open-circuit voltage, FF = fill factor, CELIV = carrier extraction by linearly increasing voltage, TOF = time of flight, and FET = field effect transistor.

#### 4.1. Carrier Mobility

Carrier mobility is one of the most important parameters for semiconductors, and plays an important role in CQD solar cells. A characterization series of the electronic properties of PbS CQD films with butylamine ligands was performed.<sup>144</sup> Carrier extraction by linearly increasing voltage (CELIV) was

used to measure the majority carrier mobility, i.e., hole mobility in a p-type film. Figure 12a shows a representative CELIV transient curve. The carrier mobility value was calculated on the basis of the time required for the current to reach a maximum value.<sup>144</sup> The calculated hole mobility was  $1.5 \times 10^{-3} \text{ cm}^2/(\text{V}\cdot\text{s})$ . The minority carrier mobility was tested by the time-of-flight (TOF) method. The transient current curve is shown in Figure 12b. To ensure accurate measurements, the film thickness is typically required to exceed 1  $\mu\text{m}$ , particularly in high-mobility films, to ensure that the measurement is not resistive-capacitive-delay-limited, and that the transit time is observable. On the basis of the transit time and bias value, the electron mobility was calculated to be  $2.1 \times 10^{-4} \text{ cm}^2/(\text{V}\cdot\text{s})$ . Considering that the minority carrier mobility was 1 order of magnitude lower than the majority carrier mobility, carrier transport was assumed to be minority-carrier-limited.

Although CELIV can be used for minority carrier mobility measurements, the method is not applicable to all device structures. Recently,  $J_{sc}$  transient decay was used for minority carrier mobility measurements.<sup>136</sup> By recording the transit time—the time for the photocurrent to decay to  $1/e$  of its maximum value—over a range of applied biases, the carrier mobility was extracted from the slope of the curve. As can be

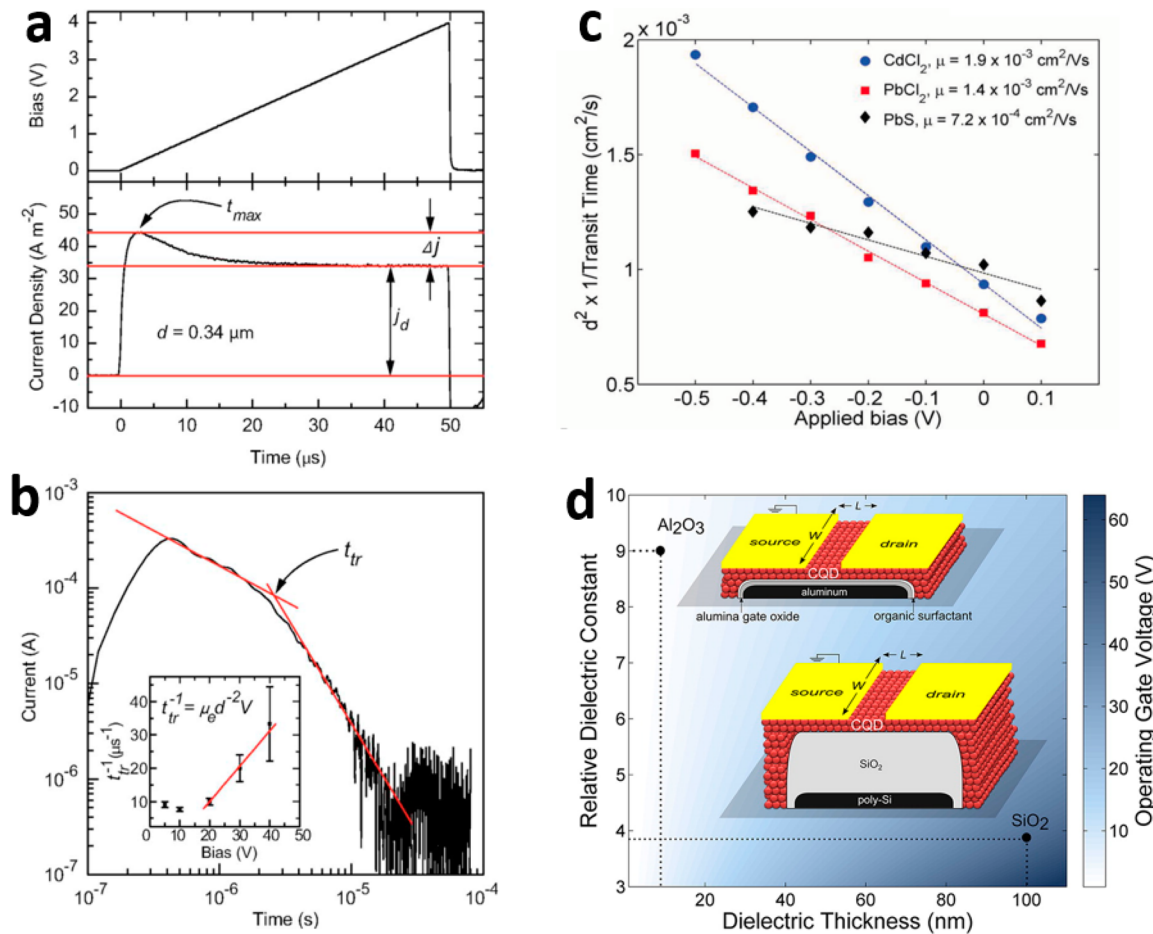


**Figure 12.** Recent development of methods for carrier mobility measurement. (a) Representative CELIV current transient curve for PbS CQDs capped with EDT. (b) Current transit curve of a TOF measurement. The inset shows the bias dependence of the transit time  $t_{tr}$ . Panels a and b reprinted with permission from ref 144. Copyright 2008 AIP Publishing. (c) Applied bias dependence of the transit time for  $J_{sc}$  transient decay measurement. The film made from CdCl<sub>2</sub>-treated PbS CQDs shows higher electron mobility than those treated by PbCl<sub>2</sub> or pure PbS CQDs. Reprinted with permission from ref 136. Copyright 2014 Wiley-VCH Verlag GmbH & Co. KGaA. (d) Schematic of an FET device structure using a Si/SiO<sub>2</sub> or Al/Al<sub>2</sub>O<sub>3</sub> gate. Reprinted from ref 145. Copyright 2013 American Chemical Society.

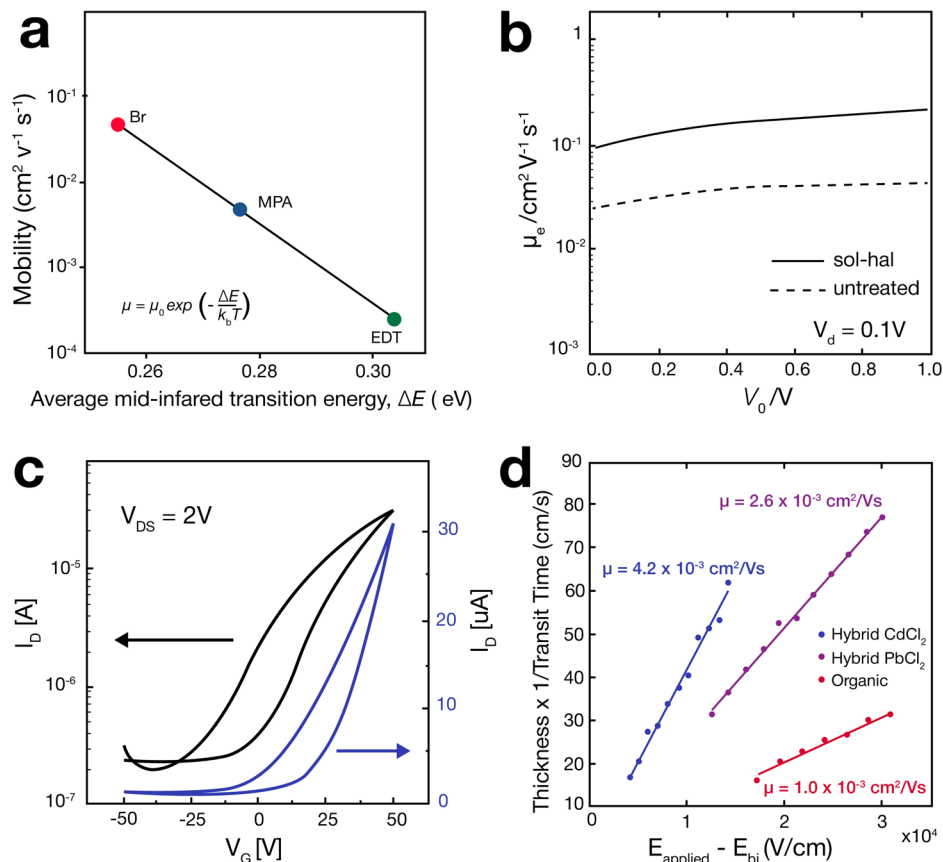


**Figure 13.** Recent developments in carrier mobility of CQD films. (a) Electron mobility comparison for PbS CQD films with bromide, mercaptopropionic acid (MPA), or ethanedithiol (EDT) ligands. Reprinted with permission from ref 68. Copyright 2011 Macmillan Publishers Ltd. (b) Electron mobility for films made from CQDs with or without solution-phase iodide treatment. Reprinted with permission from ref 71. Copyright 2012 Wiley-VCH Verlag GmbH & Co. KGaA. (c)  $I_d$  vs  $V_g$  curves for PbS CQD films treated by lead evaporation. The calculated electron mobility is  $10 \text{ cm}^2/(\text{V}\cdot\text{s})$ . Reprinted from ref 146. Copyright 2013 American Chemical Society. (d) Hole mobility for p-type CQD films with different ligands based on TOF measurements. Reprinted with permission from ref 123. Copyright 2012 Macmillan Publishers Ltd.

seen in Figure 12c, the carrier mobility was dramatically enhanced in the film made from  $\text{CdCl}_2$ -treated PbS CQDs compared to those obtained via other passivation schemes.

As previously mentioned, for majority carrier mobility measurements, TOF measurements require the use of thick films. However, the increase in film thickness can lead to poor film morphology during a layer-by-layer deposition process, which can in turn artificially limit performance. Another widely used method for majority carrier mobility measurement is the field effect transistor (FET) architecture; this method does not require the use of thick films. Silicon/silicon dioxide is generally used as the gate for FET measurements. However, defects can form in the gate dielectric during CQD film fabrication, which can cause current leakage between the source and the drain electrodes in the subthreshold region. Carrier mobility is calculated on the basis of the slope of drain–source current ( $I_d$ ) vs gate voltage ( $V_g$ ) characteristic; therefore, current leakage will significantly affect the mobility calculation. Interface defects can also cause distortions in film conductivity. Recently, Al/ $\text{Al}_2\text{O}_3$  was employed as a gate dielectric to replace the commonly used Si/SiO<sub>2</sub> (Figure 12d).<sup>145</sup> The high permittivity of  $\text{Al}_2\text{O}_3$  allows the use of a very thin gate film and much lower gate voltage, which effectively reduces the effect of charges in the gate. On the basis of the new gate substrate, much more precise measurements were realized.

Recently, the carrier mobility of CQD films was much improved by the development of novel surface ligands. The introduction of halide ligands leads to much higher carrier mobility compared with that of purely organic ligand systems (Figure 13a).<sup>68</sup> The carrier mobility of bromide ligand films approaches  $10^{-1} \text{ cm}^2/(\text{V}\cdot\text{s})$ . Changing the organic ligand can also lead to dramatic variations in the film mobility. Solution-phase halide ligand treatment was also used to improve the carrier mobility (Figure 13b). By using iodide ligand treatment both in solution and in the solid state, the film carrier mobility was increased to over  $10^{-1} \text{ cm}^2/(\text{V}\cdot\text{s})$ . Recently, on the basis of FET measurements, reported majority carrier mobilities have reached  $10 \text{ cm}^2/(\text{V}\cdot\text{s})$  (Figure 13c).<sup>146</sup> However, the efficiency of solar cells prepared by this method was limited (3.85%). The FET measurement gives an upper bound to the carrier mobility, considering that deep traps are filled during the FET scanning process. Although the efficiency of solar cells using  $\text{CdCl}_2$  treatment was 7.6%, the minority carrier, i.e., electron, mobility of the film was measurably lower than  $10 \text{ cm}^2/(\text{V}\cdot\text{s})$  (Figure 13d).<sup>123</sup> Other factors, such as trap density, may be more critical to device performance.

#### 4.2. Trap Density

Defects in the band gap can act as recombination centers to reduce photocarrier populations. Defects can also reduce the quasi-Fermi level splitting range under illumination and lead to lower open-circuit voltage. Reduction of such film defects is

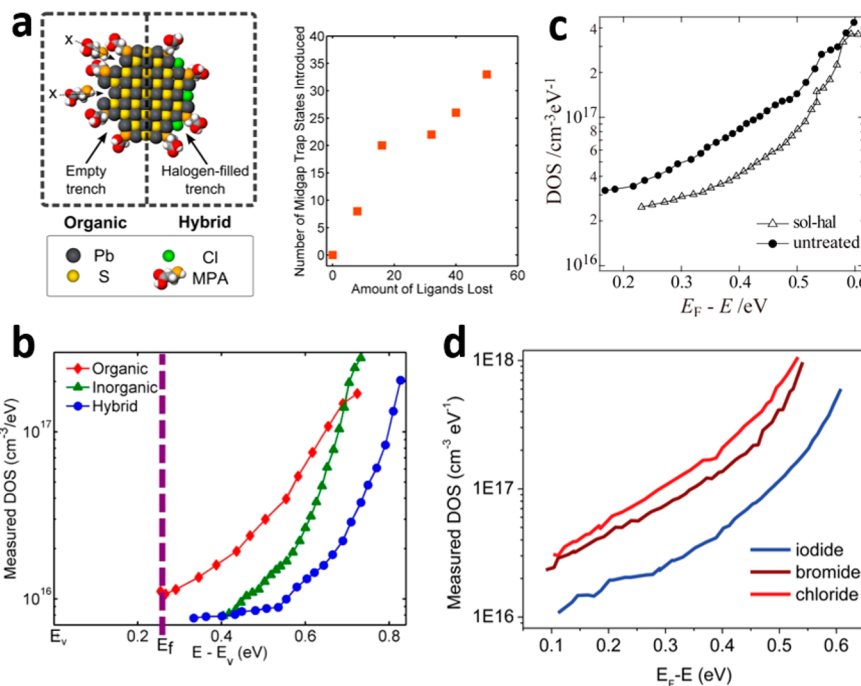


**Figure 14.** Recent developments in defect density management in PbS CQD films. (a) Schematic of CQD surface defects. The defect amount depends on the amount of ligands lost. (b) Trap density of PbS CQD films with different ligands. The hybrid passivation strategy reduces the trap density compared with both pure organic and pure inorganic ligand passivation. Panels a and b reprinted with permission from ref 123. Copyright 2012 Macmillan Publishers Ltd. (c) Trap density of PbS CQD films with or without solution-phase iodide treatment. The defect amount was reduced by using iodide solution-phase treatment. Reprinted with permission from ref 71. Copyright 2012 Wiley-VCH Verlag GmbH & Co. KGaA. (d) Trap density of films using different halide ligands. Iodide ligands lead to the lowest amount of defects. Reprinted with permission from ref 128. Copyright 2014 Macmillan Publishers Ltd.

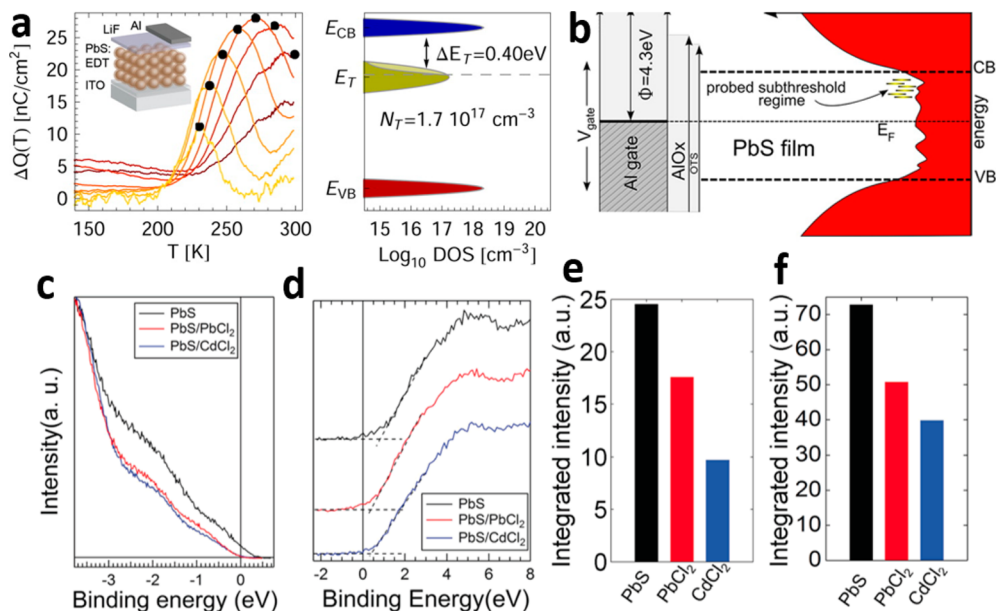


**Figure 15.** Trap density measurement methods. (a) DLTS study of charge concentration vs temperature for PbS CQD films with EDT ligands. A trap band located below the conduction band edge was observed. Reprinted from ref 147. Copyright 2013 American Chemical Society. (b) Schematic of the FET subthreshold region method used for defect measurement. Reprinted from ref 145. Copyright 2014 American Chemical Society. (c, d) PES and IPES curves for the measurement of defects in the valence band and conduction band, respectively. (e, f) Quantitative analysis of the defect concentration in both the conduction band and valence band of PbS CQD films based on PES and IPES studies. Panels c–f reprinted with permission from ref 136. Copyright 2014 Wiley-VCH Verlag GmbH & Co. KGaA.

critical to increase CQD solar cell performance. Recently, the transient photovoltage decay method was introduced to acquire the trap density in the CQD band gap.<sup>123</sup> The defect density at every applied voltage value was calculated on the basis of the

integration of the transient current and the  $\Delta V_{oc}$  value under pulsed light. Such defects are normally caused by the loss of ligands during the ligand exchange process. Figure 14b compares the band gap defect concentration for CQDs with

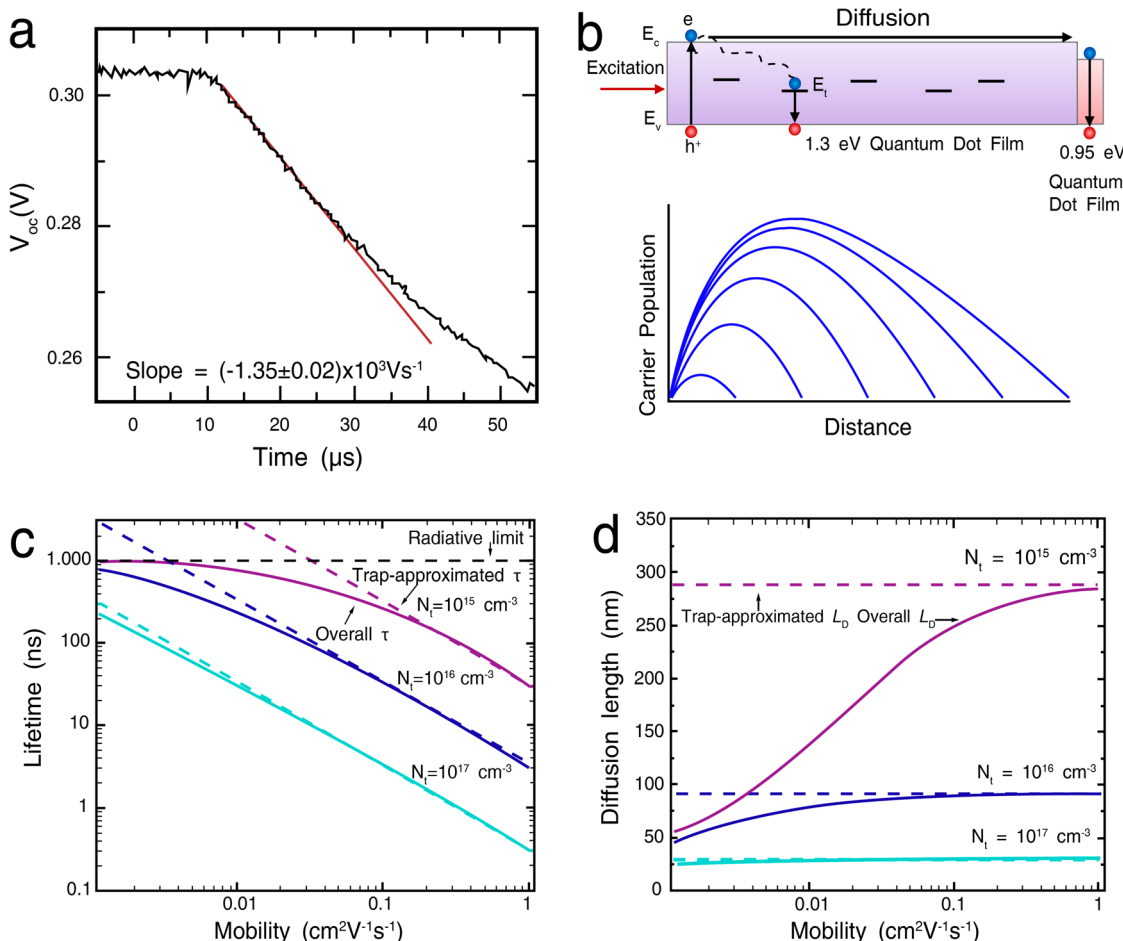


**Figure 16.** Carrier lifetime and diffusion length studies in PbS CQD films. (a) Representative  $V_{oc}$  transient decay curve for the calculation of the carrier lifetime. Reprinted with permission from ref 144. Copyright 2008 AIP Publishing. (b) Schematic of diffusion length measurement using the luminescence quenching method. The carrier diffusion length was calculated on the basis of the relationship between luminescence intensity and film thickness. Adapted from ref 152. Copyright 2013 American Chemical Society. (c) Theoretical modeling of the relationship between the trap density and carrier lifetime. (d) Theoretical modeling of the relationship between the diffusion length and carrier mobility. As the trap density is reduced, both the carrier lifetime and diffusion length are increased. Panels c and d reprinted with permission from ref 153. Copyright 2014 Macmillan Publishers Ltd.

different ligands. The use of hybrid ligands leads to reduced trap density compared with that of both pure organic and pure inorganic ligands. Iodide ligand solution-phase processing results in a lower defect concentration compared to untreated quantum dots (Figure 14c).<sup>71</sup> A strong ligand bonding strength on CQD surfaces is essential for band gap defect prevention (Figure 14d). In comparison to bromide and chloride ligands, iodide ligands give rise to much lower defect concentrations.<sup>128</sup>

Deep-level transient spectroscopy (DLTS), thermal admittance spectroscopy (TAS), and Fourier transform photocurrent spectroscopy (FTPS) have been used to measure intra-band-gap defects (Figure 15a).<sup>147,148</sup> For EDT-capped CQDs, all measurements show a defect density of about  $1.8 \times 10^{17}$  at an energy level 0.36 eV below the conduction band edge (Figure 15a). The trap density can also be extracted from FET measurements by analyzing the current in the subthreshold regime (Figure 15b). Photoelectron spectroscopy (PES) can be used to characterize the trap density near the valence band edge, while inverse photoelectron spectroscopy (IPES) can test the trap density near the conduction band edge (Figure 15c,d).<sup>136</sup> Consistent with  $V_{oc}$  transient decay measurements, the trap density of  $\text{CdCl}_2$ -treated films is much lower than that of  $\text{PbCl}_2$ -treated films or untreated CQD films (Figure 15e,f).

Strong radiative exciton decay has recently been correlated with low-defect-density materials. Photoluminescence studies are increasingly being used for optimal photovoltaic material identification and characterization.<sup>149,150</sup> The relationship between luminescence and photovoltaic power conversion efficiency has been studied in detail.<sup>151</sup> It has been shown that all types of nonradiative decay impair the open-circuit voltage and limit device performance. Hence, it has been proposed that high-efficiency solar cells should also be high-efficiency light emitters, with an ideal internal luminescence quantum efficiency of over 90%.

#### 4.3. Carrier Lifetime and Diffusion Length

The carrier diffusion length is of paramount importance to device performance considering that, in the diffusion region of actively biased solar cells, carrier transport relies solely on diffusion. Since the diffusion length is affected by the carrier lifetime and minority carrier mobility, the carrier lifetime is another crucial factor in device performance.

The CQD carrier lifetime can be tested on the basis of the slope of the  $V_{oc}$  transient decay curve (Figure 16a). In combination with the minority carrier mobility, the diffusion length of the film can be calculated.<sup>123</sup> Recently, a new method

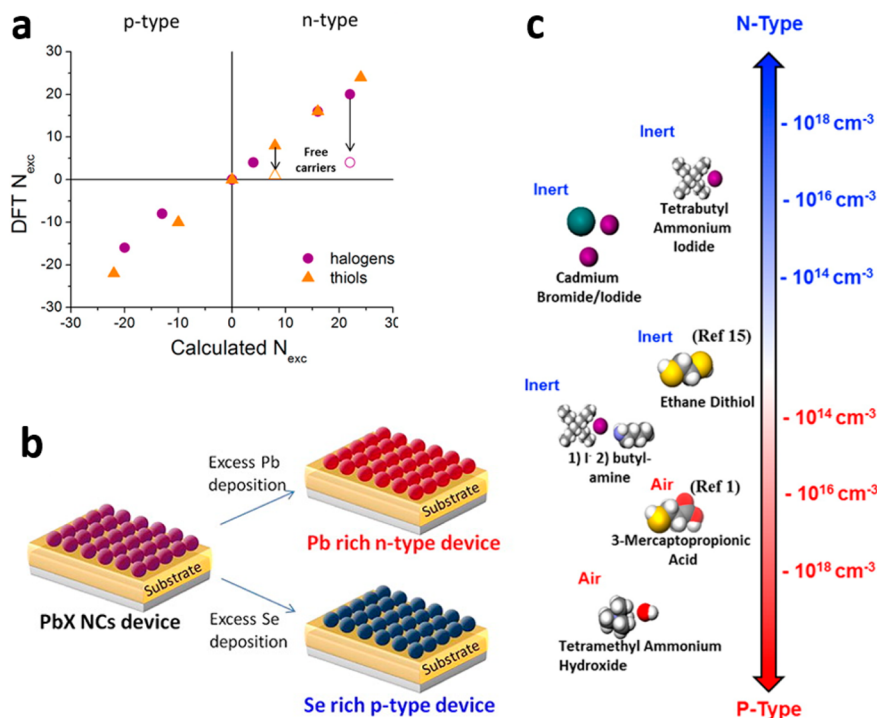


**Figure 17.** Doping mechanism in CQD films. (a) Mechanism for p-type (left) and n-type (right) doping of CQDs. When a greater positive charge exists, the film tends to be n-type, and vice versa. (b) Control of doping using different elements. When the CQD surface is lead rich, the film is n-type. When it is selenium rich, the film shows p-type behavior. (c) Variation in doping type and density as the ligand and processing environment are varied. When the film is processed in an inert environment or with halide ligands, it shows n-type character, and when treated in air or with thiol ligands, it shows p-type character. Panels a and c reprinted from ref 155. Copyright 2012 American Chemical Society. Panel b reprinted from ref 146. Copyright 2013 American Chemical Society.

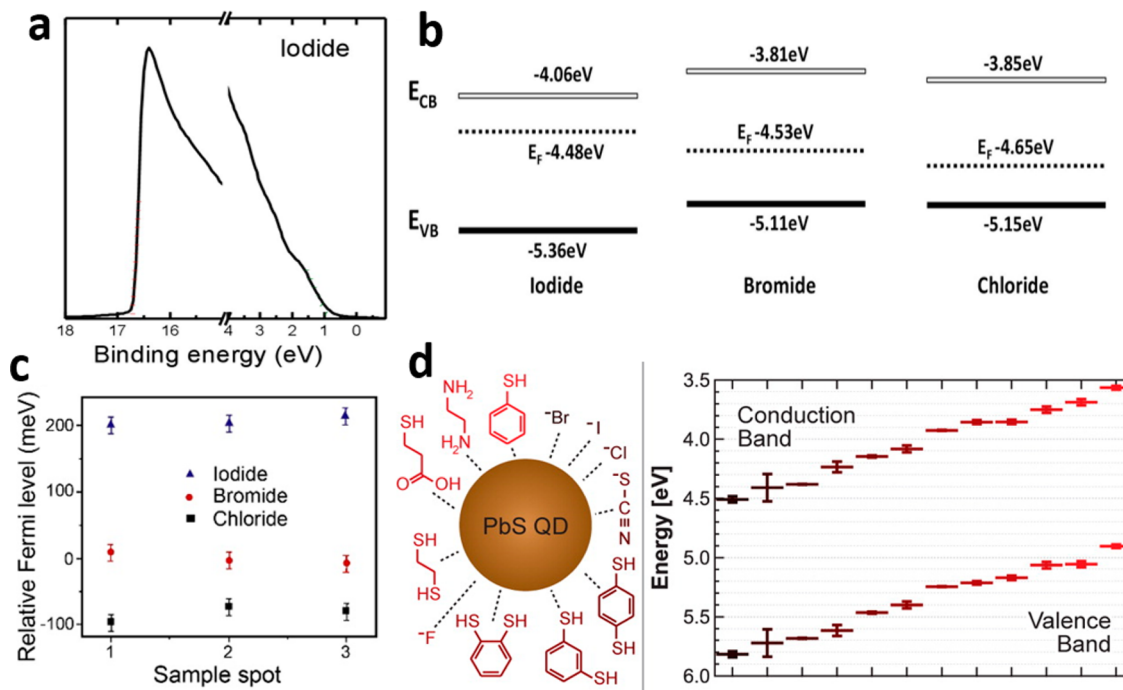


**Figure 18.** Fermi level measurements by UPS and Kelvin probe measurements. (a) UPS curve of PbS CQDs processed with iodide ligands. (b) Fermi level and band structures of PbS CQDs with different halide ligands. Iodide shows a shallower Fermi level compared to bromide and chloride. (c) Relative Fermi level positions for PbS CQDs with different halide ligands, compared to Kelvin probe measurements. Panels a–c reprinted with permission from ref 128. Copyright 2014 Macmillan Publishers Ltd. (d) UPS study of CQDs with different organic and inorganic ligands. As the electron-donating capability of the ligand increases, both the conduction band and valence band edges of the CQD film are rendered shallower relative to vacuum. Reprinted from ref 135. Copyright 2014 American Chemical Society.

**Table 2.** Optoelectronic Properties and Photovoltaic Device Efficiency Compared for a Range of CQD Treatment Types

material	$\mu_e$ [cm <sup>2</sup> /(V·s)]	$\mu_h$ [cm <sup>2</sup> /(V·s)]	trap density (cm <sup>-3</sup> eV <sup>-1</sup> )	doping density (cm <sup>-3</sup> )	diffusion length (nm)	efficiency (%)
PbS-only CQDs (no treatment) <sup>123,136</sup>	$1.0 \times 10^{-3}$	$7.2 \times 10^{-4}$	$1 \times 10^{17}$	$1 \times 10^{15}$ to $1 \times 10^{16}$	30	5.6
CdCl <sub>2</sub> -treated CQDs <sup>123</sup>	$4.2 \times 10^{-3}$	$1.9 \times 10^{-3}$	$2 \times 10^{16}$	$1 \times 10^{15}$ to $1 \times 10^{16}$	80	7.6
partially fused PbS <sup>130</sup>	$8 \times 10^{-2}$				230	9.2
bromide as ligand <sup>68</sup>	$4 \times 10^{-2}$		$5 \times 10^{16}$	$1 \times 10^{15}$ to $1 \times 10^{16}$		6
pure solid-state iodide treatment <sup>71</sup>	$2 \times 10^{-2}$		$1 \times 10^{17}$	$\sim 2 \times 10^{16}$		5.6
solution and solid-state iodide treatment <sup>71</sup>	$1 \times 10^{-1}$		$5 \times 10^{16}$	$\sim 2 \times 10^{16}$	70	6.6
EDT-treated film <sup>148</sup>	$2 \times 10^{-4}$			$1 \times 10^{17}$ to $2 \times 10^{17}$		<1.0
lead evaporation treatment <sup>146</sup>	$10 \times 10^{-1}$					3.85

was developed to test the diffusion length directly (Figure 16b).<sup>152</sup> One layer of a photoluminescence (PL) quenching material is added on top of the CQD film of interest; the carrier diffusion length can then be calculated on the basis of the CQD film thickness and corresponding PL intensity. Theoretical modeling indicates that when the trap density of the film is high, the carrier lifetime is short (Figure 16c). Similarly, when the trap density is reduced, the diffusion length of the film is increased (Figure 16d). Until recently, the highest reported diffusion length for CQD films was about 70 nm, achieved on the basis of the hybrid passivation technique. Solution-phase thiol ligand treatments were shown to slightly improve film diffusion lengths.<sup>153</sup> A recent study combined partial quantum dot fusing with strong surface passivation to generate a record diffusion length of 230 nm.<sup>130</sup>

#### 4.4. Doping Density

A major recent advance in CQD device understanding was the realization of CQD films with different doping types and densities. The first n-type CQD film was developed using halide ligands for film fabrication in an inert environment.<sup>154</sup> Stoichiometry theory was used to explain the behavior of various CQD films. With more positive charges present in the film, it tends to be n-type, and while excess negative charges lead to p-type films (Figure 17a).<sup>155</sup> An ion adsorption method was developed to build both n-type and p-type films. A film processed with lead cations tends to be n-type, while when soaked in a selenium solution, it changes into a p-type film (Figure 17b).<sup>123</sup> The same phenomenon has been observed in HgS CQDs.<sup>156</sup>

n-type films were generally thought to be unstable in air given their tendency to rapidly oxidize and return to p-type characteristics (Figure 17c). Recently, by revising the CQD solution-processing procedure to minimize the surface oxidation process in solution, air-stable n-type films were prepared.<sup>128</sup> Both ultraviolet photoelectron spectroscopy (UPS) (Figure 18a) and Kelvin probe measurements (Figure 18b) show that the work function of films using iodide ligands is shallower than that of films using bromide and chloride ligands. Air-stable n-type CQDs were observed for HgS quantum dots by using mercury cation adsorption.<sup>156</sup>

Recently, the band structures of CQD films with a series of ligands were studied (Figure 18c).<sup>135</sup> When electron-accepting ligands are used, both the conduction band and valence band are deeper, and the film tends to be n-type. In contrast, when electron-donating ligands are used, both the conduction band and valence band of the film are shallower, and the film shows p-type behavior.<sup>134</sup> Ligand selection has been shown to optimize charge generation efficiency by altering CQD frontier orbital energies.<sup>157,158</sup>

Table 2 summarizes key optoelectronic properties and photovoltaic performance for a range of CQD treatment types.

## 5. DEVICE PHYSICS AND PERFORMANCE

General advances in CQD solar cell performance have been enabled by both improved materials and developments in device architectures. The materials engineering, as overviewed in previous sections, has focused on CQD growth methods, surface management through new ligand strategies, electronic trap state removal, and deposition method development, all of which have contributed to improved solar cell performance. Architectural advances have taken inspiration from both the inorganic semiconductor and organic optoelectronic device fields, with the specific solutions tailored to CQD films and materials.

This section provides an overview of the architectural and device physics concepts that have advanced the field of CQD photovoltaics, from the first demonstrations in 2005<sup>159</sup> to certified power conversion efficiencies approaching 9% in 2014.<sup>42</sup> It finishes with a discussion of advanced concepts that seek to combine CQDs with other materials in hybrid devices and use CQD films in strategies for overcoming the single-junction efficiency limit.

### 5.1. Schottky CQD Solar Cells

The first solar cells to employ thin films of CQDs for both absorption and charge transport were developed in 2005.<sup>159</sup> These early cells took advantage of a work function difference between the transparent conductive oxide ITO (indium tin oxide) and a top metal contact (Mg) to generate a built-in field and produce a photocurrent through the CQD and polymer layers sandwiched in between. Further work replaced the polymer–CQD composite layer with a pure semiconductor nanoparticle layer,<sup>160</sup> paving the way for a device engineering approach that treated CQD films as polycrystalline semiconductor analogues rather than molecular sensitizers.

This picture, in which the CQD films could act as both absorbers and as the charge transport medium, led to the development of Schottky CQD solar cells. These cells were based on illumination through a transparent Ohmic contact to a p-type PbS or PbSe CQD film which formed a rectifying junction with a shallow work function metal. The first examples of these cells used Al as the Schottky metal,<sup>161</sup> with Ca, Mg, and Ag later demonstrated as viable alternatives<sup>162</sup> enabling improvement in open-circuit voltage. Further work improved both performance, with solar power conversion efficiencies (PCEs) reaching over 3%, and air stability by focusing on new liganding strategies,<sup>163</sup> LiF<sup>164</sup> and oxide<sup>165</sup> barrier layers, organic ETLs,<sup>166</sup> and extending the response into the infrared.<sup>167</sup>

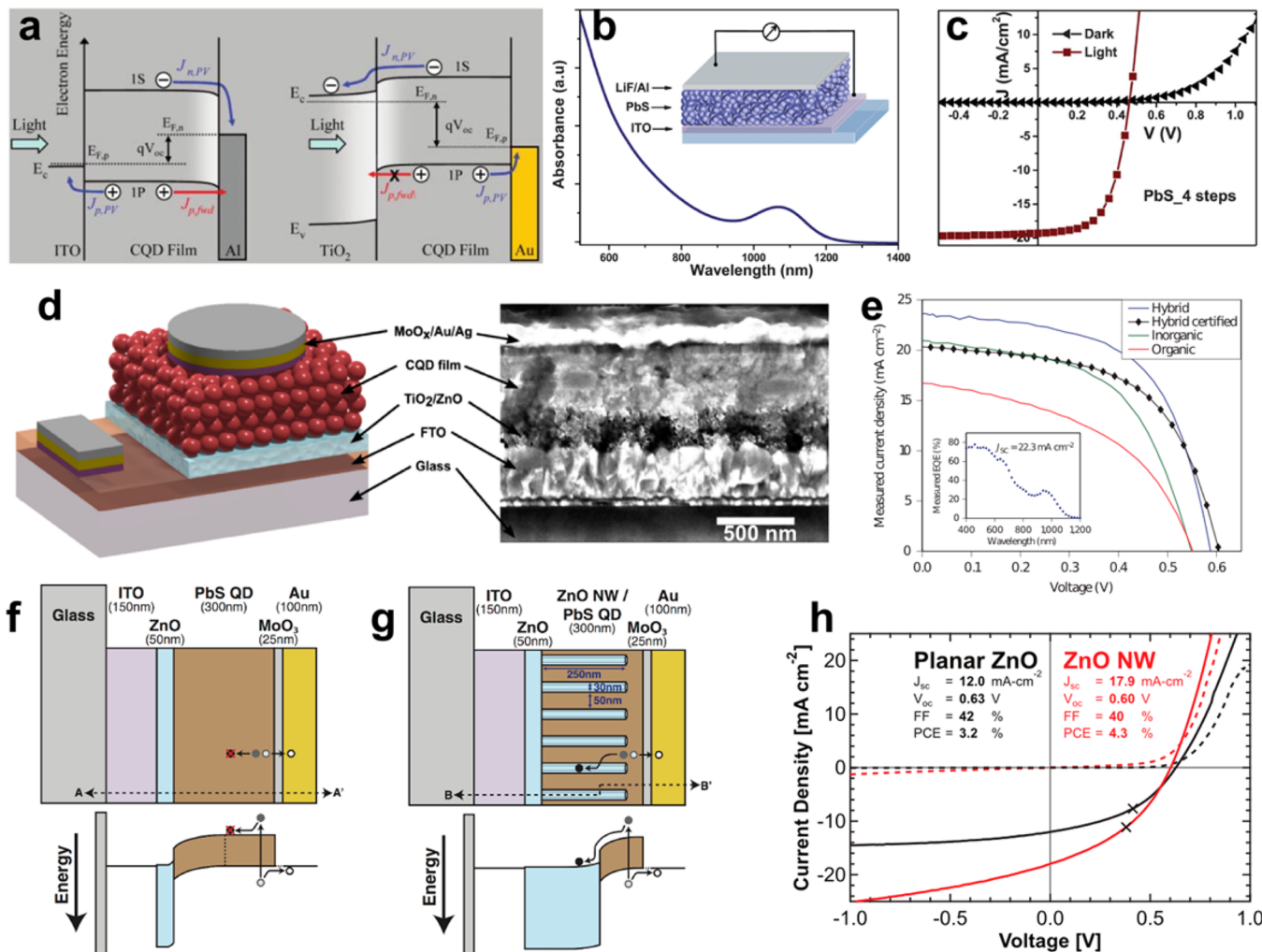


**Figure 19.** Evolution of colloidal quantum dot solar cell architectures. (a) Band diagrams of the Schottky junction (left) and the depleted heterojunction (right) CQD photovoltaic architectures under photovoltaic operation close to the maximum  $V_{oc}$ . Reprinted from ref 170. Copyright 2010 American Chemical Society. (b) Absorption spectrum and photovoltaic device structure (inset) for a high-performing PbS nanocrystal Schottky solar cell. (c) Current–voltage characteristics in the dark and under  $100 \text{ mW cm}^2$  AM 1.5 illumination of a 5.2% PCE cell with the structure shown in (b). Panels b and c reprinted with permission from ref 168. Copyright 2013 The Royal Society of Chemistry. (d) Schematic and cross-sectional SEM image of a depleted heterojunction CQD device. (e) Measured current–voltage characteristics under AM 1.5 simulated solar illumination for depleted heterojunction devices employing different CQD passivation schemes. Black tilted squares are the  $J$ – $V$  curve for a hybrid passivated device as measured by an accredited photovoltaic calibration laboratory (Newport Technology and Application Center Photovoltaic Lab). Inset: EQE curve for a hybrid passivated device with the integrated current. Panels d and e reprinted with permission from ref 123. Copyright 2012 Macmillan Publishers Ltd. (f, g). Schematic and energy band diagram at short circuit of a planar CQD heterojunction device with parallel light absorption and carrier collection pathways (f) and a bulk heterojunction device incorporating solution-processed ZnO nanowires (g). (h)  $J$ – $V$  characteristics measured in the dark (dashed lines) and under AM 1.5G illumination (solid lines) for representative planar heterojunction (black) and nanowire-based bulk heterojunction (red) CQD devices. Panels f–h adapted with permission from ref 181. Copyright 2013 Wiley-VCH Verlag GmbH & Co. KGaA.

Figure 19b shows a device schematic and absorption spectrum for the current record-performing Schottky CQD solar cell.<sup>168</sup> The current–voltage characteristics in the dark and under  $100 \text{ mW/cm}^2$  AM 1.5 illumination are shown in Figure 19c for the cell, which had a PCE of 5.2%. The Schottky architecture has several advantages, including ease of fabrication and a limited number of interfaces. It has also been used as a test bed to measure several important CQD film properties, including the size-tuned band positions of different CQD films relative to the known work functions of metals,<sup>162</sup> and elucidate the roles of drift, diffusion, and depletion in CQD-based devices.<sup>144</sup>

Despite these advantages, the Schottky architecture has been limited in absolute device performance. Fermi level pinning at

the metal–CQD interface imposes an upper bound on the open-circuit voltage that is well below the voltage predicted from consideration of the CQD band gap alone.<sup>169</sup> The introduction of buffer layers and other methods to reduce the density of electronic trap states at the interface has ameliorated this problem slightly. The Schottky architecture also requires illumination at the nonrectifying side of the junction. This is a problem in transport-limited CQD films, where it is necessary for maximum photogeneration to occur in the region of maximum internal quantum efficiency close to the junction.

## 5.2. Heterojunction CQD Solar Cells

Heterojunction CQD solar cell architectures were developed to overcome the main limitations associated with Schottky CQD

solar cells. Taking inspiration from sensitized solar cell architectures, which typically employ a monolayer of molecular absorbers on a wide-band-gap semiconductor matrix, the depleted heterojunction architecture<sup>170</sup> uses a highly doped n-type metal oxide in a p–n heterojunction with a p-type CQD film. The typical substrate consists of a glass or flexible transparent base followed by a thin transparent conductive oxide layer (usually ITO or fluorine-doped tin oxide (FTO)). TiO<sub>2</sub> and ZnO are the most commonly used wide-band-gap semiconductors that form the n-doped junction layer. The p-type absorbing CQD films, 50–400 nm in thickness, are deposited on top of the metal oxide, and the stack is finished with a back-reflective contact consisting of a deep work function metal such as gold or a highly doped oxide (MoO<sub>3</sub>) followed by silver or aluminum. A layer schematic and SEM image are shown in Figure 19d for a representative depleted heterojunction device.

The heterojunction device is illuminated through the transparent substrate and the wide-band-gap semiconductor. Photogeneration therefore occurs close to the junction region, overcoming one of the limitations of the Schottky architecture. Depletion widths in a p–n junction device depend on the relative free carrier densities in the materials on either side of the junction. The wide-band-gap semiconductor is usually highly doped so that the majority of the depletion layer falls across the CQDs. Drift currents created by the electric field are used to drive carriers in the CQD film. Some early reports observed excitonic solar cell behavior in heterojunction CQD devices;<sup>171</sup> the observation of a depletion layer in the CQDs and a transition to p–n operation was observed upon doping the ZnO side of the junction.<sup>172</sup> Band diagrams illustrating the working principles of both Schottky CQD solar cells and depleted heterojunction CQD cells are shown in Figure 19a.

A CQD solar cell with a 1 sun power conversion efficiency (2.94%) certified by an independent accredited laboratory used ZnO and PbS nanocrystals.<sup>173</sup> Performance improvement in heterojunction CQD solar cells has been rapid and relied on several materials and device engineering advances. Band alignment between the CQD film and TiO<sub>2</sub> or ZnO layers is particularly critical and must be tuned so that the electron affinity difference favors injection of electrons to the wide-band-gap semiconductor without sacrificing the open-circuit voltage. Additionally, the top Ohmic contact should be optimized to avoid the formation of a parasitic Schottky junction and avoid shunting. These issues will be discussed in depth in section 5.7.

Many of the performance advances in heterojunction architectures have been enabled by new ligand strategies which have also been developed with an eye toward improving device stability. Organic dithiol ligands<sup>174</sup> and inorganic atomic halide ligands<sup>68</sup> have been used successfully in high-performing devices. The development of a hybrid organic–inorganic ligand approach led to measurable decreases in the midgap electronic trap state density and consequent improvement in the open-circuit voltage.<sup>123</sup> Current–voltage characteristics for heterojunction solar cells employing organic, inorganic, and hybrid passivation strategies and PbS CQD films are shown in Figure 19e along with an external quantum efficiency (EQE) spectrum for a high-performing hybrid device. Cadmium and chloride passivation introduced through an *in situ* process during the CQD growth led to PbSe-based devices exhibiting record performance (6% PCE) and air fabrication.<sup>129</sup> Alternate n-type materials in place of metal oxides have also been explored, including solution-processed CdS thin films.<sup>175</sup>

Performance in heterojunction CQD solar cells based on planar films is limited by short carrier transport lengths in the CQD material. Specifically, the absorption lengths for infrared photons at the optimum single-junction band gap energies are longer than the sum of the depletion region width plus the diffusion length in the CQD materials. This trade-off is termed the absorption–extraction compromise, and it limits the thickness of the absorbing CQD material that can be effectively used in a solar cell. Strategies for overcoming the absorption–extraction compromise include the use of bulk heterojunction architectures and light-trapping schemes, both of which are discussed in subsequent sections.

### 5.3. Bulk Heterojunction CQD Solar Cells

The bulk heterojunction architecture is one method of overcoming the limitations of planar device structures. The field of organic photovoltaics developed bulk heterojunctions, in which the organic donor and acceptor phases form a three-dimensional interpenetrating network.<sup>176</sup> In excitonic materials, this ensures that no photogenerated exciton is farther than one diffusion length away from a charge-separating interface. In CQD solar cells, minority carrier transport is a particular problem, even with the benefit of a depletion region, which can be aided by the bulk heterojunction concept.

In bulk heterojunction CQD solar cells, the n-type wide-band-gap semiconductor and CQD film form an interpenetrating layer. This is usually accomplished by structuring the TiO<sub>2</sub> or ZnO and infiltrating the CQDs into the structured electrode. The structured interface allows for the extension of the depletion region and the addition of more absorbing CQD material, improving both absorption and carrier collection simultaneously.

Several methods have been used for structuring the n-type wide-band-gap semiconductor electrode. An early example used a paste of large-particle TiO<sub>2</sub> on top of a thin, compact TiO<sub>2</sub> layer and demonstrated improved absorption, EQE, and photocurrent at infrared wavelengths.<sup>177</sup> Other demonstrations of the concept have used lithographically defined TiO<sub>2</sub> nanopillar arrays,<sup>178</sup> hydrothermally grown TiO<sub>2</sub> nanowire networks,<sup>179</sup> porous templated TiO<sub>2</sub> wells,<sup>180</sup> and ZnO nanowire arrays.<sup>181</sup> The bulk heterojunction concept using ZnO nanowire arrays compared to the planar heterojunction case is illustrated with band diagrams in Figure 19f,g. Figure 19h shows current density–voltage characteristics for planar and bulk heterojunction devices based on ZnO nanowires.

The increased interfacial area inherent to the bulk heterojunction design introduces the drawback of increased bimolecular recombination. In practice, this translates to a lower device built-in voltage due to the need to manage the CQD–metal oxide conduction band offsets to prevent back-recombination. Additionally, practical measures must be taken to prevent shunting in the highly structured devices.<sup>181</sup>

### 5.4. Quantum Junction and Nanoheterojunction CQD Solar Cells

Heterojunction structures composed of metal oxides and CQD films have yielded impressive efficiencies. However, an important drawback to this device architecture is the limit on the built-in voltage that can be achieved even under degenerate doping conditions due to band offsets. The additional requirements of engineering the non-CQD side of the junction for band alignment with different CQD films and remediation of interface trap states further limit the utility of this architecture for application in multijunction solar cells.

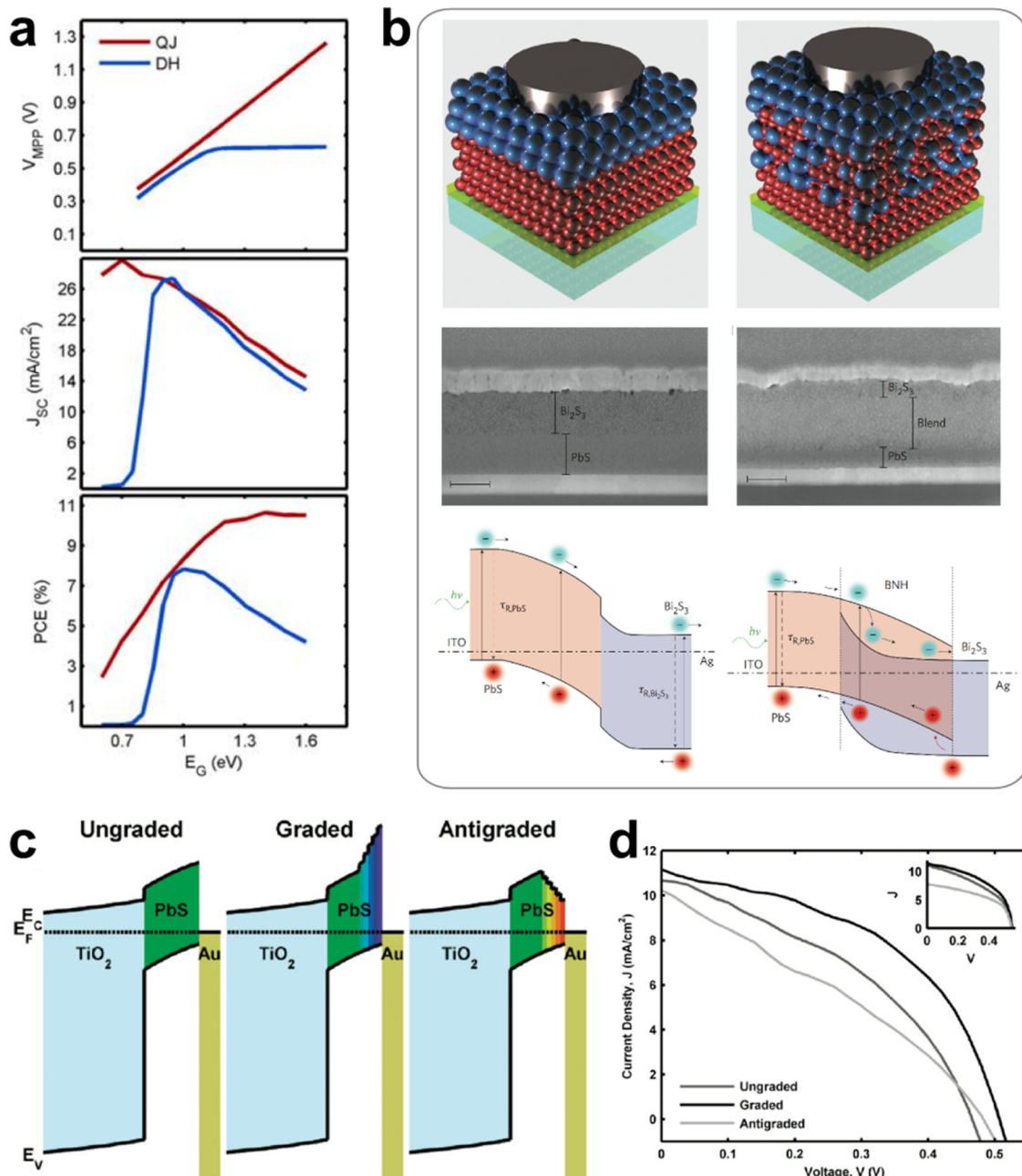


**Figure 20.** Homojunction and quantum funnel architectures. (a) Simulated solar cell performance, showing the predicted operating voltage at the maximum power point ( $V_{MPP}$ ), the short-circuit current ( $J_{sc}$ ), and the solar power conversion efficiency (PCE), for depleted heterojunction (DH; blue) and quantum junction (QJ; red) devices as a function of the quantum dot band gap. Reprinted from ref 154. Copyright 2012 American Chemical Society. (b) (Top) Schematics of a bilayer homojunction device structure (left) and a bulk nanoheterojunction structure (right) consisting of ITO–PbS quantum dot (red spheres)–Bi<sub>2</sub>S<sub>3</sub> nanocrystal (blue spheres)–Ag layers. (Middle) Cross-sectional SEM images (scale bars 200 nm). (Bottom) Band diagrams of the two structures. Reprinted with permission from ref 182. Copyright 2012 Macmillan Publishers Ltd. (c) Spatial band diagrams of ungraded, graded (quantum funnel), and antigraded CQD solar cells. Color coding corresponds to larger band gaps (more blue/violet) and smaller band gaps (more yellow/red). (d)  $J$ – $V$  performance under AM 1.5 conditions of the ungraded, graded (quantum funnel), and antigraded devices indicating the increase in fill factor as the dominant mechanism for improvement in PCE. The inset shows modeled  $J$ – $V$  curves for optimal 120 nm device thickness. Panels c and d reprinted from ref 185. Copyright 2011 American Chemical Society.

The drawbacks associated with heterojunctions can, in principle, be overcome by using a homojunction-like architecture where both the p- and n-materials of the junction are composed of CQDs. Figure 20a compares the simulated open-circuit voltage, short-circuit current, and power conversion efficiency values as a function of the quantum dot band gap for depleted heterojunction and all-CQD junction (quantum junction) devices.<sup>154</sup>

The main roadblock to realizing this type of architecture was the difficulty in developing stable n-type CQD films due to the action of oxygen as a p-type dopant.<sup>155</sup> This barrier was overcome through the development of new ligand strategies, as described in section 3.2.1. These strategies for PbS CQDs included inert processing,<sup>154</sup> in situ atomic halide passivation,<sup>108</sup> and cation substitutional doping with Bi.<sup>82</sup> Quantum junction solar cells were demonstrated using widely tuned

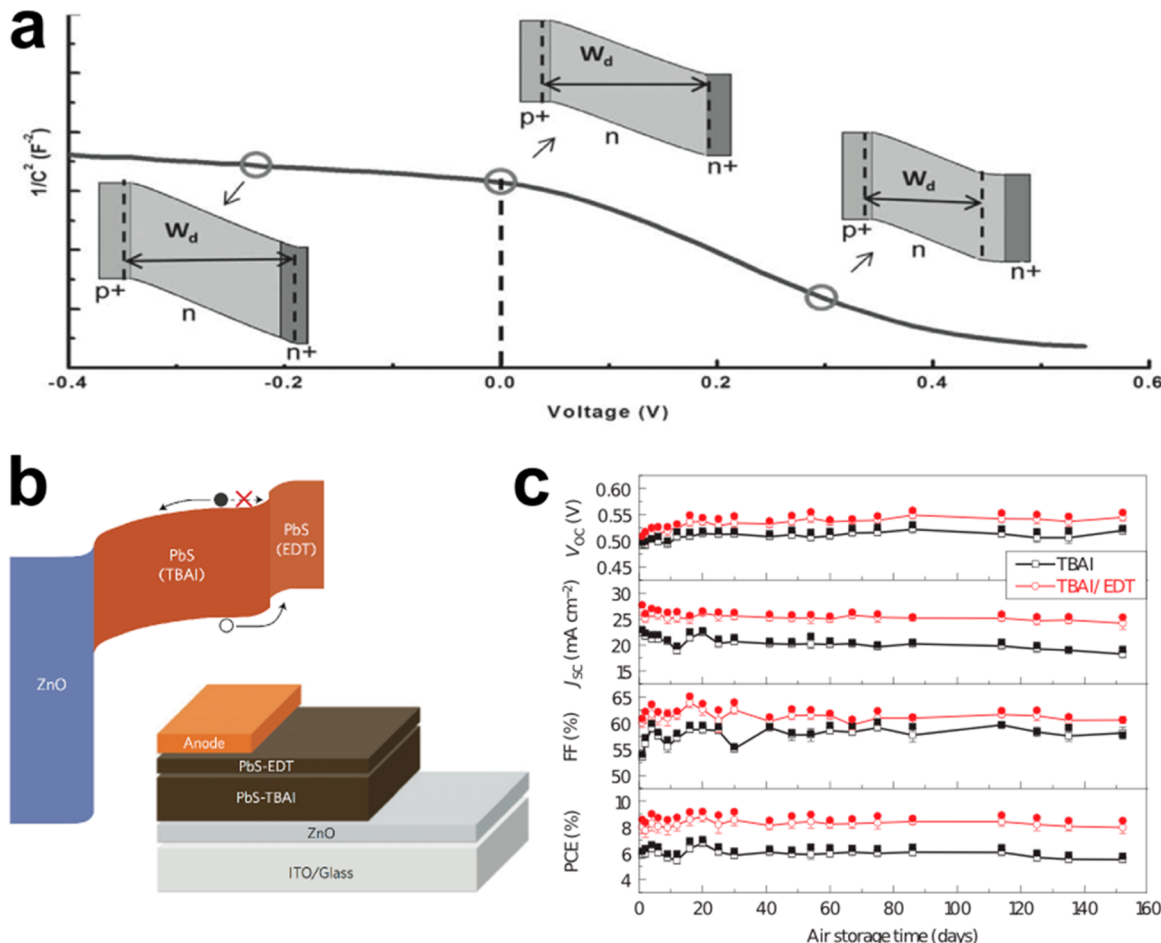


**Figure 21.** Graded doping and band alignment engineering. (a) Regimes of depletion in a graded device. Devices with doping gradients exhibit two distinct slopes in Mott–Schottky analysis consistent with two differently doped CQD layers. Reprinted with permission from ref 187. Copyright 2013 Wiley-VCH Verlag GmbH & Co. KGaA. (b) Schematic illustration of the proposed band bending at short-circuit conditions (left) in the ZnO/PbS-TBAI/PbS-EDT (TBAI = tetrabutylammonium iodide) device structure (right). (c) Time evolution of photovoltaic parameters of PbS-TBAI (black) and PbS-TBAI/PbS-EDT (red) devices, illustrating excellent long-term stability. Open symbols represent the average values, and solid symbols represent the values for the best-performing device. Panels b and c reprinted with permission from ref 42. Copyright 2014 Macmillan Publishers Ltd.

CQD band gaps of 0.6–1.6 eV.<sup>154</sup> Further optimization of the device structure<sup>83</sup> and ligand strategies<sup>108</sup> produced power conversion efficiencies of over 6%.

A related architecture that relied on the development of n-type nanocrystals is the bulk nanoheterojunction solar cell. One study<sup>182</sup> used colloidal  $\text{Bi}_2\text{S}_3$  nanocrystals as the n-type material and PbS CQDs as the p-type material in a bulk heterojunction architecture. The two types of nanoparticles were partially intermixed, as shown in Figure 20b, and both contributed to photocharge generation. The bulk structure allowed charges generated in both materials to be close to a charge-separating interface, resulting in a 3-fold performance improvement over a bilayer structure. Further work introduced a remote trap passivation scheme in which ZnO nanocrystals were intermixed with PbS CQDs in a bulk nanoheterojunction device.<sup>183</sup> The highly doped ZnO nanocrystals transferred charges to deep electron acceptor sites in the CQDs, resulting in an improved open-circuit voltage.

### 5.5. Quantum Funnels

Exciton funneling through the use of graded band gap materials is another strategy that has been used to aid carrier transport and collection in CQD solar cells. In a heterogeneous ensemble

of CQDs, such as those found in most practical films, photoexcited carriers will generally end up in the CQDs with the smallest band gaps.<sup>184</sup> This concept can be used to effectively funnel carriers to the charge-collecting junction when the cell is operating under noncomplete depletion at its maximum power point by employing an intentionally graded band gap architecture. CQDs are uniquely suited to implement such an architecture, due to their facile band gap tuning through the quantum size effect and their layer-by-layer deposition methods.

The quantum funnel concept was implemented in a truncated heterojunction architecture using five quantum dot layers with band gap energies ranging from 1.06 to 1.35 eV in both graded and antigraded configurations, as illustrated in Figure 20c.<sup>185</sup> In this demonstration, the primary factor driving enhanced performance over ungraded and antigraded controls was an improved fill factor due to the graded device ensuring that minority carriers were driven to the electron-accepting electrode, even when reverse bias was reduced under operating conditions away from short circuit (Figure 20d).

Further work has used the quantum funnel concept to engineer the electric field profile in a quantum junction CQD solar cell.<sup>186</sup> Both the open-circuit voltage and short-circuit

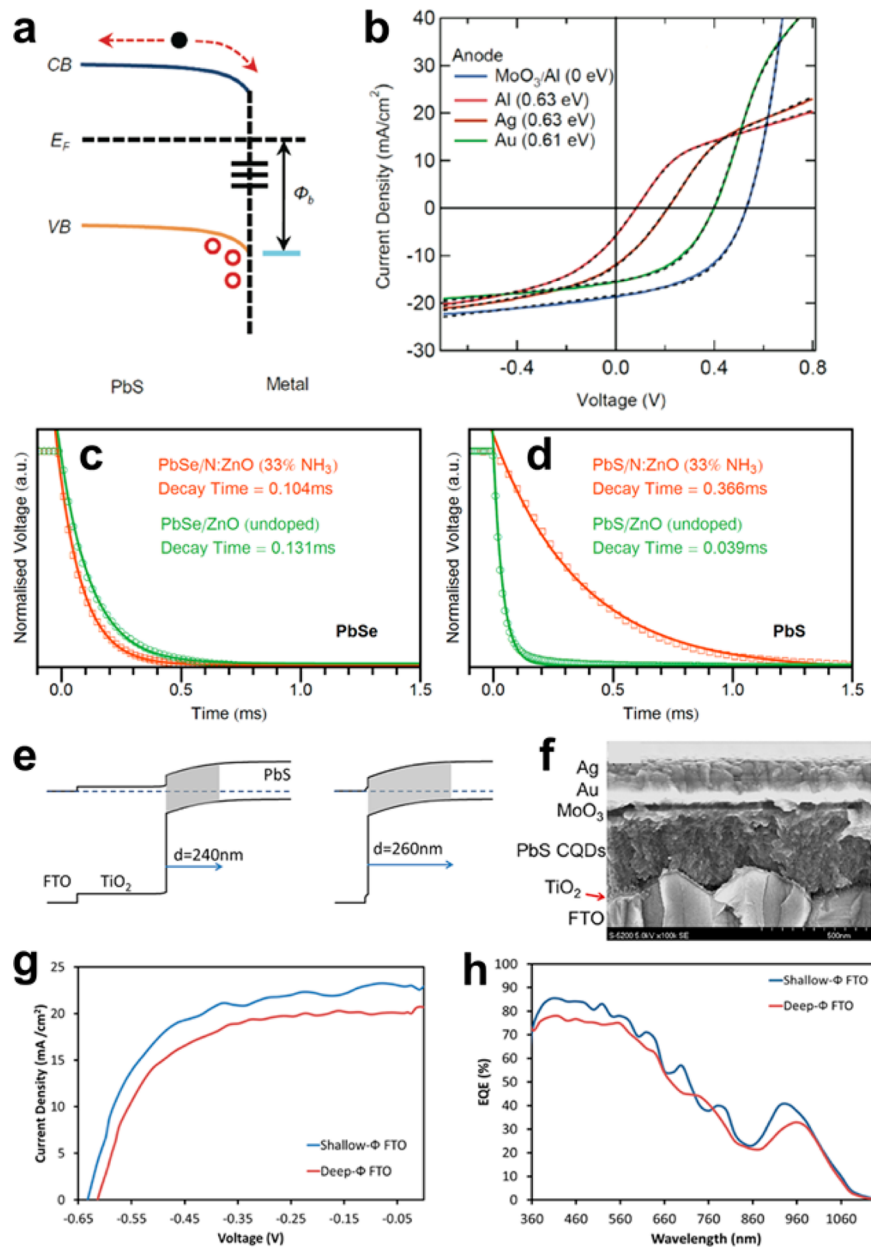


**Figure 22.** Advances in electrode engineering. (a) Ohmic contact engineering: schematic energy diagram of the unintentional Schottky diode that can occur at the PbS–metal interface. (b)  $J$ – $V$  characteristics under  $100\text{ mW}/\text{cm}^2$  white light illumination for devices with different Ohmic contacts. The dotted lines are fitting curves based on a two-diode model. The values in parentheses are the fitting results of the Schottky junction hole injection barrier height. Panels a and b reprinted from ref 191. Copyright 2011 American Chemical Society. (c, d) Electron-collector engineering: photovoltage decay measurements on (c) PbSe and (d) PbS solar cells using undoped and nitrogen-doped ZnO electrodes. The solid lines show monoexponential fits to the data with the time constant displayed in the inset. Panels c and d reprinted from ref 198. Copyright 2013 American Chemical Society. (e) Band diagram for a typical PbS CQD photovoltaic (PV) device with a deep work function FTO layer and a TiO<sub>2</sub> thickness of 300 nm (left) and a shallow work function FTO layer and a thin 10 nm TiO<sub>2</sub> layer (right). The width of the depletion region (gray color) inside the PbS film,  $d$ , is larger in the right diagram, illustrating the donor-supply electrode concept. (f) Cross-sectional SEM image of a CQD device on a donor-supply electrode (shallow work function FTO with a 10 nm atomic-layer-deposited TiO<sub>2</sub> film). (g) Light  $J$ – $V$  curve and (h) EQE spectra for a CQD PV device fabricated on shallow (donor-supply electrode) and deep work function ( $\Phi$ ) FTO with 10 nm thick TiO<sub>2</sub> layers. Panels e–h adapted from ref 200. Copyright 2013 American Chemical Society.

current were increased by adding a top CQD layer with a larger band gap to an optimized quantum junction device.

### 5.6. Graded Doping Architectures

The highest power conversion efficiency reported in CQD solar cells to date has been achieved by using band alignment engineering and graded doping architectures.<sup>42</sup> These types of devices can be extensions of the heterojunction or homo-

junction architectures in which control over both the dopant type and magnitude, as well as conduction band edge positions, in CQD films is achieved, usually through different ligand schemes. Taking inspiration from polycrystalline devices employing p–i–n, p<sup>+</sup>–n–n<sup>+</sup>, and related structures, graded doping architectures seek to increase cell voltages using the larger Fermi level splitting associated with higher doping levels.

They also have the goal of increasing current collection using back fields.

Figure 21a illustrates the different operating regions of a graded doping quantum junction architecture using Mott–Schottky analysis. This device consisted of a thin, highly doped ( $10^{19} \text{ cm}^{-3}$ ) p-type PbS CQD layer followed by lightly doped ( $10^{16} \text{ cm}^{-3}$ ) and highly doped ( $10^{17} \text{ cm}^{-3}$ ) n-type PbS CQD layers.<sup>187</sup> The addition of the top highly doped n-type layer introduced an electric field in the back of the device that aided in carrier extraction and allowed for increased quasi-Fermi level splitting and operating voltage. The different doping levels were achieved by using different ligand strategies (tetramethylammonium hydroxide for the p-type layer and different amounts of tetrabutylammonium bromide treatment for the n-type layer).

Graded doping schemes have also been implemented in heterojunction architectures. One study employed the ligand 3-mercaptopropionic acid to make a lightly doped ( $10^{15} \text{ cm}^{-3}$ ) PbS CQD film and used this film in a p<sup>+</sup>–p–n architecture to realize a heterojunction solar cell with a PCE of over 7%.<sup>188</sup> Another study used a highly doped CuI thin film as the p-type layer in a p–i–n solar cell where the intrinsic layer was composed of PbSe CQDs and the n-type layer was ZnO.<sup>189</sup>

High performance was achieved in a study that used different CQD ligand treatments to control both the doping levels and band alignment in a ZnO–PbS CQD solar cell.<sup>42</sup> A band diagram and optimized device structure are shown in Figure 21b. The addition of the top EDT-treated PbS CQD layer introduced additional band bending into the device, which helped prevent electrons from flowing in the wrong direction. A champion device achieved a certified solar PCE of 8.55%, and the devices also exhibited long-term air stability as shown in Figure 21c. The stability was attributed to the use of inorganic-ligand-passivated CQDs as the light-absorbing layer and removal of the interfacial MoO<sub>3</sub> layer at the Ohmic contact interface.

## 5.7. Electrical Contact Development

Engineering of both electron-collecting and hole-collecting electrodes in different CQD solar cell architectures has received much attention in the field. Advances in electrode technology have been important in facilitating performance advances. Much of the attention has focused on achieving trap-free interfaces and ideal band alignment, and it seems likely that there are more performance benefits to be gained from those areas in the future.

**5.7.1. Strategies To Improve Hole Collection.** Strategies to improve hole collection in CQD solar cells have primarily focused on engineering of the top Ohmic contact to p-type CQD films. Initial studies of heterojunction architectures used gold as the deep work function top reflective contact.<sup>170</sup> Further studies aimed at reducing the use of this high-cost material found that nickel could act as a suitable replacement if a LiF interlayer was added to prevent reactions and degradation of the metal–semiconductor interface.<sup>190</sup>

The introduction of n-type transition-metal oxides consisting of V<sub>2</sub>O<sub>x</sub> or especially MoO<sub>x</sub> resulted in significant performance advances. One study found that MoO<sub>x</sub> acts as a hole extraction layer by enhancing band-bending at the PbS CQD interface and providing hole transport levels through oxygen vacancies,<sup>191</sup> as illustrated in Figure 22a. Another study found that the deep work function MoO<sub>x</sub> can remove a reverse-bias Schottky diode otherwise present at the CQD–metal interface by pinning the

Fermi level of the top contact.<sup>192</sup> Both studies found that including MoO<sub>x</sub> improved the solar cell open-circuit voltage. A comparison of device performance with several different top contact materials is shown in Figure 22b.

Nickel oxide has also been used as a hole-transporting photocathode in heterojunction CQD solar cells.<sup>193</sup> Sputtered NiO can be used in a bottom-illuminated architecture, or the architecture can be inverted with the use of sol–gel NiO as the bottom hole-transporting layer and nanocrystal ZnO as the top electron-transporting layer.

**5.7.2. Strategies To Improve Electron Collection.** The majority of the focus on engineering electrodes in CQD solar cells has been on the electron-collecting layers, due to the success of the heterojunction architecture employing p-type CQD films. Particular attention has been paid to optimizing the properties of the n-type TiO<sub>2</sub> and ZnO layers for better heterojunction performance. To explore the importance of band offsets between CQD films with different band gaps and the TiO<sub>2</sub> acceptor, a sol–gel-derived TiO<sub>2</sub> precursor was doped with impurities.<sup>194</sup> The optimal band offset resulted in the efficient extraction of carriers even in the absence of a strong electric field. A similar method using magnesium doping was used to tune the ZnO conduction band position and reduce voltage losses associated with the ZnO conduction band tail.<sup>195</sup>

Recombination at the metal oxide–semiconductor interface is also an area of ongoing concern in heterojunction CQD solar cells. Several strategies have been used to overcome this performance-limiting process. The introduction of a thin ZnO buffer layer between the CQD film and TiO<sub>2</sub> electrode was found to result in a nearly 2-fold reduction of the interface recombination rate.<sup>196</sup> [6,6]-Phenyl-61-butanoic acid methyl ester (PCBM) can also be used as a buffer layer and electron transport layer at the same interface due to its low trap state density and favorable band alignment.<sup>197</sup> The introduction of a PCBM interface layer into a depleted heterojunction CQD solar cell resulted in a champion device PCE of 8.9%.<sup>197</sup>

Doping ZnO with nitrogen was also found to reduce the carrier concentration in the metal oxide in a heterojunction CQD solar cell.<sup>198</sup> This method suppressed PbS/ZnO interface recombination, resulting in a 50% improvement in  $V_{oc}$  and PCE. Parts c and d of Figure 22 show photovoltage decay measurements on undoped and nitrogen-doped ZnO–PbS and ZnO–PbSe solar cells, illustrating the large change in recombination rate for the doped ZnO in the PbS solar cell.

The electron-accepting electrode can be engineered to increase the width of the depletion region in the CQD film by employing the donor-supply electrode (DSE) concept.<sup>199</sup> The DSE consists of a highly doped, shallow work function electrode that enhances the free carrier density in the n-type electrode through charge injection doping. Energy band diagrams illustrating the DSE concept are shown in Figure 22e. This concept was first used in the field to overcome the limitations associated with low-temperature TiO<sub>2</sub> electrodes for applications in small-band-gap CQD cells.<sup>199</sup> An implementation consisting of shallow work function FTO and thin atomic-layer-deposited TiO<sub>2</sub> later resulted in a champion device efficiency of 8.5%.<sup>200</sup> A cross-sectional SEM image of a heterojunction CQD solar cell employing the DSE strategy is shown in Figure 22d, and current density–voltage and EQE curves are shown in Figure 22e,f for DSE and control devices.

Many other strategies to optimize the electron-collecting electrode for specific applications have been developed. A solution-processed zinc oxide layer based on a diethyl zinc

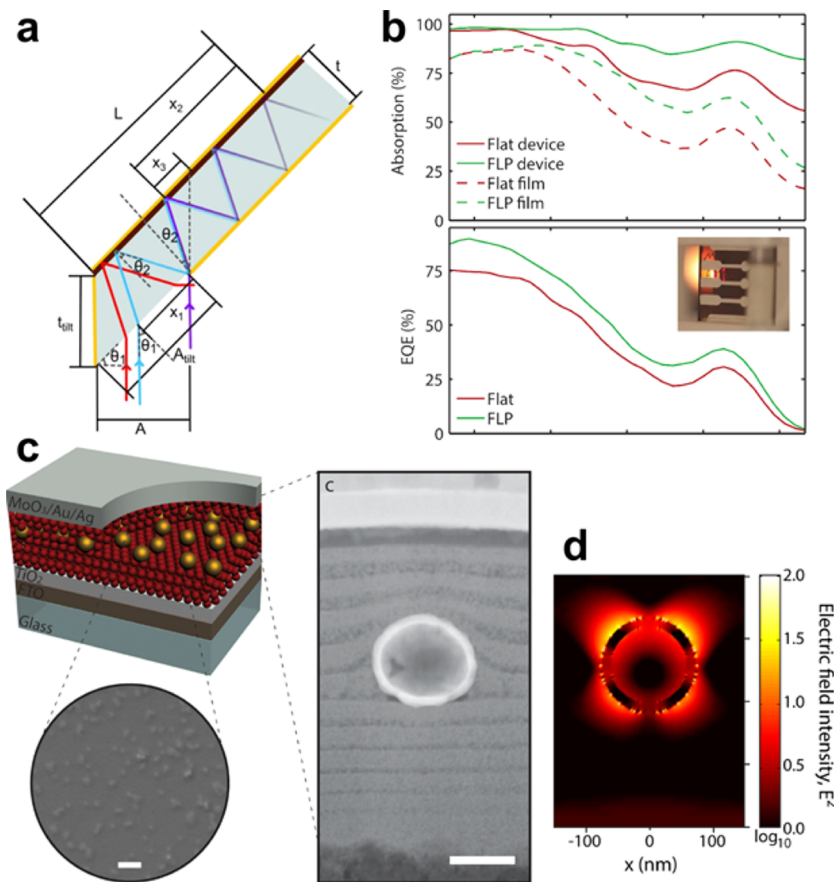


**Figure 23.** Light trapping in CQD solar cells. (a) Geometric configuration of a folded light path solar cell. (b) Absorption (top) and EQE (bottom) for device (solid lines) and CQD film (dashed lines) flat (red) and folded (green) light path samples. Inset: photograph of a tilted sample illuminated through the device aperture at  $45^\circ$  with a thin strip of white light demonstrating the capturing of multiple passes of light; in this case the third and fifth passes can be clearly observed. Panels a and b reprinted with permission from ref 203. Copyright 2013 Macmillan Publishers Ltd. (c) (Top left) Schematic of a PbS CQD device with embedded plasmonic gold nanoshells. (Bottom left) Top-view SEM image showing the representative density of nanoshells after CQD deposition. Scale bar 1  $\mu\text{m}$ . (Right) Cross-sectional TEM image showing a single gold nanoshell embedded in a PbS CQD film. Scale bar 100 nm. (d) FDTD simulation of the electric field intensity ( $E^2$ ) profile in the plasmonic film from c on a log scale at the CQD exciton wavelength,  $\lambda = 950$  nm. Panels c and d adapted from ref 208. Copyright 2013 American Chemical Society.

precursor was used to realize an inverted heterojunction architecture in which the light absorption profile could be tailored for optimal absorption in thin CQD films.<sup>201</sup> ZnO nanowire arrays were grown on a graphene transparent conductive oxide (TCO) base to enable flexible CQD devices.<sup>202</sup> As new advances in CQD films and materials are made, concurrent engineering of the electrode layers will continue to be necessary.

### 5.8. Optical Engineering of CQD Solar Cells

Colloidal quantum dots are strong absorbers, with absorption coefficients for PbS CQDs reaching values of above  $10^5 \text{ cm}^{-1}$  at blue wavelengths.<sup>40</sup> However, at infrared wavelengths near the band gap energy, CQD solar cells still must contend with the absorption–extraction compromise, whereby absorption lengths exceed charge transport lengths in CQD films. Light trapping, or effectively increasing optical path lengths in the absorbing material through structuring, is one method to overcome this compromise. Several different light-trapping methods have been used to increase performance in CQD solar cells, including geometrical optics schemes, nanophotonic structuring, and plasmonic enhancement.

#### 5.8.1. Geometric and Nanophotonic Light Trapping.

Geometric schemes to increase absorption in CQD solar cells

have concentrated on increasing the number of effective passes that a photon takes through the absorbing material. The conventional planar cell is a double-pass design, in which light enters the cell, passes through the absorbing material, experiences reflection at the back contact, and passes through the absorbing material once more before leaving the cell. A double-pass structure can be converted into a multipass structure by tilting the cell and using a folded light path design,<sup>203</sup> creating micrometer-scale pyramids in the bottom electrode<sup>204</sup> or structuring the TCO to create diffraction gratings.<sup>205</sup> The folded light path design is illustrated in Figure 23a,b.

Nanophotonic structuring has also been used as a light-trapping method in CQD solar cells. Scalable fabrication methods such as nanoimprint lithography<sup>206</sup> and nanosphere lithography<sup>207</sup> can be applied to structure the bottom electrodes on a submicrometer scale. These designs take advantage of light localization and waveguiding provided by the periodic photonic structures to enhance absorption and consequently the photocurrent in photovoltaic devices.

#### 5.8.2. Plasmonic Enhancement of CQD Solar Cells.

CQD solar cells are uniquely suited to benefit from absorption enhancements via plasmonic effects. Surface plasmon resonances, in which localized collective electron oscillations near a

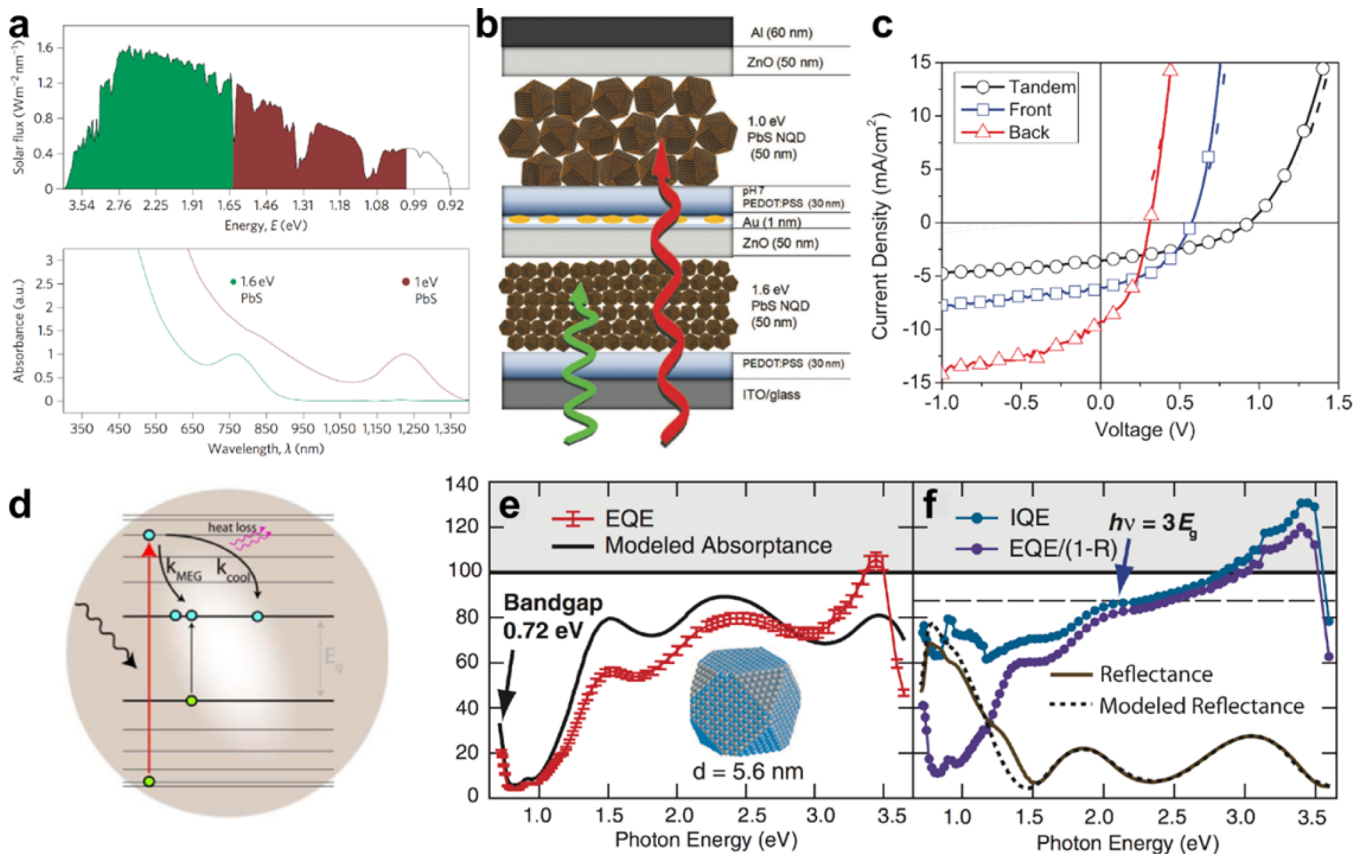


**Figure 24.** Advanced concepts—tandem and multiple-exciton-generation cells. (a) Spectral utilization (top) and absorption spectra (bottom) for CQD tandem solar cells having quantum-confined band gaps of 1.6 eV (green) and 1.0 eV (red). Reprinted with permission from ref 216. Copyright 2011 Macmillan Publishers Ltd. (b) Schematic of a proposed tandem cell with optimum combination of PbS CQD band gaps. (c)  $J$ – $V$  characteristic of the tandem cell shown in (b) and corresponding control single-junction devices. The tandem cell exhibits a  $V_{oc}$  that is the sum of the  $V_{oc}$  values of the subcells. Panels b and c reprinted with permission from ref 217. Copyright 2011 Wiley-VCH Verlag GmbH & Co. KGaA. (d) Illustration of multiple-exciton generation (MEG) in a quantum dot. Hot carriers undergo one of two competing processes: generation of an extra e–h pair ( $k_{MEG}$ ) or cooling of the single-exciton state ( $k_{cool}$ ). Reprinted from ref 222. Copyright 2012 American Chemical Society. (e) Measured EQE and modeled absorptance curves for a PbSe CQD solar cell with a diameter of 5.6 nm and an associated band gap of 0.72 eV. (f) IQE for the cell in (e) calculated either from  $\text{EQE}/(1 - R)$  (purple curve) or from  $\text{EQE}/A$  (blue curve), where  $A$  is the modeled absorptance of the PbSe plus ZnO layers. The modeled reflectance is shown as a dashed black line. Values of IQE over 100 represent MEG contributions to the solar cell performance. Panels e and f reprinted with permission from ref 228. Copyright 2011 American Association for the Advancement of Science.

metal–dielectric interface or at the surface of a metal particle couple strongly to electromagnetic fields, have been used to improve CQD solar cell performance. One of the advantages of the low-temperature solution-phase processing of CQDs is the ease with which they can be combined with other nanomaterials. Plasmonic metal nanoparticles offer both chemical compatibility and complementary functionality. These nanostructures are extremely sensitive to their local optical environment, offering the possibility to tune or enhance the overall absorption of other materials in their vicinity. Like CQDs, they can be synthesized in the solution phase and colloidally stabilized through the use of surfactants. The energy of plasmonic nanoparticle resonances can be tuned by changing the size and shape of the nanoparticles. This effect can be used to target the more weakly absorbing portions of the CQD film spectra and enhance performance in the spectral regions most affected by the absorption–extraction compromise. The noble metals (particularly gold and silver) are popular materials for plasmonic nanostructures, although in principle any conductor can exhibit plasmonic effects.

Plasmonic nanoparticles can be integrated into CQD films to act as resonant optical antennas at targeted wavelengths. One

such device based on plasmonic gold nanoshells embedded in a PbS CQD solar cell<sup>208</sup> is shown in Figure 23c. Figure 23d shows the electric field profile surrounding the gold nanoshell, calculated using finite-difference time domain (FDTD) simulations, indicating expected enhancement at the wavelengths that are minimally absorbed in the CQD film. The addition of the plasmonic nanoshells resulted in a 35% maximum enhancement in photocurrent in the performance-limiting infrared wavelength regime and a resultant power conversion efficiency improvement of 11% over that of a nonplasmonic control device. The strong confinement of radiation modes provided by ultrasmall plasmonic nanoparticles has been demonstrated as well in a device that rapidly transfers hot electrons produced in 5 nm diameter gold particles to PbS CQDs.<sup>209</sup> This near-field energy transfer scheme resulted in a 41% increase in the short-circuit current and a 5% increase in the power conversion efficiency compared to those of a nonplasmonic device.

Plasmonic nanostructures can also be used simultaneously as both absorption enhancers and integrated junction elements in CQD solar cells. Silver plasmonic particles have been used as the Schottky contacts in a CQD solar cell,<sup>210</sup> where they acted

both as part of the charge-separating junction and to enhance absorption at the spatial region of maximum internal quantum efficiency (IQE) in the cell. An all-inorganic bulk nano-heterojunction cell design that used plasmonic iron pyrite nanocubes as one of the heterojunction materials showed both enhanced absorption and charge separation and transport efficiency compared to a layered structure due to the intimate contact and overlap of the optical fields between the different nanomaterials.<sup>211</sup>

Additional studies on plasmonic–CQD systems have targeted better incoupling and photoluminescence efficiency in CQD arrays. These include the realization of plasmonic grating structures that couple incident light to surface plasmon polariton modes propagating at the metal–CQD film interface<sup>212</sup> and the demonstration of a 15-fold enhancement in the photoluminescence intensity of a plasmonic–CQD system constructed using colloidal self-assembly and metal evaporation.<sup>213</sup> These results indicate that further improvements in CQD solar cell performance should be possible with tailored engineering of the spectral and energetic landscape of coupled plasmonic–quantum dot systems.

### 5.9. CQD Solar Cell Concepts beyond the Single-Junction Limit

Much progress has been made in developing CQD solar cell architectures since the first device demonstrations in 2005. All of the previously described advances have been made within the traditional single-junction framework which is described by the Shockley–Queisser power conversion efficiency limit.<sup>214</sup> One of the main potential applications of CQDs as a photovoltaic material is the possibility of realizing advanced effects in solar cells by taking advantage of the discrete energy band structure and quantum size effect tunability offered by CQD materials. The following sections describe several efforts to use CQDs in solar cell concepts that go beyond the Shockley–Queisser limit.

**5.9.1. Multiple-Junction CQD Solar Cells.** Solar cell materials with different band gaps can be stacked and connected through ideal recombination layers to absorb more of the solar spectrum and exceed the single-junction efficiency limit.<sup>169</sup> One of the main barriers to realizing high-performing and cost-efficient multiple-junction photovoltaics is the difficulty in finding a materials system with the requisite band gap tuning range. High efficiencies have been achieved in multijunction cells based on the III–V materials system.<sup>215</sup> These materials are grown by epitaxial methods, and much care must be taken in lattice-matching the different materials. The high costs of such systems currently limit them to niche applications, such as in space exploration. CQDs have the potential to solve this problem. Their band gap tunability provided by the quantum size effect offers the potential to fabricate tandem solar cells out of a single materials system without the added complication of lattice-matched growth. Figure 24a shows the spectral utilization and absorption spectra for a tandem architecture employing CQDs with band gaps of 1.0 and 1.6 eV.<sup>216</sup> CQDs could potentially be used on their own or in tandem with other materials to extend the absorption range of multijunction cells to infrared wavelengths. The main technical challenge in developing multijunction CQD photovoltaics is developing appropriate recombination layers for individual current-matched cells.

Proof-of-principle PbS CQD tandem solar cells demonstrating voltage addition employed two different recombination layer strategies. One used gold islands as the recombination

layer in an inverted heterojunction architecture.<sup>217</sup> The device structure is illustrated in Figure 24b, and Figure 24c shows the current–voltage characteristics for the individual and tandem cells. The other tandem demonstration used a graded recombination layer in a depleted heterojunction architecture.<sup>216</sup> Both studies took care in optimizing the individual cells and satisfying the current-matching condition in the tandem device to achieve improved performance over the individual constituent cells.

Further progress in all-CQD multijunction cells will require development in recombination layer technology which could be aided by low-temperature film formation techniques such as atomic layer deposition.<sup>196,200</sup> Additionally, the ability to tune CQD materials over a wide wavelength range and their facile solution-processed deposition methods make them of particular interest as the infrared cell layers in hybrid systems composed of multiple materials.

**5.9.2. Hot Carrier Effects in CQD Solar Cells.** Hot carrier loss is an important performance-limiting mechanism in single-junction solar cells.<sup>214</sup> Hot carriers, electrons and holes that are excited with photon energies larger than the band gap energy, usually relax to their respective band edges via phonon emission rapidly. In quantum-confined materials such as CQDs, the relative scarcity of available states can slow this process,<sup>218</sup> possibly providing a pathway to capturing the energy in excess of the fundamental excitonic transition. This extra energy could potentially be harvested using either hot carrier solar cell concepts or multiple-exciton generation (MEG), as discussed below.

Hot electrons could in theory be harvested directly in a hot carrier solar cell, where selective contacts would be used to extract carriers at energies above the band gap energy before relaxation to the band edge occurs.<sup>219</sup> The first step in realizing such a device is increasing the hot carrier lifetime. Slow cooling in CQDs has been demonstrated in core–shell CQDs,<sup>220</sup> and hot electron transfer from PbSe CQDs to titania films has been observed.<sup>221</sup> These early reports demonstrate a path toward using CQDs in a hot carrier solar cell.

Another method of extracting energy from hot carriers in solar cells is to use MEG. MEG occurs in semiconductors when excitons with energy greater than twice the band gap energy relax to the band edge by exciting an additional electron–hole pair through impact ionization.<sup>222</sup> In an ideal MEG solar cell, EQE would exceed 100% for energies greater than twice the band gap energy because high-energy photons could produce more than one photocarrier pair. If a threshold of twice the band gap energy could be realized for impact ionization in a CQD solar cell, the theoretical maximum power conversion efficiency would shift to above 60%.<sup>223</sup>

Figure 24d illustrates the MEG process in a quantum dot. MEG is expected to be more efficient in quantum-confined nanostructures compared to bulk semiconductors because the momentum conservation requirement is relaxed and carrier–carrier interactions are larger due to strong confinement in the nanostructure.<sup>222</sup> Another potential effect in quantum-confined materials is the decoupling of the carrier multiplication profile from the effective band gap, allowing increased photovoltages for equivalent carrier multiplication yields in nanocrystalline compared to bulk materials.<sup>224</sup> In PbSe, MEG has been shown to occur with approximately twice the efficiency in isolated quantum dots compared to in the bulk material, indicating that MEG may be a promising route to increasing solar cell efficiency.<sup>225–227</sup>

Table 3. Champion Colloidal Quantum Dot Photovoltaic Device Details

description	material stack	ligand	exciton peak (nm)	number of junctions	power conversion efficiency (%)	certified?
Schottky <sup>168</sup>	ITO/PbS/LiF/Al	1,4-benzenedithiol	1100	1	5.2	N
heterojunction <sup>123</sup>	TiO <sub>2</sub> /PbS	MPA and CdCl <sub>2</sub>	950	1	7.0	Y
p-i-n <sup>42</sup>	ZnO/PbS/PbS	TBAI/EDT	935	1	8.6	Y
fused heterojunction <sup>130</sup>	TiO <sub>2</sub> /PbS	MPA and CdCl <sub>2</sub>	1000	1	9.2	N
tandem <sup>216</sup>	TiO <sub>2</sub> /PbS/recombination stack/PbS	MPA	800/1250	2	4.2	N

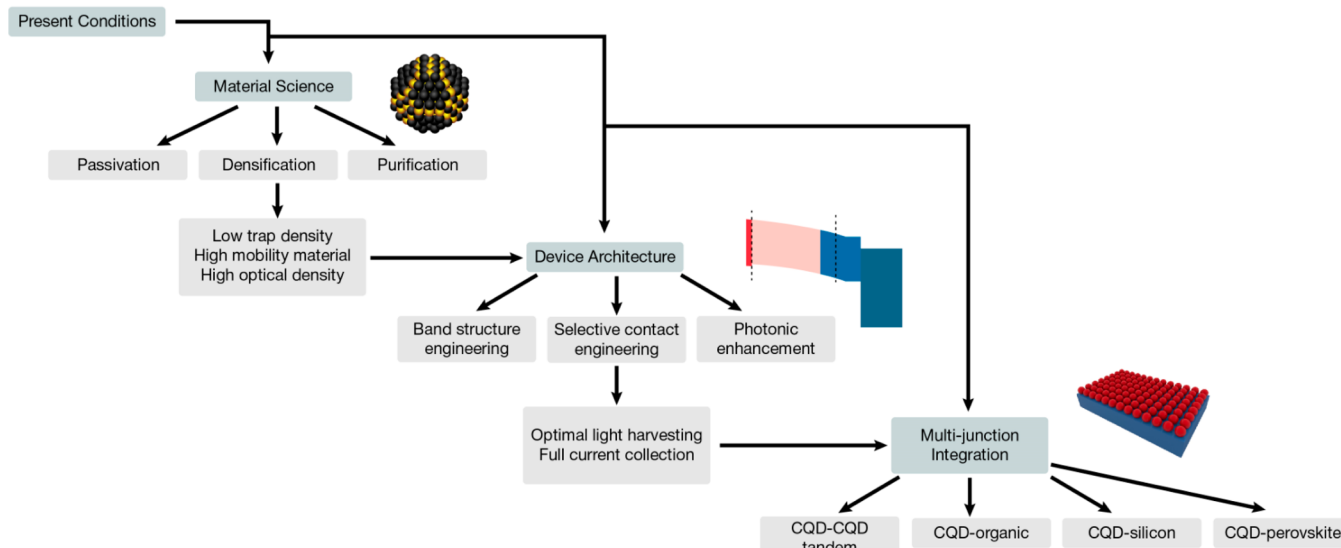


Figure 25. Pathways forward for CQD photovoltaics.

The first MEG CQD solar cell exhibiting EQE over 100% was demonstrated in 2011.<sup>228</sup> The cell used a hydrazine surface treatment on PbSe CQDs to increase the MEG efficiency such that multiple carriers contributed to the photocurrent for absorbed short-wavelength photons. Parts e and f of Figure 24 show plots of EQE, IQE, and absorbance for the PbSe MEG solar cells. This demonstration of useful MEG is a promising step for third-generation photovoltaic devices.

In addition, CQDs can act as acceptors for hot carrier products generated in other materials. Singlet exciton fission to produce spin-triplet excitons in organic semiconductors can be considered an analogue to MEG in inorganic semiconductors.<sup>229</sup> Recent demonstrations have shown effective transfer of spin triplets generated in pentacene<sup>230</sup> and tetracene<sup>231</sup> to PbSe and PbS CQDs, respectively. These studies opened new avenues to coupling organic and inorganic materials in hybrid devices.

## 6. CONCLUSION

Recent colloidal quantum dot research has led to significant advances in synthesis methods, in material and film processing techniques, and in characterization and optimization of optoelectronic properties. These have enabled the realization of solution-processed photovoltaic devices with certified power conversion efficiencies recently reaching 9.2%. Champion CQD photovoltaic devices are summarized in Table 3.

Continued progress in the field (Figure 25) will rely on progress in three key areas.

The first strives to synthesize a population of perfect quantum dots, and to produce perfect quantum dot films from

them; fulfilling this prescription will rely on expertise in materials science and materials chemistry. While large strides have been made in recent years to improve quantum dot surface passivation, orders of magnitude remain between the defect density levels observed in bulk semiconductors and the best quantum dot solids to date. Studies of novel passivation strategies, including new or hybrid ligand systems, surface engineering, core/shell strategies, and self-healing surfaces, will reduce trap states, improve carrier transport, and reduce the extent of energy level pinning. A second route to improved electronic transport in quantum dot films will rely on densifying nanocrystal films through improved packing and, ideally, ordering. Such films will eliminate diversity in path length and thus tortuosity in charge transport through the device. Improvements in this area will be driven by actively engineering order-generating quantum dot surfaces, and by careful work to achieve a higher degree of film purity, with extraneous chemical species eliminated from the quantum dot film.

The second pillar of research focuses on constructing the most efficient device architecture using a given material. Advances in this area have led to the most recent record CQD solar cell efficiencies, and will continue to have vital influence over progress in the field as a whole. Studies must focus on optimizing both light and photocurrent management, the goal being full capture of all incident energy, and the high-yield conveyance of the resultant photogenerated charge to an external circuit. This will rely on careful engineering of the band structure of the quantum film in concert with that of selective top and bottom electrodes. Significant studies have been performed on the electron-transporting component (trans-

parent conductive metal oxides, typically), yet as the optoelectronic quality of the quantum dot solid improves, even greater enhancements will be required in both the electron- and hole-accepting layers to ensure optimal performance. Research will need to adjust existing systems or apply novel material solutions, while intensely studying the interfaces between the quantum dot film and electrodes to eliminate any potential losses. Photonic enhancements will be required to further increase absorption in a given thickness of light-absorbing material.

Finally, as single-junction quantum dot solar cells advance and improve, a renewed focus will be placed on multiple-junction integration, with the goal of creating high-efficiency devices through improved spectral utilization and minimal loss associated with photocarrier thermalization. Tandem and triple-junction all-CQD solar cells will exploit control over quantum dot size to maximize spectral capture efficiency and boost device voltage. It may be particularly attractive to combine CQDs, distinctive among solution-processed materials in their infrared-harvesting capability, with established solar technologies such as crystalline silicon, or with novel large-gap solar technologies such as lead halide perovskites.

The past few years have seen a deepening in understanding—through a combination of experimental and computational studies—of how quantum dots and ligands, through their composition and binding, lead to rationally described transport, trapping, and consequent device performance. While the recent meteoric rise of perovskite photovoltaic devices has raised concerns from some in the field, we contend that these two platforms offer more value as complementary rather than competing research paths. Each platform has advantages and drawbacks: while perovskites hold the edge in efficiency, with certified values over 20%, quantum dot films exhibit significantly greater stability over time, and offer band gap tunability into the infrared. Continued progress in the fundamental physical chemistry and device physics of both CQD and perovskite devices will be mutually beneficial, with many insights applying to each platform. Colloidal quantum dot photovoltaics remains a highly relevant, rapidly progressing field with the opportunity to compete within a growing, highly diverse solar marketplace.

## AUTHOR INFORMATION

### Corresponding Author

\*E-mail: ted.sargent@utoronto.ca.

### Notes

The authors declare no competing financial interest.

## Biographies



Graham H. Carey received a B.Sc. Hons. (chemistry and physics) from Dalhousie University in 2010, and is nearing completion of a Ph.D. (electrical engineering and environmental studies) under Prof. Ted Sargent at the University of Toronto. Graham's research has focused on the intersection of electrical transport, surface passivation, and impurity management in colloidal quantum dot solids.



Ahmed L. Abdelhady is a postdoctoral fellow at the Solar & Photovoltaics Engineering Research Center, King Abdullah University of Science and Technology (KAUST), Saudi Arabia. He holds a B.Sc. in chemistry from Mansoura University, Egypt (2002), as well as a Ph.D. in inorganic chemistry from The University of Manchester, United Kingdom (2011), under the supervision of Prof. Paul O'Brien. After he completed his Ph.D., he became a Lecturer of Inorganic Chemistry at Mansoura University. In 2013 he joined Prof. Osman Bakr's Functional Nanomaterials Lab. His current research is focused on quantum dots and hybrid perovskite synthesis and characterization.



Zhijun Ning received his Ph.D. degree from the Department of Applied Chemistry, East China University of Science and Technology, under the supervision of Prof. He Tian. From 2009 to 2011, he worked as a postdoctoral scholar at the Royal Institute of Technology, Sweden. From 2011 to 2014, he was a postdoctoral scholar in the Department of Electrical and Computer Engineering at the University of Toronto, under the supervision of Prof. Edward H. Sargent. Since December 2014, he has been an Assistant Professor (tenure-track) in the School of Physical Science and Technology, ShanghaiTech University. He is a participant in the Young 1000 Talent Program. His current research interests include the synthesis and application of novel optoelectronic materials such as nanocrystals, organic–inorganic hybrid perovskites, and organic molecules for solar cells, displays, and photodetectors.



Susanna M. Thon received her B.S. in physics from the Massachusetts Institute of Technology in 2005, and completed her Ph.D. in physics at the University of California, Santa Barbara, in 2010. From 2011 to 2013, she was a postdoctoral fellow at the University of Toronto. She is currently an Assistant Professor of Electrical and Computer Engineering at Johns Hopkins University. Her research interests include photonic, materials, and device engineering for nanostructured optoelectronics.



Osman M. Bakr is an Assistant Professor of Materials Science and Engineering, SABIC Presidential Career Development Chair, at the King Abdullah University of Science and Technology (KAUST), Saudi Arabia. He holds a B.Sc. in materials science and engineering from the Massachusetts Institute of Technology (2003) as well as M.S. and Ph.D. degrees in applied physics from Harvard University (2009). He was a postdoctoral fellow in the Laboratory for Nanoscale Optics at Harvard University. In 2010 he moved to KAUST and founded the Functional Nanomaterials Lab, a research group dedicated to the study of nanoparticles and hybrid nanomaterials, particularly advancing their

synthesis and self-assembly for applications in photovoltaics, optoelectronics, and photocatalysis.



Edward H. Sargent received his B.Sc.Eng. (engineering physics) from Queen's University in 1995 and his Ph.D. in electrical and computer engineering (photonics) from the University of Toronto in 1998. He holds the rank of Professor in the Edward S. Rogers Sr. Department of Electrical and Computer Engineering at the University of Toronto, where he holds the Canada Research Chair in Nanotechnology. He is a Fellow of the American Association for the Advancement of Science (AAAS) and a Fellow of the Institute of Electrical and Electronics Engineers (IEEE).

## REFERENCES

- (1) Konstantatos, G.; Howard, I.; Fischer, A.; Hoogland, S.; Clifford, J.; Klem, E.; Levina, L.; Sargent, E. H. Ultrasensitive Solution-Cast Quantum Dot Photodetectors. *Nature* **2006**, *442*, 180–183.
- (2) Huang, L.; Tu, C.-C.; Lin, L. Y. Colloidal Quantum Dot Photodetectors Enhanced by Self-Assembled Plasmonic Nanoparticles. *Appl. Phys. Lett.* **2011**, *98*, 113110.
- (3) Keuleyan, S.; Lhuillier, E.; Brajuskovic, V.; Guyot-Sionnest, P. Mid-Infrared HgTe Colloidal Quantum Dot Photodetectors. *Nat. Photonics* **2011**, *5*, 489–493.
- (4) Li, L.; Pandey, A.; Werder, D. J.; Khanal, B. P.; Pietryga, J. M.; Klimov, V. I. Efficient Synthesis of Highly Luminescent Copper Indium Sulfide-Based Core/Shell Nanocrystals with Surprisingly Long-Lived Emission. *J. Am. Chem. Soc.* **2011**, *133*, 1176–1179.
- (5) Steckel, J. S.; Coe-Sullivan, S.; Bulović, V.; Bawendi, M. G. 1.3  $\mu\text{m}$  to 1.55  $\mu\text{m}$  Tunable Electroluminescence from PbSe Quantum Dots Embedded within an Organic Device. *Adv. Mater.* **2003**, *15*, 1862–1866.
- (6) Qian, L.; Zheng, Y.; Xue, J.; Holloway, P. H. Stable and Efficient Quantum-Dot Light-Emitting Diodes Based on Solution-Processed Multilayer Structures. *Nat. Photonics* **2011**, *5*, 543–548.
- (7) Donegá, C. de M. Synthesis and Properties of Colloidal Heteronanocrystals. *Chem. Soc. Rev.* **2011**, *40*, 1512–1546.
- (8) Murray, C. B.; Norris, D. J.; Bawendi, M. G. Synthesis and Characterization of Nearly Monodisperse CdE (E = Sulfur, Selenium, Tellurium) Semiconductor Nanocrystallites. *J. Am. Chem. Soc.* **1993**, *115*, 8706–8715.
- (9) Park, J.; Joo, J.; Kwon, S. G.; Jang, Y.; Hyeon, T. Synthesis of Monodisperse Spherical Nanocrystals. *Angew. Chem., Int. Ed.* **2007**, *46*, 4630–4660.
- (10) Thanh, N. T. K.; Maclean, N.; Mahiddine, S. Mechanisms of Nucleation and Growth of Nanoparticles in Solution. *Chem. Rev.* **2014**, *114*, 7610–7630.
- (11) Kumar, S.; Nann, T. Shape Control of II–VI Semiconductor Nanomaterials. *Small* **2006**, *2*, 316–329.
- (12) Burda, C.; Chen, X.; Narayanan, R.; El-Sayed, M. A. Chemistry and Properties of Nanocrystals of Different Shapes. *Chem. Rev.* **2005**, *105*, 1025–1102.

- (13) Reiss, H. The Growth of Uniform Colloidal Dispersions. *J. Chem. Phys.* **1951**, *19*, 482–487.
- (14) De Smet, Y.; Deriemaeker, L.; Finsy, R. A Simple Computer Simulation of Ostwald Ripening. *Langmuir* **1997**, *13*, 6884–6888.
- (15) Talapin, D. V.; Rogach, A. L.; Haase, M.; Weller, H. Evolution of an Ensemble of Nanoparticles in a Colloidal Solution: Theoretical Study. *J. Phys. Chem. B* **2001**, *105*, 12278–12285.
- (16) Yin, Y.; Alivisatos, A. P. Colloidal Nanocrystal Synthesis and the Organic–Inorganic Interface. *Nature* **2005**, *437*, 664–670.
- (17) García-Rodríguez, R.; Hendricks, M. P.; Cossairt, B. M.; Liu, H.; Owen, J. S. Conversion Reactions of Cadmium Chalcogenide Nanocrystal Precursors. *Chem. Mater.* **2013**, *25*, 1233–1249.
- (18) Van Embden, J.; Mulvaney, P. Nucleation and Growth of CdSe Nanocrystals in a Binary Ligand System. *Langmuir* **2005**, *21*, 10226–10233.
- (19) Huang, J.; Kovalenko, M. V.; Talapin, D. V. Alkyl Chains of Surface Ligands Affect Polypyramidal CdSe Nanocrystals and Play an Important Role in the Synthesis of Anisotropic Nanoheterostructures. *J. Am. Chem. Soc.* **2010**, *132*, 15866–15868.
- (20) Manna, L.; Scher, E. C.; Alivisatos, A. P. Synthesis of Soluble and Processable Rod-, Arrow-, Teardrop-, and Tetrapod-Shaped CdSe Nanocrystals. *J. Am. Chem. Soc.* **2000**, *122*, 12700–12706.
- (21) Qu, L.; Peng, X. Control of Photoluminescence Properties of CdSe Nanocrystals in Growth. *J. Am. Chem. Soc.* **2002**, *124*, 2049–2055.
- (22) Talapin, D. V.; Lee, J.-S.; Kovalenko, M. V.; Shevchenko, E. V. Prospects of Colloidal Nanocrystals for Electronic and Optoelectronic Applications. *Chem. Rev.* **2009**, *110*, 389–458.
- (23) Kwon, S. G.; Piao, Y.; Park, J.; Angappane, S.; Jo, Y.; Hwang, N.-M.; Park, J.-G.; Heyon, T. Kinetics of Monodisperse Iron Oxide Nanocrystal Formation by “Heating-Up” Process. *J. Am. Chem. Soc.* **2007**, *129*, 12571–12584.
- (24) Pan, J.; El-Ballouli, A. O.; Rollny, L.; Voznyy, O.; Burlakov, V. M.; Goriely, A.; Sargent, E. H.; Bakr, O. M. Automated Synthesis of Photovoltaic-Quality Colloidal Quantum Dots Using Separate Nucleation and Growth Stages. *ACS Nano* **2013**, *7*, 10158–10166.
- (25) Tagliazucchi, M.; Tice, D. B.; Sweeney, C. M.; Morris-Cohen, A. J.; Weiss, E. A. Ligand-Controlled Rates of Photoinduced Electron Transfer in Hybrid CdSe Nanocrystal/Poly(viologen) Films. *ACS Nano* **2011**, *5*, 9907–9917.
- (26) Sambur, J. B.; Riha, S. C.; Choi, D.; Parkinson, B. A. Influence of Surface Chemistry on the Binding and Electronic Coupling of CdSe Quantum Dots to Single Crystal TiO<sub>2</sub> Surfaces. *Langmuir* **2010**, *26*, 4839–4847.
- (27) King, L. A.; Riley, D. J. Importance of QD Purification Procedure on Surface Adsorbance of QDs and Performance of QD Sensitized Photoanodes. *J. Phys. Chem. C* **2012**, *116*, 3349–3355.
- (28) Kalyuzhny, G.; Murray, R. W. Ligand Effects on Optical Properties of CdSe Nanocrystals. *J. Phys. Chem. B* **2005**, *109*, 7012–7021.
- (29) Shen, Y.; Gee, M. Y.; Tan, R.; Pellechia, P. J.; Greystak, A. B. Purification of Quantum Dots by Gel Permeation Chromatography and the Effect of Excess Ligands on Shell Growth and Ligand Exchange. *Chem. Mater.* **2013**, *25*, 2838–2848.
- (30) Shen, Y.; Tan, R.; Gee, M. Y.; Greystak, A. B. Quantum Yield Regeneration: Influence of Neutral Ligand Binding on Photophysical Properties in Colloidal Core/Shell Quantum Dots. *ACS Nano* **2015**, *9*, 3345–3359.
- (31) Wang, H.; Barceló, I.; Lana-Villarreal, T.; Gómez, R.; Bonn, M.; Cánovas, E. Interplay between Structure, Stoichiometry, and Electron Transfer Dynamics in SILAR-Based Quantum Dot-Sensitized Oxides. *Nano Lett.* **2014**, *14*, 5780–5786.
- (32) Guijarro, N.; Lana-Villarreal, T.; Lutz, T.; Haque, S. A.; Gómez, R. Sensitization of TiO<sub>2</sub> with PbSe Quantum Dots by SILAR: How Mercaptophenol Improves Charge Separation. *J. Phys. Chem. Lett.* **2012**, *3*, 3367–3372.
- (33) Lee, H.; Leventis, H. C.; Moon, S.-J.; Chen, P.; Ito, S.; Haque, S. A.; Torres, T.; Nüesch, F.; Geiger, T.; Zakeeruddin, S. M.; et al. PbS and CdS Quantum Dot-Sensitized Solid-State Solar Cells: “Old Concepts, New Results”. *Adv. Funct. Mater.* **2009**, *19*, 2735–2742.
- (34) Jara, D. H.; Yoon, S. J.; Stamplecoskie, K. G.; Kamat, P. V. Size-Dependent Photovoltaic Performance of CuInS<sub>2</sub> Quantum Dot-Sensitized Solar Cells. *Chem. Mater.* **2014**, *26*, 7221–7228.
- (35) Santra, P. K.; Kamat, P. V. Mn-Doped Quantum Dot Sensitized Solar Cells: A Strategy To Boost Efficiency over 5%. *J. Am. Chem. Soc.* **2012**, *134*, 2508–2511.
- (36) Bang, J. H.; Kamat, P. V. Quantum Dot Sensitized Solar Cells. A Tale of Two Semiconductor Nanocrystals: CdSe and CdTe. *ACS Nano* **2009**, *3*, 1467–1476.
- (37) Brus, L. Electronic Wave Functions in Semiconductor Clusters: Experiment and Theory. *J. Phys. Chem.* **1986**, *90*, 2555–2560.
- (38) Yu, W. W.; Qu, L.; Guo, W.; Peng, X. Experimental Determination of the Extinction Coefficient of CdTe, CdSe, and CdS Nanocrystals. *Chem. Mater.* **2003**, *15*, 2854–2860.
- (39) Moreels, I.; Justo, Y.; De Geyter, B.; Haustraete, K.; Martins, J. C.; Hens, Z. Size-Tunable, Bright, and Stable PbS Quantum Dots: A Surface Chemistry Study. *ACS Nano* **2011**, *5*, 2004–2012.
- (40) Moreels, I.; Lambert, K.; Smeets, D.; De Muynck, D.; Nollet, T.; Martins, J. C.; Vanhaecke, F.; Vantomme, A.; Delerue, C.; Allan, G.; et al. Size-Dependent Optical Properties of Colloidal PbS Quantum Dots. *ACS Nano* **2009**, *3*, 3023–3030.
- (41) Yang, C. C.; Li, S. Size, Dimensionality, and Constituent Stoichiometry Dependence of Bandgap Energies in Semiconductor Quantum Dots and Wires. *J. Phys. Chem. C* **2008**, *112*, 2851–2856.
- (42) Chuang, C.-H. M.; Brown, P. R.; Bulović, V.; Bawendi, M. G. Improved Performance and Stability in Quantum Dot Solar Cells through Band Alignment Engineering. *Nat. Mater.* **2014**, *13*, 796–801.
- (43) Hines, M. A.; Scholes, G. D. Colloidal PbS Nanocrystals with Size-Tunable Near-Infrared Emission: Observation of Post-Synthesis Self-Narrowing of the Particle Size Distribution. *Adv. Mater.* **2003**, *15*, 1844–1849.
- (44) Choi, H.; Ko, J.-H.; Kim, Y.-H.; Jeong, S. Steric-Hindrance-Driven Shape Transition in PbS Quantum Dots: Understanding Size-Dependent Stability. *J. Am. Chem. Soc.* **2013**, *135*, 5278–5281.
- (45) Cademartiri, L.; Bertolotti, J.; Sapienza, R.; Wiersma, D. S.; von Freymann, G.; Ozin, G. A. Multigram Scale, Solventless, and Diffusion-Controlled Route to Highly Monodisperse PbS Nanocrystals. *J. Phys. Chem. B* **2005**, *110*, 671–673.
- (46) Owen, J. S.; Chan, E. M.; Liu, H.; Alivisatos, A. P. Precursor Conversion Kinetics and the Nucleation of Cadmium Selenide Nanocrystals. *J. Am. Chem. Soc.* **2010**, *132*, 18206–18213.
- (47) Yuan, M.; Kemp, K. W.; Thon, S. M.; Kim, J. Y.; Chou, K. W.; Amassian, A.; Sargent, E. H. High-Performance Quantum-Dot Solids via Elemental Sulfur Synthesis. *Adv. Mater.* **2014**, *26*, 3513–3519.
- (48) Tang, J.; Brzozowski, L.; Barkhouse, D. A. R.; Wang, X.; Debnath, R.; Wolowiec, R.; Palmiano, E.; Levina, L.; Pattantyus-Abrraham, A. G.; Jamakosmanovic, D.; et al. Quantum Dot Photovoltaics in the Extreme Quantum Confinement Regime: The Surface-Chemical Origins of Exceptional Air- and Light-Stability. *ACS Nano* **2010**, *4*, 869–878.
- (49) Yu, H.; Li, J.; Loomis, R. A.; Wang, L.-W.; Buhro, W. E. Two-versus Three-Dimensional Quantum Confinement in Indium Phosphide Wires and Dots. *Nat. Mater.* **2003**, *2*, 517–520.
- (50) Cozzoli, P. D.; Pellegrino, T.; Manna, L. Synthesis, Properties and Perspectives of Hybrid Nanocrystal Structures. *Chem. Soc. Rev.* **2006**, *35*, 1195–1208.
- (51) Mullin, J. W. *Crystallization*; 4th ed.; Butterworth-Heinemann: Oxford, U.K., 2001.
- (52) Peng, X. Mechanisms for the Shape-Control and Shape-Evolution of Colloidal Semiconductor Nanocrystals. *Adv. Mater.* **2003**, *15*, 459–463.
- (53) Yu, J. H.; Joo, J.; Park, H. M.; Baik, S.-I.; Kim, Y. W.; Kim, S. C.; Heyon, T. Synthesis of Quantum-Sized Cubic ZnS Nanorods by the Oriented Attachment Mechanism. *J. Am. Chem. Soc.* **2005**, *127*, 5662–5670.

- (54) Cho, K.-S.; Talapin, D. V.; Gaschler, W.; Murray, C. B. Designing PbSe Nanowires and Nanorings through Oriented Attachment of Nanoparticles. *J. Am. Chem. Soc.* **2005**, *127*, 7140–7147.
- (55) Crisp, R. W.; Panthani, M. G.; Rance, W. L.; Duenow, J. N.; Parilla, P. A.; Callahan, R.; Dabney, M. S.; Berry, J. J.; Talapin, D. V.; Luther, J. M. Nanocrystal Grain Growth and Device Architectures for High-Efficiency CdTe Ink-Based Photovoltaics. *ACS Nano* **2014**, *8*, 9063–9072.
- (56) Kovalenko, M. V.; Scheele, M.; Talapin, D. V. Colloidal Nanocrystals with Molecular Metal Chalcogenide Surface Ligands. *Science* **2009**, *324*, 1417–1420.
- (57) Klem, E. J. D.; MacNeil, D. D.; Cyr, P. W.; Levina, L.; Sargent, E. H. Efficient Solution-Processed Infrared Photovoltaic Cells: Planarized All-Inorganic Bulk Heterojunction Devices via Inter-Quantum-Dot Bridging during Growth from Solution. *Appl. Phys. Lett.* **2007**, *90*, 183113.
- (58) Diedenhofen, S. L.; Kufer, D.; Lasanta, T.; Konstantatos, G. Integrated Colloidal Quantum Dot Photodetectors with Color-Tunable Plasmonic Nanofocusing Lenses. *Light Sci. Appl.* **2015**, *4*, e234.
- (59) Huynh, W. U.; Dittmer, J. J.; Alivisatos, A. P. Hybrid Nanorod-Polymer Solar Cells. *Science* **2002**, *295*, 2425–2427.
- (60) Li, Q.; Sun, B.; Kinloch, I. A.; Zhi, D.; Sirringhaus, H.; Windle, A. H. Enhanced Self-Assembly of Pyridine-Capped CdSe Nanocrystals on Individual Single-Walled Carbon Nanotubes. *Chem. Mater.* **2006**, *18*, 164–168.
- (61) Zhang, C.; O'Brien, S.; Balogh, L. Comparison and Stability of CdSe Nanocrystals Covered with Amphiphilic Poly(amidoamine) Dendrimers. *J. Phys. Chem. B* **2002**, *106*, 10316–10321.
- (62) Lokteva, I.; Radychev, N.; Witt, F.; Borchert, H.; Parisi, J.; Kolny-Olesiak, J. Surface Treatment of CdSe Nanoparticles for Application in Hybrid Solar Cells: The Effect of Multiple Ligand Exchange with Pyridine. *J. Phys. Chem. C* **2010**, *114*, 12784–12791.
- (63) Jang, J.; Liu, W.; Son, J. S.; Talapin, D. V. Temperature-Dependent Hall and Field-Effect Mobility in Strongly Coupled All-Inorganic Nanocrystal Arrays. *Nano Lett.* **2014**, *14*, 653–662.
- (64) Lee, J.-S.; Kovalenko, M. V.; Huang, J.; Chung, D. S.; Talapin, D. V. Band-like Transport, High Electron Mobility and High Photoconductivity in All-Inorganic Nanocrystal Arrays. *Nat. Nanotechnol.* **2011**, *6*, 348–352.
- (65) Liu, W.; Lee, J.-S.; Talapin, D. V. III–V Nanocrystals Capped with Molecular Metal Chalcogenide Ligands: High Electron Mobility and Ambipolar Photoresponse. *J. Am. Chem. Soc.* **2012**, *135*, 1349–1357.
- (66) Kovalenko, M. V.; Schaller, R. D.; Jarzab, D.; Loi, M. A.; Talapin, D. V. Inorganically Functionalized PbS–CdS Colloidal Nanocrystals: Integration into Amorphous Chalcogenide Glass and Luminescent Properties. *J. Am. Chem. Soc.* **2012**, *134*, 2457–2460.
- (67) Jiang, C.; Lee, J.-S.; Talapin, D. V. Soluble Precursors for CuInSe<sub>2</sub>, CuIn<sub>1-x</sub>Ga<sub>x</sub>Se<sub>2</sub>, and Cu<sub>2</sub>ZnSn(S,Se)<sub>4</sub> Based on Colloidal Nanocrystals and Molecular Metal Chalcogenide Surface Ligands. *J. Am. Chem. Soc.* **2012**, *134*, 5010–5013.
- (68) Tang, J.; Kemp, K. W.; Hoogland, S.; Jeong, K. S.; Liu, H.; Levina, L.; Furukawa, M.; Wang, X.; Debnath, R.; Cha, D.; et al. Colloidal-Quantum-Dot Photovoltaics Using Atomic-Ligand Passivation. *Nat. Mater.* **2011**, *10*, 765–771.
- (69) Anderson, N. C.; Owen, J. S. Soluble, Chloride-Terminated CdSe Nanocrystals: Ligand Exchange Monitored by <sup>1</sup>H and <sup>31</sup>P NMR Spectroscopy. *Chem. Mater.* **2012**, *25*, 69–76.
- (70) Greaney, M. J.; Couderc, E.; Zhao, J.; Nail, B. A.; Mecklenburg, M.; Thornbury, W.; Osterloh, F. E.; Bradford, S. E.; Brutcher, R. L. Controlling the Trap State Landscape of Colloidal CdSe Nanocrystals with Cadmium Halide Ligands. *Chem. Mater.* **2015**, *27*, 744–756.
- (71) Ning, Z.; Ren, Y.; Hoogland, S.; Voznyy, O.; Levina, L.; Stadler, P.; Lan, X.; Zhitomirsky, D.; Sargent, E. H. All-Inorganic Colloidal Quantum Dot Photovoltaics Employing Solution-Phase Halide Passivation. *Adv. Mater.* **2012**, *24*, 6295–6299.
- (72) Zhang, J.; Gao, J.; Miller, E. M.; Luther, J. M.; Beard, M. C. Diffusion-Controlled Synthesis of PbS and PbSe Quantum Dots with in Situ Halide Passivation for Quantum Dot Solar Cells. *ACS Nano* **2013**, *8*, 614–622.
- (73) Dirin, D. N.; Dreyfuss, S.; Bodnarchuk, M. I.; Nedelcu, G.; Papagiorgis, P.; Itskos, G.; Kovalenko, M. V. Lead Halide Perovskites and Other Metal Halide Complexes as Inorganic Capping Ligands for Colloidal Nanocrystals. *J. Am. Chem. Soc.* **2014**, *136*, 6550–6553.
- (74) Zhang, H.; Jang, J.; Liu, W.; Talapin, D. V. Colloidal Nanocrystals with Inorganic Halide, Pseudohalide, and Halometallate Ligands. *ACS Nano* **2014**, *8*, 7359–7369.
- (75) Smith, D. K.; Luther, J. M.; Semonin, O. E.; Nozik, A. J.; Beard, M. C. Tuning the Synthesis of Ternary Lead Chalcogenide Quantum Dots by Balancing Precursor Reactivity. *ACS Nano* **2010**, *5*, 183–190.
- (76) Van Vechten, J. A.; Bergstresser, T. K. Electronic Structures of Semiconductor Alloys. *Phys. Rev. B* **1970**, *1*, 3351–3358.
- (77) Regulacio, M. D.; Han, M.-Y. Composition-Tunable Alloyed Semiconductor Nanocrystals. *Acc. Chem. Res.* **2010**, *43*, 621–630.
- (78) Mukherjee, S.; Hazarika, A.; Santra, P. K.; Abdelhady, A. L.; Malik, M. A.; Gorgoi, M.; O'Brien, P.; Karis, O.; Sarma, D. D. Determination of Internal Structures of Heterogeneous Nanocrystals Using Variable-Energy Photoemission Spectroscopy. *J. Phys. Chem. C* **2014**, *118*, 15534–15540.
- (79) Buonsanti, R.; Milliron, D. J. Chemistry of Doped Colloidal Nanocrystals. *Chem. Mater.* **2013**, *25*, 1305–1317.
- (80) Shu, T.; Zhou, Z.; Wang, H.; Liu, G.; Xiang, P.; Rong, Y.; Han, H.; Zhao, Y. Efficient Quantum Dot-Sensitized Solar Cell with Tunable Energy Band CdSe<sub>x</sub>S<sub>(1-x)</sub> Quantum Dots. *J. Mater. Chem.* **2012**, *22*, 10525–10529.
- (81) Pan, Z.; Zhao, K.; Wang, J.; Zhang, H.; Feng, Y.; Zhong, X. Near Infrared Absorption of CdSe<sub>x</sub>Te<sub>1-x</sub> Alloyed Quantum Dot Sensitized Solar Cells with More than 6% Efficiency and High Stability. *ACS Nano* **2013**, *7*, 5215–5222.
- (82) Stavrinidis, A.; Rath, A. K.; de Arquer, F. P. G.; Diedenhofen, S. L.; Magén, C.; Martinez, L.; So, D.; Konstantatos, G. Heterovalent Cation Substitutional Doping for Quantum Dot Homojunction Solar Cells. *Nat. Commun.* **2013**, *4*.
- (83) Liu, H.; Zhitomirsky, D.; Hoogland, S.; Tang, J.; Kramer, I. J.; Ning, Z.; Sargent, E. H. Systematic Optimization of Quantum Junction Colloidal Quantum Dot Solar Cells. *Appl. Phys. Lett.* **2012**, *101*, 151112.
- (84) Deutsch, Z.; Avidan, A.; Pinkas, I.; Oron, D. Energetics and Dynamics of Exciton–Exciton Interactions in Compound Colloidal Semiconductor Quantum Dots. *Phys. Chem. Chem. Phys.* **2011**, *13*, 3210–3219.
- (85) Reiss, P.; Protière, M.; Li, L. Core/Shell Semiconductor Nanocrystals. *Small* **2009**, *5*, 154–168.
- (86) Justo, Y.; Geiregat, P.; Hoecke, K. V.; Vanhaecke, F.; De Mello Donega, C.; Hens, Z. Optical Properties of PbS/CdS Core/Shell Quantum Dots. *J. Phys. Chem. C* **2013**, *117*, 20171–20177.
- (87) Zhao, H.; Fan, Z.; Liang, H.; Selopal, G. S.; Gonfa, B. A.; Jin, L.; Soudi, A.; Cui, D.; Enrichi, F.; Natile, M. M.; et al. Controlling Photoinduced Electron Transfer from PbS@CdS Core@shell Quantum Dots to Metal Oxide Nanostructured Thin Films. *Nanoscale* **2014**, *6*, 7004–7011.
- (88) Neo, D. C. J.; Cheng, C.; Stranks, S. D.; Fairclough, S. M.; Kim, J. S.; Kirkland, A. I.; Smith, J. M.; Snaith, H. J.; Aspasia, H. E.; Watt, A. A. R. Influence of Shell Thickness and Surface Passivation on PbS/CdS Core/Shell Colloidal Quantum Dot Solar Cells. *Chem. Mater.* **2014**, *26*, 4004–4013.
- (89) Neo, M. S.; Venkatram, N.; Li, G. S.; Chin, W. S.; Ji, W. Synthesis of PbS/CdS Core–Shell QDs and Their Nonlinear Optical Properties. *J. Phys. Chem. C* **2010**, *114*, 18037–18044.
- (90) Pan, Z.; Mora-Seró, I.; Shen, Q.; Zhang, H.; Li, Y.; Zhao, K.; Wang, J.; Zhong, X.; Bisquert, J. High-Efficiency “Green” Quantum Dot Solar Cells. *J. Am. Chem. Soc.* **2014**, *136*, 9203–9210.
- (91) Aldakov, D.; Lefrançois, A.; Reiss, P. Ternary and Quaternary Metal Chalcogenide Nanocrystals: Synthesis, Properties and Applications. *J. Mater. Chem. C* **2013**, *1*, 3756–3776.
- (92) Santra, P. K.; Nair, P. V.; George Thomas, K.; Kamat, P. V. CuInS<sub>2</sub>-Sensitized Quantum Dot Solar Cell. Electrophoretic Deposi-

- tion, Excited-State Dynamics, and Photovoltaic Performance. *J. Phys. Chem. Lett.* **2013**, *4*, 722–729.
- (93) Li, T.-L.; Lee, Y.-L.; Teng, H. High-Performance Quantum Dot-Sensitized Solar Cells Based on Sensitization with CuInS<sub>2</sub> Quantum Dots/CdS Heterostructure. *Energy Environ. Sci.* **2012**, *5*, 5315–5324.
- (94) Luo, J.; Wei, H.; Huang, Q.; Hu, X.; Zhao, H.; Yu, R.; Li, D.; Luo, Y.; Meng, Q. Highly Efficient Core–Shell CuInS<sub>2</sub>–Mn Doped CdS Quantum Dot Sensitized Solar Cells. *Chem. Commun.* **2013**, *49*, 3881–3883.
- (95) McDaniel, H.; Fuke, N.; Pietryga, J. M.; Klimov, V. I. Engineered CuInSe<sub>x</sub>S<sub>2-x</sub> Quantum Dots for Sensitized Solar Cells. *J. Phys. Chem. Lett.* **2013**, *4*, 355–361.
- (96) McDaniel, H.; Fuke, N.; Makarov, N. S.; Pietryga, J. M.; Klimov, V. I. An Integrated Approach to Realizing High-Performance Liquid-Junction Quantum Dot Sensitized Solar Cells. *Nat. Commun.* **2013**, *4*.
- (97) Ivanov, S. A.; Piryatinski, A.; Nanda, J.; Tretiak, S.; Zavadil, K. R.; Wallace, W. O.; Werder, D.; Klimov, V. I. Type-II Core/Shell CdS/ZnSe Nanocrystals: Synthesis, Electronic Structures, and Spectroscopic Properties. *J. Am. Chem. Soc.* **2007**, *129*, 11708–11719.
- (98) Ning, Z.; Tian, H.; Yuan, C.; Fu, Y.; Qin, H.; Sun, L.; Ågren, H. Solar Cells Sensitized with Type-II ZnSe–CdS Core/shell Colloidal Quantum Dots. *Chem. Commun.* **2011**, *47*, 1536–1538.
- (99) Ning, Z.; Yuan, C.; Tian, H.; Fu, Y.; Li, L.; Sun, L.; Ågren, H. Type-II Colloidal Quantum Dot Sensitized Solar Cells with a Thiourea Based Organic Redox Couple. *J. Mater. Chem.* **2012**, *22*, 6032–6037.
- (100) Zhang, Q.; Chen, G.; Yang, Y.; Shen, X.; Zhang, Y.; Li, C.; Yu, R.; Luo, Y.; Li, D.; Meng, Q. Toward Highly Efficient CdS/CdSe Quantum Dots-Sensitized Solar Cells Incorporating Ordered Photoanodes on Transparent Conductive Substrates. *Phys. Chem. Chem. Phys.* **2012**, *14*, 6479–6486.
- (101) Tian, J.; Zhang, Q.; Zhang, L.; Gao, R.; Shen, L.; Zhang, S.; Qu, X.; Cao, G. ZnO/TiO<sub>2</sub> Nanocable Structured Photoelectrodes for CdS/CdSe Quantum Dot Co-Sensitized Solar Cells. *Nanoscale* **2013**, *5*, 936–943.
- (102) Pan, Z.; Zhang, H.; Cheng, K.; Hou, Y.; Hua, J.; Zhong, X. Highly Efficient Inverted Type-I CdS/CdSe Core/Shell Structure QD-Sensitized Solar Cells. *ACS Nano* **2012**, *6*, 3982–3991.
- (103) Sheng, P.; Li, W.; Cai, J.; Wang, X.; Tong, X.; Cai, Q.; Grimes, C. A. A Novel Method for the Preparation of a Photocorrosion Stable Core/Shell CdTe/CdS Quantum Dot TiO<sub>2</sub> Nanotube Array Photoelectrode Demonstrating an AM 1.5G Photoconversion Efficiency of 6.12%. *J. Mater. Chem. A* **2013**, *1*, 7806–7815.
- (104) Wang, J.; Mora-Seró, I.; Pan, Z.; Zhao, K.; Zhang, H.; Feng, Y.; Yang, G.; Zhong, X.; Bisquert, J. Core/Shell Colloidal Quantum Dot Exciplex States for the Development of Highly Efficient Quantum-Dot-Sensitized Solar Cells. *J. Am. Chem. Soc.* **2013**, *135*, 15913–15922.
- (105) McElroy, N.; Page, R. C.; Espinbarro-Valazquez, D.; Lewis, E.; Haigh, S.; O’Brien, P.; Binks, D. J. Comparison of Solar Cells Sensitised by CdTe/CdSe and CdSe/CdTe Core/Shell Colloidal Quantum Dots with and without a CdS Outer Layer. *Thin Solid Films* **2014**, *560*, 65–70.
- (106) Maenosono, S.; Okubo, T.; Yamaguchi, Y. Overview of Nanoparticle Array Formation by Wet Coating. *J. Nanopart. Res.* **2003**, *5*, 5–15.
- (107) Fischer, A.; Rollny, L.; Pan, J.; Carey, G. H.; Thon, S. M.; Hoogland, S.; Voznyy, O.; Zhitomirsky, D.; Kim, J. Y.; Bakr, O. M.; et al. Directly Deposited Quantum Dot Solids Using a Colloidally Stable Nanoparticle Ink. *Adv. Mater.* **2013**, *25*, 5742–5749.
- (108) Ning, Z.; Dong, H.; Zhang, Q.; Voznyy, O.; Sargent, E. H. Solar Cells Based on Inks of n-Type Colloidal Quantum Dots. *ACS Nano* **2014**, *8*, 10321–10327.
- (109) Achermann, M.; Petruska, M. A.; Crooker, S. A.; Klimov, V. I. Picosecond Energy Transfer in Quantum Dot Langmuir–Blodgett Nanoassemblies. *J. Phys. Chem. B* **2003**, *107*, 13782–13787.
- (110) Shimomura, M.; Sawadaishi, T. Bottom-Up Strategy of Materials Fabrication: A New Trend in Nanotechnology of Soft Materials. *Curr. Opin. Colloid Interface Sci.* **2001**, *6*, 11–16.
- (111) Fu, Y.; Xu, H.; Bai, S.; Qiu, D.; Sun, J.; Wang, Z.; Zhang, X. Fabrication of a Stable Polyelectrolyte/Au Nanoparticles Multilayer Film. *Macromol. Rapid Commun.* **2002**, *23*, 256–259.
- (112) Cassagneau, T.; Mallouk, T. E.; Fendler, J. H. Layer-by-Layer Assembly of Thin Film Zener Diodes from Conducting Polymers and CdSe Nanoparticles. *J. Am. Chem. Soc.* **1998**, *120*, 7848–7859.
- (113) Kirmani, A. R.; Carey, G. H.; Abdelsamie, M.; Yan, B.; Cha, D.; Rollny, L. R.; Cui, X.; Sargent, E. H.; Amassian, A. Effect of Solvent Environment on Colloidal-Quantum-Dot Solar-Cell Manufacturability and Performance. *Adv. Mater.* **2014**, *26*, 4717–4723.
- (114) Yang, C.-C.; Y. Josefowicz, J.; Alexandru, L. Deposition of Ultrathin Films by a Withdrawal Method. *Thin Solid Films* **1980**, *74*, 117–127.
- (115) Guo, Q.; Kim, S. J.; Kar, M.; Shafarman, W. N.; Birkmire, R. W.; Stach, E. A.; Agrawal, R.; Hillhouse, H. W. Development of CuInSe<sub>2</sub> Nanocrystal and Nanoring Inks for Low-Cost Solar Cells. *Nano Lett.* **2008**, *8*, 2982–2987.
- (116) Wood, V.; Panzer, M. J.; Chen, J.; Bradley, M. S.; Halpert, J. E.; Bawendi, M. G.; Bulović, V. Inkjet-Printed Quantum Dot–Polymer Composites for Full-Color AC-Driven Displays. *Adv. Mater.* **2009**, *21*, 2151–2155.
- (117) Kramer, I. J.; Minor, J. C.; Moreno-Bautista, G.; Rollny, L.; Kanjanaboons, P.; Kopilovic, D.; Thon, S. M.; Carey, G. H.; Chou, K. W.; Zhitomirsky, D.; et al. Efficient Spray-Coated Colloidal Quantum Dot Solar Cells. *Adv. Mater.* **2015**, *27*, 116–121.
- (118) Kramer, I. J.; Moreno-Bautista, G.; Minor, J. C.; Kopilovic, D.; Sargent, E. H. Colloidal Quantum Dot Solar Cells on Curved and Flexible Substrates. *Appl. Phys. Lett.* **2014**, *105*, 163902.
- (119) Remacle, F. On Electronic Properties of Assemblies of Quantum Nanodots. *J. Phys. Chem. A* **2000**, *104*, 4739–4747.
- (120) Liu, Y.; Gibbs, M.; Puthussery, J.; Gaik, S.; Ihly, R.; Hillhouse, H. W.; Law, M. Dependence of Carrier Mobility on Nanocrystal Size and Ligand Length in PbSe Nanocrystal Solids. *Nano Lett.* **2010**, *10*, 1960–1969.
- (121) Talgorn, E.; Moysidou, E.; Abellon, R. D.; Savenije, T. J.; Goossens, A.; Houtepen, A. J.; Siebbeles, L. D. A. Highly Photoconductive CdSe Quantum-Dot Films: Influence of Capping Molecules and Film Preparation Procedure. *J. Phys. Chem. C* **2010**, *114*, 3441–3447.
- (122) Sun, L.; Choi, J. J.; Stachnik, D.; Bartnik, A. C.; Hyun, B.-R.; Malliaras, G. G.; Hanrath, T.; Wise, F. W. Bright Infrared Quantum-Dot Light-Emitting Diodes through Inter-Dot Spacing Control. *Nat. Nanotechnol.* **2012**, *7*, 369–373.
- (123) Ip, A. H.; Thon, S. M.; Hoogland, S.; Voznyy, O.; Zhitomirsky, D.; Debnath, R.; Levina, L.; Rollny, L. R.; Carey, G. H.; Fischer, A.; et al. Hybrid Passivated Colloidal Quantum Dot Solids. *Nat. Nanotechnol.* **2012**, *7*, 577–582.
- (124) Zarghami, M. H.; Liu, Y.; Gibbs, M.; Gebremichael, E.; Webster, C.; Law, M. p-Type PbSe and PbS Quantum Dot Solids Prepared with Short-Chain Acids and Diacids. *ACS Nano* **2010**, *4*, 2475–2485.
- (125) Smith, A. R.; Yoon, W.; Heuer, W. B.; Baril, S. I. M.; Boercker, J. E.; Tischler, J. G.; Foos, E. E. Effect of Ligand Structure on the Optical and Electronic Properties of Nanocrystalline PbSe Films. *J. Phys. Chem. C* **2012**, *116*, 6031–6037.
- (126) Baumgardner, W. J.; Whitham, K.; Hanrath, T. Confined-but-Connected Quantum Solids via Controlled Ligand Displacement. *Nano Lett.* **2013**, *13*, 3225–3231.
- (127) Sandeep, C. S. S.; Azpiroz, J. M.; Evers, W. H.; Boehme, S. C.; Moreels, I.; Kinge, S.; Siebbeles, L. D. A.; Infante, I.; Houtepen, A. J. Epitaxially Connected PbSe Quantum-Dot Films: Controlled Neck Formation and Optoelectronic Properties. *ACS Nano* **2014**, *8*, 11499–11511.
- (128) Ning, Z.; Voznyy, O.; Pan, J.; Hoogland, S.; Adinolfi, V.; Xu, J.; Li, M.; Kirmani, A. R.; Sun, J.-P.; Minor, J.; et al. Air-Stable n-Type Colloidal Quantum Dot Solids. *Nat. Mater.* **2014**, *13*, 822–828.
- (129) Zhang, J.; Gao, J.; Church, C. P.; Miller, E. M.; Luther, J. M.; Klimov, V. I.; Beard, M. C. PbSe Quantum Dot Solar Cells with More

- Than 6% Efficiency Fabricated in Ambient Atmosphere. *Nano Lett.* **2014**, *14*, 6010–6015.
- (130) Carey, G. H.; Levina, L.; Comin, R.; Voznyy, O.; Sargent, E. H. Record Charge Carrier Diffusion Length in Colloidal Quantum Dot Solids via Mutual Dot-to-Dot Surface Passivation. *Adv. Mater.* **2015**, *27*, 3325–3330.
- (131) Turo, M. J.; Macdonald, J. E. Crystal-Bound vs Surface-Bound Thiols on Nanocrystals. *ACS Nano* **2014**, *8*, 10205–10213.
- (132) Anderson, N. C.; Hendricks, M. P.; Choi, J. J.; Owen, J. S. Ligand Exchange and the Stoichiometry of Metal Chalcogenide Nanocrystals: Spectroscopic Observation of Facile Metal-Carboxylate Displacement and Binding. *J. Am. Chem. Soc.* **2013**, *135*, 18536–18548.
- (133) Zhitomirsky, D.; Furukawa, M.; Tang, J.; Stadler, P.; Hoogland, S.; Voznyy, O.; Liu, H.; Sargent, E. H. N-Type Colloidal-Quantum-Dot Solids for Photovoltaics. *Adv. Mater.* **2012**, *24*, 6181–6185.
- (134) Milliron, D. J. Quantum Dot Solar Cells: The Surface Plays a Core Role. *Nat. Mater.* **2014**, *13*, 772–773.
- (135) Brown, P. R.; Kim, D.; Lunt, R. R.; Zhao, N.; Bawendi, M. G.; Grossman, J. C.; Bulović, V. Energy Level Modification in Lead Sulfide Quantum Dot Thin Films through Ligand Exchange. *ACS Nano* **2014**, *8*, 5863–5872.
- (136) Katsiev, K.; Ip, A. H.; Fischer, A.; Tanabe, I.; Zhang, X.; Kirmani, A. R.; Voznyy, O.; Rollny, L. R.; Chou, K. W.; Thon, S. M.; et al. The Complete In-Gap Electronic Structure of Colloidal Quantum Dot Solids and Its Correlation with Electronic Transport and Photovoltaic Performance. *Adv. Mater.* **2014**, *26*, 937–942.
- (137) Ding, B.; Wang, Y.; Huang, P.-S.; Waldeck, D. H.; Lee, J.-K. Depleted Bulk Heterojunctions in Thermally Annealed PbS Quantum Dot Solar Cells. *J. Phys. Chem. C* **2014**, *118*, 14749–14758.
- (138) Jo, C. H.; Kim, J. H.; Kim, J.; Kim, J.; Oh, M. S.; Kang, M. S.; Kim, M.-G.; Kim, Y.-H.; Ju, B.-K.; Park, S. K. Low-Temperature Annealed PbS Quantum Dot Films for Scalable and Flexible Ambipolar Thin-Film-Transistors and Circuits. *J. Mater. Chem. C* **2014**, *2*, 10305–10311.
- (139) Klem, E. J. D.; Shukla, H.; Hinds, S.; MacNeil, D. D.; Levina, L.; Sargent, E. H. Impact of Dithiol Treatment and Air Annealing on the Conductivity, Mobility, and Hole Density in PbS Colloidal Quantum Dot Solids. *Appl. Phys. Lett.* **2008**, *92*, 212105.
- (140) Goodwin, E. D.; Diroll, B. T.; Oh, S. J.; Paik, T.; Murray, C. B.; Kagan, C. R. Effects of Post-Synthesis Processing on CdSe Nanocrystals and Their Solids: Correlation between Surface Chemistry and Optoelectronic Properties. *J. Phys. Chem. C* **2014**, *118*, 27097–27105.
- (141) Koole, R.; Schapotschnikow, P.; de Mello Donegá, C.; Vlugt, T. J. H.; Meijerink, A. Time-Dependent Photoluminescence Spectroscopy as a Tool To Measure the Ligand Exchange Kinetics on a Quantum Dot Surface. *ACS Nano* **2008**, *2*, 1703–1714.
- (142) Carey, G. H.; Kramer, I. J.; Kanjanaboops, P.; Moreno-Bautista, G.; Voznyy, O.; Rollny, L.; Tang, J. A.; Hoogland, S.; Sargent, E. H. Electronically Active Impurities in Colloidal Quantum Dot Solids. *ACS Nano* **2014**, *8*, 11763–11769.
- (143) Zhitomirsky, D.; Kramer, I. J.; Labelle, A. J.; Fischer, A.; Debnath, R.; Pan, J.; Bakr, O. M.; Sargent, E. H. Colloidal Quantum Dot Photovoltaics: The Effect of Polydispersity. *Nano Lett.* **2012**, *12*, 1007–1012.
- (144) Johnston, K. W.; Pattantyus-Abraham, A. G.; Clifford, J. P.; Myrskog, S. H.; Hoogland, S.; Shukla, H.; Klem, E. J. D.; Levina, L.; Sargent, E. H. Efficient Schottky-Quantum-Dot Photovoltaics: The Roles of Depletion, Drift, and Diffusion. *Appl. Phys. Lett.* **2008**, *92*, 122111.
- (145) Stadler, P.; Sutherland, B. R.; Ren, Y.; Ning, Z.; Simchi, A.; Thon, S. M.; Hoogland, S.; Sargent, E. H. Joint Mapping of Mobility and Trap Density in Colloidal Quantum Dot Solids. *ACS Nano* **2013**, *7*, 5757–5762.
- (146) Oh, S. J.; Berry, N. E.; Choi, J.-H.; Gaulding, E. A.; Paik, T.; Hong, S.-H.; Murray, C. B.; Kagan, C. R. Stoichiometric Control of Lead Chalcogenide Nanocrystal Solids To Enhance Their Electronic and Optoelectronic Device Performance. *ACS Nano* **2013**, *7*, 2413–2421.
- (147) Bozyigit, D.; Jakob, M.; Yarema, O.; Wood, V. Deep Level Transient Spectroscopy (DLTS) on Colloidal-Synthesized Nanocrystal Solids. *ACS Appl. Mater. Interfaces* **2013**, *5*, 2915–2919.
- (148) Bozyigit, D.; Volk, S.; Yarema, O.; Wood, V. Quantification of Deep Traps in Nanocrystal Solids, Their Electronic Properties, and Their Influence on Device Behavior. *Nano Lett.* **2013**, *13*, 5284–5288.
- (149) Kimball, G. M.; Müller, A. M.; Lewis, N. S.; Atwater, H. A. Photoluminescence-Based Measurements of the Energy Gap and Diffusion Length of  $Zn_3P_2$ . *Appl. Phys. Lett.* **2009**, *95*, 112103.
- (150) Leite, M. S.; Woo, R. L.; Hong, W. D.; Law, D. C.; Atwater, H. A. Wide-Band-Gap InAlAs Solar Cell for an Alternative Multijunction Approach. *Appl. Phys. Lett.* **2011**, *98*, 093502.
- (151) Miller, O. D.; Yablonovitch, E.; Kurtz, S. R. Strong Internal and External Luminescence as Solar Cells Approach the Shockley–Queisser Limit. *IEEE J. Photovoltaics* **2012**, *2*, 303–311.
- (152) Zhitomirsky, D.; Voznyy, O.; Hoogland, S.; Sargent, E. H. Measuring Charge Carrier Diffusion in Coupled Colloidal Quantum Dot Solids. *ACS Nano* **2013**, *7*, 5282–5290.
- (153) Zhitomirsky, D.; Voznyy, O.; Levina, L.; Hoogland, S.; Kemp, K. W.; Ip, A. H.; Thon, S. M.; Sargent, E. H. Engineering Colloidal Quantum Dot Solids within and beyond the Mobility-Invariant Regime. *Nat. Commun.* **2014**, *5*.
- (154) Tang, J.; Liu, H.; Zhitomirsky, D.; Hoogland, S.; Wang, X.; Furukawa, M.; Levina, L.; Sargent, E. H. Quantum Junction Solar Cells. *Nano Lett.* **2012**, *12*, 4889–4894.
- (155) Voznyy, O.; Zhitomirsky, D.; Stadler, P.; Ning, Z.; Hoogland, S.; Sargent, E. H. A Charge-Orbital Balance Picture of Doping in Colloidal Quantum Dot Solids. *ACS Nano* **2012**, *6*, 8448–8455.
- (156) Jeong, K. S.; Deng, Z.; Keuleyan, S.; Liu, H.; Guyot-Sionnest, P. Air-Stable N-Doped Colloidal HgS Quantum Dots. *J. Phys. Chem. Lett.* **2014**, *5*, 1139–1143.
- (157) Yaacobi-Gross, N.; Garphunkin, N.; Solomeshch, O.; Vaneski, A.; Susha, A. S.; Rogach, A. L.; Tessler, N. Combining Ligand-Induced Quantum-Confining Stark Effect with Type II Heterojunction Bilayer Structure in CdTe and CdSe Nanocrystal-Based Solar Cells. *ACS Nano* **2012**, *6*, 3128–3133.
- (158) Yaacobi-Gross, N.; Soreni-Harari, M.; Zimin, M.; Kababya, S.; Schmidt, A.; Tessler, N. Molecular Control of Quantum-Dot Internal Electric Field and Its Application to CdSe-Based Solar Cells. *Nat. Mater.* **2011**, *10*, 974–979.
- (159) McDonald, S. A.; Konstantatos, G.; Zhang, S.; Cyr, P. W.; Klem, E. J. D.; Levina, L.; Sargent, E. H. Solution-Processed PbS Quantum Dot Infrared Photodetectors and Photovoltaics. *Nat. Mater.* **2005**, *4*, 138–142.
- (160) Maria, A.; Cyr, P. W.; Klem, E. J. D.; Levina, L.; Sargent, E. H. Solution-Processed Infrared Photovoltaic Devices with >10% Monochromatic Internal Quantum Efficiency. *Appl. Phys. Lett.* **2005**, *87*, 213112.
- (161) Clifford, J. P.; Johnston, K. W.; Levina, L.; Sargent, E. H. Schottky Barriers to Colloidal Quantum Dot Films. *Appl. Phys. Lett.* **2007**, *91*, 253117.
- (162) Luther, J. M.; Law, M.; Beard, M. C.; Song, Q.; Reese, M. O.; Ellingson, R. J.; Nozik, A. J. Schottky Solar Cells Based on Colloidal Nanocrystal Films. *Nano Lett.* **2008**, *8*, 3488–3492.
- (163) Koleilat, G. I.; Levina, L.; Shukla, H.; Myrskog, S. H.; Hinds, S.; Pattantyus-Abraham, A. G.; Sargent, E. H. Efficient, Stable Infrared Photovoltaics Based on Solution-Cast Colloidal Quantum Dots. *ACS Nano* **2008**, *2*, 833–840.
- (164) Tang, J.; Wang, X.; Brzozowski, L.; Barkhouse, D. A. R.; Debnath, R.; Levina, L.; Sargent, E. H. Schottky Quantum Dot Solar Cells Stable in Air under Solar Illumination. *Adv. Mater.* **2010**, *22*, 1398–1402.
- (165) Choi, M.-J.; Oh, J.; Yoo, J.-K.; Choi, J.; Sim, D. M.; Jung, Y. S. Tailoring of the PbS/Metal Interface in Colloidal Quantum Dot Solar Cells for Improvements of Performance and Air Stability. *Energy Environ. Sci.* **2014**, *7*, 3052–3060.

- (166) Zhao, N.; Osedach, T. P.; Chang, L.-Y.; Geyer, S. M.; Wanger, D.; Binda, M. T.; Arango, A. C.; Bawendi, M. G.; Bulovic, V. Colloidal PbS Quantum Dot Solar Cells with High Fill Factor. *ACS Nano* **2010**, *4*, 3743–3752.
- (167) Johnston, K. W.; Pattantyus-Abraham, A. G.; Clifford, J. P.; Myrskog, S. H.; MacNeil, D. D.; Levina, L.; Sargent, E. H. Schottky-Quantum Dot Photovoltaics for Efficient Infrared Power Conversion. *Appl. Phys. Lett.* **2008**, *92*, 151115.
- (168) Piliego, C.; Protesescu, L.; Bisri, S. Z.; Kovalenko, M. V.; Loi, M. A. 5.2% Efficient PbS Nanocrystal Schottky Solar Cells. *Energy Environ. Sci.* **2013**, *6*, 3054–3059.
- (169) Henry, C. H. Limiting Efficiencies of Ideal Single and Multiple Energy Gap Terrestrial Solar Cells. *J. Appl. Phys.* **1980**, *51*, 4494.
- (170) Pattantyus-Abraham, A. G.; Kramer, I. J.; Barkhouse, A. R.; Wang, X.; Konstantatos, G.; Debnath, R.; Levina, L.; Raabe, I.; Nazeeruddin, M. K.; Grätzel, M.; et al. Depleted-Heterojunction Colloidal Quantum Dot Solar Cells. *ACS Nano* **2010**, *4*, 3374–3380.
- (171) Choi, J. J.; Lim, Y.-F.; Santiago-Berrios, M. B.; Oh, M.; Hyun, B.-R.; Sun, L.; Bartnik, A. C.; Goedhart, A.; Malliaras, G. G.; Abrúñ, H. D.; et al. PbSe Nanocrystal Excitonic Solar Cells. *Nano Lett.* **2009**, *9*, 3749–3755.
- (172) Willis, S. M.; Cheng, C.; Assender, H. E.; Watt, A. A. R. The Transitional Heterojunction Behavior of PbS/ZnO Colloidal Quantum Dot Solar Cells. *Nano Lett.* **2012**, *12*, 1522–1526.
- (173) Luther, J. M.; Gao, J.; Lloyd, M. T.; Semonin, O. E.; Beard, M. C.; Nozik, A. J. Stability Assessment on a 3% Bilayer PbS/ZnO Quantum Dot Heterojunction Solar Cell. *Adv. Mater.* **2010**, *22*, 3704–3707.
- (174) Gao, J.; Luther, J. M.; Semonin, O. E.; Ellingson, R. J.; Nozik, A. J.; Beard, M. C. Quantum Dot Size Dependent  $J-V$  Characteristics in Heterojunction ZnO/PbS Quantum Dot Solar Cells. *Nano Lett.* **2011**, *11*, 1002–1008.
- (175) Chang, L.-Y.; Lunt, R. R.; Brown, P. R.; Bulović, V.; Bawendi, M. G. Low-Temperature Solution-Processed Solar Cells Based on PbS Colloidal Quantum Dot/CdS Heterojunctions. *Nano Lett.* **2013**, *13*, 994–999.
- (176) Shaheen, S. E.; Brabec, C. J.; Sariciftci, N. S.; Padinger, F.; Fromherz, T.; Hummelen, J. C. 2.5% Efficient Organic Plastic Solar Cells. *Appl. Phys. Lett.* **2001**, *78*, 841–843.
- (177) Barkhouse, D. A. R.; Debnath, R.; Kramer, I. J.; Zhitomirsky, D.; Pattantyus-Abraham, A. G.; Levina, L.; Etgar, L.; Grätzel, M.; Sargent, E. H. Depleted Bulk Heterojunction Colloidal Quantum Dot Photovoltaics. *Adv. Mater.* **2011**, *23*, 3134–3138.
- (178) Kramer, I. J.; Zhitomirsky, D.; Bass, J. D.; Rice, P. M.; Topuria, T.; Krupp, L.; Thon, S. M.; Ip, A. H.; Debnath, R.; Kim, H.-C.; et al. Ordered Nanopillar Structured Electrodes for Depleted Bulk Heterojunction Colloidal Quantum Dot Solar Cells. *Adv. Mater.* **2012**, *24*, 2315–2319.
- (179) Lan, X.; Bai, J.; Masala, S.; Thon, S. M.; Ren, Y.; Kramer, I. J.; Hoogland, S.; Simchi, A.; Koleilat, G. I.; Paz-Soldan, D.; et al. Self-Assembled Nanowire Network Electrodes for Depleted Bulk Heterojunction Solar Cells. *Adv. Mater.* **2013**, *25*, 1769–1773.
- (180) Cheng, C.; Lee, M. M.; Noel, N. K.; Hughes, G. M.; Ball, J. M.; Assender, H. E.; Snaith, H. J.; Watt, A. A. R. Polystyrene Tempered Porous Titania Wells for Quantum Dot Heterojunction Solar Cells. *ACS Appl. Mater. Interfaces* **2014**, *6*, 14247–14252.
- (181) Jean, J.; Chang, S.; Brown, P. R.; Cheng, J. J.; Rekemeyer, P. H.; Bawendi, M. G.; Gradečák, S.; Bulović, V. ZnO Nanowire Arrays for Enhanced Photocurrent in PbS Quantum Dot Solar Cells. *Adv. Mater.* **2013**, *25*, 2790–2796.
- (182) Rath, A. K.; Bernechea, M.; Martinez, L.; de Arquer, F. P. G.; Osmond, J.; Konstantatos, G. Solution-Processed Inorganic Bulk Nano-Heterojunctions and Their Application to Solar Cells. *Nat. Photonics* **2012**, *6*, 529–534.
- (183) Rath, A. K.; Pelayo Garcia de Arquer, F.; Stavrinidis, A.; Lasanta, T.; Bernechea, M.; Diedenhofen, S. L.; Konstantatos, G. Remote Trap Passivation in Colloidal Quantum Dot Bulk Nano-Heterojunctions and Its Effect in Solution-Processed Solar Cells. *Adv. Mater.* **2014**, *26*, 4741–4747.
- (184) Tikhomirov, G.; Hoogland, S.; Lee, P. E.; Fischer, A.; Sargent, E. H.; Kelley, S. O. DNA-Based Programming of Quantum Dot Valency, Self-Assembly and Luminescence. *Nat. Nanotechnol.* **2011**, *6*, 485–490.
- (185) Kramer, I. J.; Levina, L.; Debnath, R.; Zhitomirsky, D.; Sargent, E. H. Solar Cells Using Quantum Funnels. *Nano Lett.* **2011**, *11*, 3701–3706.
- (186) Adinolfi, V.; Ning, Z.; Xu, J.; Masala, S.; Zhitomirsky, D.; Thon, S. M.; Sargent, E. H. Electric Field Engineering Using Quantum-Size-Effect-Tuned Heterojunctions. *Appl. Phys. Lett.* **2013**, *103*, 011106.
- (187) Ning, Z.; Zhitomirsky, D.; Adinolfi, V.; Sutherland, B.; Xu, J.; Voznyy, O.; Maraghechi, P.; Lan, X.; Hoogland, S.; Ren, Y.; et al. Graded Doping for Enhanced Colloidal Quantum Dot Photovoltaics. *Adv. Mater.* **2013**, *25*, 1719–1723.
- (188) Yuan, M.; Zhitomirsky, D.; Adinolfi, V.; Voznyy, O.; Kemp, K. W.; Ning, Z.; Lan, X.; Xu, J.; Kim, J. Y.; Dong, H.; et al. Doping Control via Molecularly Engineered Surface Ligand Coordination. *Adv. Mater.* **2013**, *25*, 5586–5592.
- (189) Ko, D.-K.; Brown, P. R.; Bawendi, M. G.; Bulović, V. p-i-n Heterojunction Solar Cells with a Colloidal Quantum-Dot Absorber Layer. *Adv. Mater.* **2014**, *26*, 4845–4850.
- (190) Debnath, R.; Greiner, M. T.; Kramer, I. J.; Fischer, A.; Tang, J.; Barkhouse, D. A. R.; Wang, X.; Levina, L.; Lu, Z.-H.; Sargent, E. H. Depleted-Heterojunction Colloidal Quantum Dot Photovoltaics Employing Low-Cost Electrical Contacts. *Appl. Phys. Lett.* **2010**, *97*, 023109.
- (191) Gao, J.; Perkins, C. L.; Luther, J. M.; Hanna, M. C.; Chen, H.-Y.; Semonin, O. E.; Nozik, A. J.; Ellingson, R. J.; Beard, M. C. n-Type Transition Metal Oxide as a Hole Extraction Layer in PbS Quantum Dot Solar Cells. *Nano Lett.* **2011**, *11*, 3263–3266.
- (192) Brown, P. R.; Lunt, R. R.; Zhao, N.; Osedach, T. P.; Wanger, D. D.; Chang, L.-Y.; Bawendi, M. G.; Bulović, V. Improved Current Extraction from ZnO/PbS Quantum Dot Heterojunction Photovoltaics Using a MoO<sub>3</sub> Interfacial Layer. *Nano Lett.* **2011**, *11*, 2955–2961.
- (193) Hyun, B.-R.; Choi, J. J.; Seyler, K. L.; Hanrath, T.; Wise, F. W. Heterojunction PbS Nanocrystal Solar Cells with Oxide Charge-Transport Layers. *ACS Nano* **2013**, *7*, 10938–10947.
- (194) Liu, H.; Tang, J.; Kramer, I. J.; Debnath, R.; Koleilat, G. I.; Wang, X.; Fisher, A.; Li, R.; Brzozowski, L.; Levina, L.; et al. Electron Acceptor Materials Engineering in Colloidal Quantum Dot Solar Cells. *Adv. Mater.* **2011**, *23*, 3832–3837.
- (195) Hoye, R. L. Z.; Ehrler, B.; Böhm, M. L.; Muñoz-Rojas, D.; Altamimi, R. M.; Alyamani, A. Y.; Vaynzof, Y.; Sadhanala, A.; Ercolano, G.; Greenham, N. C.; Improved Open-Circuit Voltage in ZnO–PbSe Quantum Dot Solar Cells by Understanding and Reducing Losses Arising from the ZnO Conduction Band Tail. *Adv. Energy Mater.* **2014**, *4*, DOI: 10.1002/aenm.201301544.
- (196) Kemp, K. W.; Labelle, A. J.; Thon, S. M.; Ip, A. H.; Kramer, I. J.; Hoogland, S.; Sargent, E. H. Interface Recombination in Depleted Heterojunction Photovoltaics Based on Colloidal Quantum Dots. *Adv. Energy Mater.* **2013**, *3*, 917–922.
- (197) Yuan, M.; Voznyy, O.; Zhitomirsky, D.; Kanjanaboos, P.; Sargent, E. H. Synergistic Doping of Fullerene Electron Transport Layer and Colloidal Quantum Dot Solids Enhances Solar Cell Performance. *Adv. Mater.* **2015**, *27*, 917–921.
- (198) Ehrler, B.; Musselman, K. P.; Böhm, M. L.; Morgenstern, F. S. F.; Vaynzof, Y.; Walker, B. J.; MacManus-Driscoll, J. L.; Greenham, N. C. Preventing Interfacial Recombination in Colloidal Quantum Dot Solar Cells by Doping the Metal Oxide. *ACS Nano* **2013**, *7*, 4210–4220.
- (199) Koleilat, G. I.; Wang, X.; Labelle, A. J.; Ip, A. H.; Carey, G. H.; Fischer, A.; Levina, L.; Brzozowski, L.; Sargent, E. H. A Donor-Supply Electrode (DSE) for Colloidal Quantum Dot Photovoltaics. *Nano Lett.* **2011**, *11*, 5173–5178.
- (200) Maraghechi, P.; Labelle, A. J.; Kirmani, A. R.; Lan, X.; Adachi, M. M.; Thon, S. M.; Hoogland, S.; Lee, A.; Ning, Z.; Fischer, A.; et al.

- The Donor–Supply Electrode Enhances Performance in Colloidal Quantum Dot Solar Cells. *ACS Nano* **2013**, *7*, 6111–6116.
- (201) Kim, G.-H.; Walker, B.; Kim, H.-B.; Kim, J. Y.; Sargent, E. H.; Park, J.; Kim, J. Y. Inverted Colloidal Quantum Dot Solar Cells. *Adv. Mater.* **2014**, *26*, 3321–3327.
- (202) Park, H.; Chang, S.; Jean, J.; Cheng, J. J.; Araujo, P. T.; Wang, M.; Bawendi, M. G.; Dresselhaus, M. S.; Bulović, V.; Kong, J.; et al. Graphene Cathode-Based ZnO Nanowire Hybrid Solar Cells. *Nano Lett.* **2013**, *13*, 233–239.
- (203) Koleilat, G. I.; Kramer, I. J.; Wong, C. T. O.; Thon, S. M.; Labelle, A. J.; Hoogland, S.; Sargent, E. H. Folded-Light-Path Colloidal Quantum Dot Solar Cells. *Sci. Rep.* **2013**, *3*, No. 2166.
- (204) Labelle, A. J.; Thon, S. M.; Masala, S.; Adachi, M. M.; Dong, H.; Farahani, M.; Ip, A. H.; Fratalocchi, A.; Sargent, E. H. Colloidal Quantum Dot Solar Cells Exploiting Hierarchical Structuring. *Nano Lett.* **2015**, *15*, 1101–1108.
- (205) Mahpeykar, S. M.; Xiong, Q.; Wang, X. Resonance-Induced Absorption Enhancement in Colloidal Quantum Dot Solar Cells Using Nanostructured Electrodes. *Opt. Express* **2014**, *22*, A1576–A1588.
- (206) Kim, S.; Kim, J. K.; Gao, J.; Song, J. H.; An, H. J.; You, T.-S.; Lee, T.-S.; Jeong, J.-R.; Lee, E.-S.; Jeong, J.-H.; et al. Lead Sulfide Nanocrystal Quantum Dot Solar Cells with Trenched ZnO Fabricated via Nanoimprinting. *ACS Appl. Mater. Interfaces* **2013**, *5*, 3803–3808.
- (207) Adachi, M. M.; Labelle, A. J.; Thon, S. M.; Lan, X.; Hoogland, S.; Sargent, E. H. Broadband Solar Absorption Enhancement via Periodic Nanostructuring of Electrodes. *Sci. Rep.* **2013**, *3*, No. 2928.
- (208) Paz-Soldan, D.; Lee, A.; Thon, S. M.; Adachi, M. M.; Dong, H.; Maraghechi, P.; Yuan, M.; Labelle, A. J.; Hoogland, S.; Liu, K.; et al. Jointly Tuned Plasmonic–Excitonic Photovoltaics Using Nanoshells. *Nano Lett.* **2013**, *13*, 1502–1508.
- (209) Kholmicheva, N.; Moroz, P.; Rijal, U.; Bastola, E.; Upadhyay, P.; Liyanage, G.; Razgoniaev, A.; Ostrowski, A. D.; Zamkov, M. Plasmonic Nanocrystal Solar Cells Utilizing Strongly Confined Radiation. *ACS Nano* **2014**, *8*, 12549–12559.
- (210) Beck, F. J.; Lasanta, T.; Konstantatos, G. Plasmonic Schottky Nanojunctions for Tailoring the Photogeneration Profile in Thin Film Solar Cells. *Adv. Opt. Mater.* **2014**, *2*, 493–500.
- (211) Kirkeminde, A.; Scott, R.; Ren, S. All Inorganic Iron Pyrite Nano-Heterojunction Solar Cells. *Nanoscale* **2012**, *4*, 7649–7654.
- (212) Beck, F. J.; Stavrinidis, A.; Diedenhofen, S. L.; Lasanta, T.; Konstantatos, G. Surface Plasmon Polariton Couplers for Light Trapping in Thin-Film Absorbers and Their Application to Colloidal Quantum Dot Optoelectronics. *ACS Photonics* **2014**, *1*, 1197–1205.
- (213) Wu, Y.; Ren, S.; Xu, X.; Liu, L.; Wang, H.; Yu, J. Engineered Fluorescence of Quantum Dots via Plasmonic Nanostructures. *Sol. Energy Mater. Sol. Cells* **2014**, *126*, 113–119.
- (214) Shockley, W.; Queisser, H. J. Detailed Balance Limit of Efficiency of *p-n* Junction Solar Cells. *J. Appl. Phys.* **2004**, *32*, 510–519.
- (215) King, R. R.; Law, D. C.; Edmondson, K. M.; Fetzer, C. M.; Kinsey, G. S.; Yoon, H.; Sherif, R. A.; Karam, N. H. 40% Efficient Metamorphic GaInP/GaInAs/Ge Multijunction Solar Cells. *Appl. Phys. Lett.* **2007**, *90*, 183516.
- (216) Wang, X.; Koleilat, G. I.; Tang, J.; Liu, H.; Kramer, I. J.; Debnath, R.; Brzozowski, L.; Barkhouse, D. A. R.; Levina, L.; Hoogland, S.; et al. Tandem Colloidal Quantum Dot Solar Cells Employing a Graded Recombination Layer. *Nat. Photonics* **2011**, *5*, 480–484.
- (217) Choi, J. J.; Wenger, W. N.; Hoffman, R. S.; Lim, Y.-F.; Luria, J.; Jasieniak, J.; Marohn, J. A.; Hanrath, T. Solution-Processed Nanocrystal Quantum Dot Tandem Solar Cells. *Adv. Mater.* **2011**, *23*, 3144–3148.
- (218) Nozik, A. J.; Beard, M. C.; Luther, J. M.; Law, M.; Ellingson, R. J.; Johnson, J. C. Semiconductor Quantum Dots and Quantum Dot Arrays and Applications of Multiple Exciton Generation to Third-Generation Photovoltaic Solar Cells. *Chem. Rev.* **2010**, *110*, 6873–6890.
- (219) Ross, R. T.; Nozik, A. J. Efficiency of Hot-Carrier Solar Energy Converters. *J. Appl. Phys.* **1982**, *53*, 3813–3818.
- (220) Pandey, A.; Guyot-Sionnest, P. Slow Electron Cooling in Colloidal Quantum Dots. *Science* **2008**, *322*, 929–932.
- (221) Tisdale, W. A.; Williams, K. J.; Timp, B. A.; Norris, D. J.; Aydil, E. S.; Zhu, X.-Y. Hot-Electron Transfer from Semiconductor Nanocrystals. *Science* **2010**, *328*, 1543–1547.
- (222) Beard, M. C.; Luther, J. M.; Semonin, O. E.; Nozik, A. J. Third Generation Photovoltaics Based on Multiple Exciton Generation in Quantum Confined Semiconductors. *Acc. Chem. Res.* **2012**, *46*, 1252–1260.
- (223) Schaller, R. D.; Klimov, V. I. High Efficiency Carrier Multiplication in PbSe Nanocrystals: Implications for Solar Energy Conversion. *Phys. Rev. Lett.* **2004**, *92*, 186601.
- (224) Nair, G.; Chang, L.-Y.; Geyer, S. M.; Bawendi, M. G. Perspective on the Prospects of a Carrier Multiplication Nanocrystal Solar Cell. *Nano Lett.* **2011**, *11*, 2145–2151.
- (225) McGuire, J. A.; Sykora, M.; Joo, J.; Pietryga, J. M.; Klimov, V. I. Apparent versus True Carrier Multiplication Yields in Semiconductor Nanocrystals. *Nano Lett.* **2010**, *10*, 2049–2057.
- (226) Delerue, C.; Allan, G.; Pijpers, J. J. H.; Bonn, M. Carrier Multiplication in Bulk and Nanocrystalline Semiconductors: Mechanism, Efficiency, and Interest for Solar Cells. *Phys. Rev. B* **2010**, *81*, 125306.
- (227) Beard, M. C.; Midgett, A. G.; Hanna, M. C.; Luther, J. M.; Hughes, B. K.; Nozik, A. J. Comparing Multiple Exciton Generation in Quantum Dots To Impact Ionization in Bulk Semiconductors: Implications for Enhancement of Solar Energy Conversion. *Nano Lett.* **2010**, *10*, 3019–3027.
- (228) Semonin, O. E.; Luther, J. M.; Choi, S.; Chen, H.-Y.; Gao, J.; Nozik, A. J.; Beard, M. C. Peak External Photocurrent Quantum Efficiency Exceeding 100% via MEG in a Quantum Dot Solar Cell. *Science* **2011**, *334*, 1530–1533.
- (229) Smith, M. B.; Michl, J. Singlet Fission. *Chem. Rev.* **2010**, *110*, 6891–6936.
- (230) Tabachnyk, M.; Ehrler, B.; Gélinas, S.; Böhm, M. L.; Walker, B. J.; Musselman, K. P.; Greenham, N. C.; Friend, R. H.; Rao, A. Resonant Energy Transfer of Triplet Excitons from Pentacene to PbSe Nanocrystals. *Nat. Mater.* **2014**, *13*, 1033–1038.
- (231) Thompson, N. J.; Wilson, M. W. B.; Congreve, D. N.; Brown, P. R.; Scherer, J. M.; Bischof, T. S.; Wu, M.; Geva, N.; Welborn, M.; Voorhis, T. V.; et al. Energy Harvesting of Non-Emissive Triplet Excitons in Tetracene by Emissive PbS Nanocrystals. *Nat. Mater.* **2014**, *13*, 1039–1043.